CARBON NANOTUBE GROWTH RATE REGRESSION USING SUPPORT VECTOR MACHINES AND ARTIFICIAL NEURAL NETWORKS

THESIS

Nicholas M. Westing, First Lieutenant, USAF

AFIT-ENG-14-M-83

DEPARTMENT OF THE AIR FORCE
AIR UNIVERSITY

AIR FORCE INSTITUTE OF TECHNOLOGY

Wright-Patterson Air Force Base, Ohio

AFIT-ENG-14-M-83

CARBON NANOTUBE GROWTH RATE REGRESSION USING SUPPORT VECTOR MACHINES AND ARTIFICIAL NEURAL NETWORKS

THESIS

Presented to the Faculty

Department of Electrical and Computer Engineering

Graduate School of Engineering and Management

Air Force Institute of Technology

Air University

Air Education and Training Command

in Partial Fulfillment of the Requirements for the

Degree of Master of Science in Electrical Engineering

Nicholas M. Westing, B.S.E.E.

First Lieutenant, USAF

March 2014

AFIT-ENG-14-M-83

CARBON NANOTUBE GROWTH RATE REGRESSION USING SUPPORT VECTOR MACHINES AND ARTIFICIAL NEURAL NETWORKS

Nicholas M. Westing, B.S.E.E.
First Lieutenant, USAF

Approved:

//signed//	13 Feb 2014
Lt Col Jeffrey D. Clark, PhD (Chairman)	Date
//signed//	13 Feb 2014
Maj Michael C. Pochet, PhD (Member)	Date
//signed//	13 Feb 2014
Dr. Benji Maruyama, PhD (Member)	Date

AFIT-ENG-14-M-83

Abstract

Control of carbon nanotube growth rates is a challenging problem, thus limiting their use in a wide variety of applications. Carbon nanotubes demonstrating metallic or semiconducting properties allow for high strength materials and high current densities in smaller wires. Due to their simplicity and desirable properties, Single Walled Carbon Nanotubes (SWNTs) are considered for chiral-selective growth experiments. A machine learning based approach for chiral selective growth of SWNTs using a laser-induced chemical vapor deposition growth system is introduced. Determination of SWNT growth rates is performed through in-situ Raman spectroscopy using a 532 nm excitation laser.

A total of 450 experiments are performed and a subset of 121 experiments are used to train a SWNT vs. Multi Walled Carbon Nanotube (MWNT) Support Vector Machine (SVM) classifier. The SVM classifier determines parameter values for 99% probability or greater of SWNT growth with an accuracy of 95.04%. This subset of synthesis parameters are evaluated using an Artificial Neural Network (ANN) to predict SWNT growth rates and growth lengths.

Analysis of the ANN growth rate model showed a peak in growth rate as a function of water concentration and growth temperature. The growth length model was trained using the same growth experiments as the growth rate model and showed a 80% reduction in validation errors. The growth length model also identified an optimal water/ethylene ratio for maximizing SWNT length.

Table of Contents

Page

Page

List of Figures

Figure Page

Figure Page

List of Tables

List of Acronyms

Acronym	Definition
ANN	Artificial Neural Network
CNT	Carbon Nanotube
SOM	Self-Organizing Map
SWNT	Single Walled Carbon Nanotube
MWNT	Multi Walled Carbon Nanotube
CVD	Chemical Vapor Deposition
SVM	Support Vector Machine
RBF	Radial Basis Function
SVR	Support Vector Machine Regression
MOSFET	Metal-Oxide Semiconductor Field Effect Transistor
RBM	Radial Breathing Mode
AFRL	Air Force Research Laboratory
SCCM	Standard Cubic Centimeter per Minute
SMO	Sequential Minimal Optimization
WEKA	Waikato Environment for Knowledge Analysis
ARFF	Attribute Relationship File Format
GPU	Graphics Processing Unit
MSE	Mean Squared Error
AUC	Area Under Receiver Operating Characteristic Curve
ARES	Adaptive Rapid Experimentation and in-situ Spectroscopy

CARBON NANOTUBE GROWTH RATE REGRESSION USING SUPPORT VECTOR MACHINES AND ARTIFICIAL NEURAL NETWORKS

I. Introduction

Since their relatively recent discovery, Carbon Nanotubes (CNTs) have been researched for a wide variety of applications across science and technology [12, 23]. CNTs are the only nanostructured carbon material to reach large scale production to include fullerenes, graphene and carbon black [52]. The electrical, mechanical, thermal and chemical properties of CNTs are determined during the growth process due to the organization of the carbon atoms [5]. Determining the CNT structure allows many applications to take advantage of their unique properties. For example, using CNTs in transistors allows for faster and smaller computers without increased heat because of their conductivity properties. This also allows computer engineers to continue doubling the number of transistors every two years, known as Moore's Law. [50]

Recent research has discovered a relationship between Single Walled Carbon Nanotube (SWNT) structure and growth rate [45]. Rao et al. did not control the growth rate in their experiments, but rather the growth rate was determined posterior. The goal of this thesis is to to predict the CNT structure based on input parameters before growth begins. A growth chamber model is constructed using a Support Vector Machine (SVM) classifier to predict when SWNTs would grow and an Artificial Neural Network (ANN) is used to predict input parameters for a specific growth rate. Once an accurate growth chamber model is constructed and accurate prediction is validated, further understanding of the nucleation, growth, and termination of CNTs will be possible.

1.1 Problem Statement

Traditional Chemical Vapor Deposition (CVD) growth of CNTs takes hours per growth, however a novel growth system under development at Air Force Research Laboratory (AFRL) shortens this growth time to several minutes and can execute over 100 experiments per day [45, 52]. The automated growth system has the capability to run a set of experiments without any user intervention allowing exploration of the entire parameter space whereby background pressure, temperature, feedstock gas type and flow rates are varied. Unfortunately, varying catalyst types, sizes, shapes, carbon gases, pressures, water concentration and growth temperature creates a large input space preventing an exhaustive search through experimentation even at this faster rate.

Understanding the effects of these parameters on CNT growth is accomplished by adjusting one or two parameters per experiment and analyzing the differences in tube quality, length and orientation. This technique provides a better understanding of how the adjusted parameters affect CNT growth, but doesn't necessarily lead to an optimized set of parameters to grow CNTs with a desired structure.

Optimized growth parameters for a desired CNT structure are required and depend on the exploration of the multi-dimensional parameter space. Performing an exhaustive search across this space is intractable. The goal of this thesis is to constrain synthesis results to only SWNT growth and then use the constrained input parameters to control the growth rate using an ANN.

1.2 Justification

Using a machine learning approach to determine optimal growth parameters offers several advantages over traditional materials science techniques. This type of data analysis creates decision boundaries within the input space, highlights areas of missing data and predicts the CNT structure.

Generating decision boundaries between SWNT and Multi Walled Carbon Nanotube (MWNT) growth parameters is crucial for predicting SWNT growth rates. The differences in SWNT and MWNT growth parameters provides insight in the underlying growth properties and emphasizes growth parameters with strong affects on growth.

Investigating the effects of one growth parameter at a time on the CNT growth rate is a slow process requiring time and materials. A machine learning approach is able to highlight areas of missing data by incorporating confidence bounds in experiment prediction. Theoretical experimental parameters similar to the training experiment parameters will have a higher prediction confidence than experiments outside the training experimental parameter ranges.

The machine learning model determines growth chamber inputs that produce a desired growth rate, which is validated through experimentation. Each new catalyst will require a new model, however, the determination of the new model is achieved at a lower cost. The result of this lower cost is a quicker search across more catalyst materials. More catalyst compositions can be explored and optimized growth rates are realized by this faster search.

1.3 Assumptions

The machine learning approach used for extracting optimal growth parameters assumes the catalyst material and architecture are held constant. The model does not include differences in surface chemistry and growth reactions across all catalyst materials.

The given sputtered catalyst thickness is assumed uniform across all growth samples in the system. This assumption is necessary since the thickness of the catalyst cannot be measured in the current growth system without removing the sample from the growth chamber. Measuring the catalyst thickness of each growth sample would reduce experimentation speed and data collection.

The catalyst size distribution across each pillar is assumed a direct result of the growth parameters used. The sputtered catalyst film will break up into catalyst particles as a result of laser heating. The laser power, chamber pressure and partial pressures of each gas will have an effect on how the catalyst film distributes into particles.

The measured growth temperature is assumed uniform across the surface of the silicon pillar. Previous work has shown a small temperature gradient within the silicon pillar and across the surface [45]. However, proper laser alignment on the center of the pillar reduces the temperature gradients at the point of growth to be negligible for this thesis.

1.4 Approach

Each growth experiment results in either SWNT growth, MWNT growth, both SWNT and MWNT growth or no growth. This thesis focuses on predicting SWNT growth rates, therefore, a classifier is required to determine the growth experiments that produce SWNTs. The SWNT classifier will implement the SVM algorithm using a Radial Basis Function (RBF) kernel.

The SVM model will provide a probability of obtaining SWNT growth for a given set of experimental parameters. This model is validated through experimentation on sets of parameters satisfying a specified confidence bound.

The subset of experimental parameters, predicted to grow only SWNTs, are used to determine the growth rate of SWNTs. The prediction model incorporates an ANN to determine experimental parameters necessary for a specified growth rate. The ANN model will be validated through experimentation on parameters predicted to produce SWNT growth.

The SVM model and ANN prediction model will be used together to extrapolate the collected experimental data into areas with little knowledge of growth. This technique

determines new experiment parameters resulting in SWNT growth and explores these areas for growth rate prediction.

1.5 Materials and Equipment

A laser-induced CVD growth system located at AFRL is required for collecting CNT growth data. The growth system, Adaptive Rapid Experimentation and in-situ Spectroscopy (ARES), is an automated system capable of running sequences of experiments without user input. Samples consist of 10 μm diameter pillars of silicon placed 40 μm apart. Sputtered films of alumina are first placed on the pillars, followed by nickel which is sputtered on top of the alumina to create the catalyst used in all growth experiments. The system utilizes a 532nm excitation laser for both silicon pillar heating and in-situ Raman spectroscopy. The laser is focused on each pillar using a 50× objective lens resulting in a laser spot size diameter of 7 μm. Research grade hydrogen, ethylene and a mix of 99:1 argon to carbon dioxide are pumped into the growth chamber at varying flow rates generating different chamber growth pressures. [45]

II. Background

This chapter outlines previous work in controlling Carbon Nanotube (CNT) growth with an emphasis on nanotechnology advances utilizing machine learning techniques to control experiment parameters. Section 2.1 is a summary of different growth methods with a focus on how each growth variable affects the overall structure of the nanotube. Structures and properties of CNTs are discussed in Section 2.2 and research accomplished that optimizes the growth parameters for specific structures is discussed in Section 2.3.

Support Vector Machine (SVM) classification and Artificial Neural Network (ANN) regression techniques are introduced in Section 2.4. Kernel functions for SVM classification, and activation functions for ANN are discussed. This chapter concludes with a discussion on machine learning approaches applied to similar nanotechnology fields.

2.1 Summary of Growth Methods

CNT growth requires a metallic catalyst, carbon gas, and high temperatures to begin the growth process [23]. The three main techniques used to grow CNTs are arc discharge, chemical vapor depostion (CVD), and laser ablation [39]. Each method is a variation on the heating of a metal catalyst combined with a carbon source to nucleate growth [10]. The purity, length, alignment and diameter of Single Walled Carbon Nanotube (SWNT)s varies depending on the growth method and growth conditions [39].

2.1.1 Arc Discharge.

The arc discharge growth method uses two graphite electrodes to create an electric arc in a chamber filled with inert gas at low pressures creating carbon deposits. The electrodes are spaced 1 mm apart where 20 volts, (50-100 amps), create the high

temperature discharge. This discharge creates a small rod-shaped deposit on one of the electrodes. [10]

More recent developments in arc discharge growth use several gases and metal catalysts on the tips of the electrodes [52]. This produces very high yields of CNTs as was shown using catalyst particles and graphite powder only placed on the anode to produce bundles of SWNTs [10].

2.1.2 Laser Ablation.

Synthesizing SWNTs using the arc discharge method offers limited control over growth temperature with moderate yields of nanotubes and quality [10]. However, laser ablation utilizes a scanning laser beam that focuses on a metal-graphite composite target. The laser and the target are mounted in a quartz tube with an inert gas flowing across the target. The quartz tube containing the target is mounted inside a $1200°C$ furnace. A water cooled collector is mounted outside the furnace for collecting the nanotubes and the by-products produced by this process. [10] This method allows for high yields of SWNTs, which is proportional to the temperature of the furnace [17].

2.1.3 Chemical Vapor Deposition.

Chemical Vapor Deposition (CVD) synthesis requires an oven, tubular reactor, and mass flow controllers for the mixture of gases in the chamber. This method allows many variations in growth parameters providing a detailed understanding of the affects they have on CNT production and quality. CVD growth occurs at relatively low temperatures, allowing silicon to be used as a substrate which increases the possibilities for CNT integration with electronic applications. [52] The scale-up possibilities for bulk growth and the ability to grow on a specific surface at predetermined locations, make this growth technique useful for a wide range of applications [55].

2.2 Carbon Nanotube Structures and Properties

SWNTs are depicted as long wrapped sheets of graphene as shown in Fig. 2.1 while Multi Walled Carbon Nanotube (MWNT)s are concentric SWNTs with varying diameters. SWNTs have been studied in greater detail because modeling MWNTs is more complex with many unknown relationships existing between the concentric SWNTs. [40]

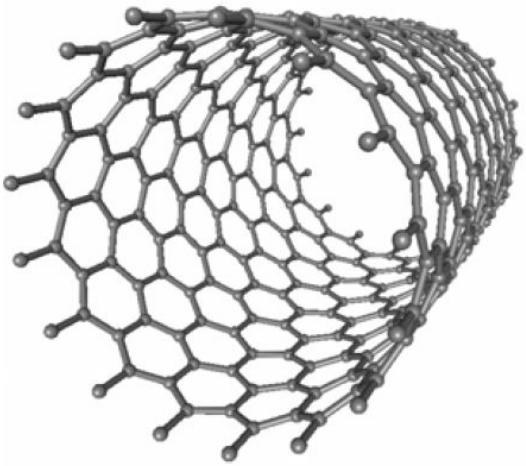

Figure 2.1: Depiction of a Single Wall Carbon Nanotube [24] ©1998 IEEE.

The chiral angle determines the conducting properties of CNTs and is determined using using two vectors, $\mathbf{C}_h$ and $\mathbf{T}$, to describe a rectangle in the lattice. The lattice shown in Fig. 2.2 is a CNT unrolled. The vector $\mathbf{T}$ is perpendicular to the chiral vector $\mathbf{C}_h$ as shown in Fig. 2.2. [40] The chiral vector is defined as:

$$\mathbf{C}_h = n\mathbf{a}_1 + m\mathbf{a}_2, \tag{2.1}$$

where n and m are integers and $\mathbf{a}_1$ and $\mathbf{a}_2$ are unit vectors of the hexagonal lattice described by: [40]:

$$\mathbf{a}_1 = (\tfrac{\sqrt{3}}{2}, \tfrac{1}{2}) \quad \mathbf{a}_2 = (\tfrac{\sqrt{3}}{2}, \tfrac{-1}{2}). \tag{2.2}$$

The unit vectors $\mathbf{a}_1$ and $\mathbf{a}_2$ are shown in Fig. 2.2. The end points of the chiral vector meet when the flattened lattice shown in Fig. 2.2 is rolled into a CNT [39]. The chiral angle is

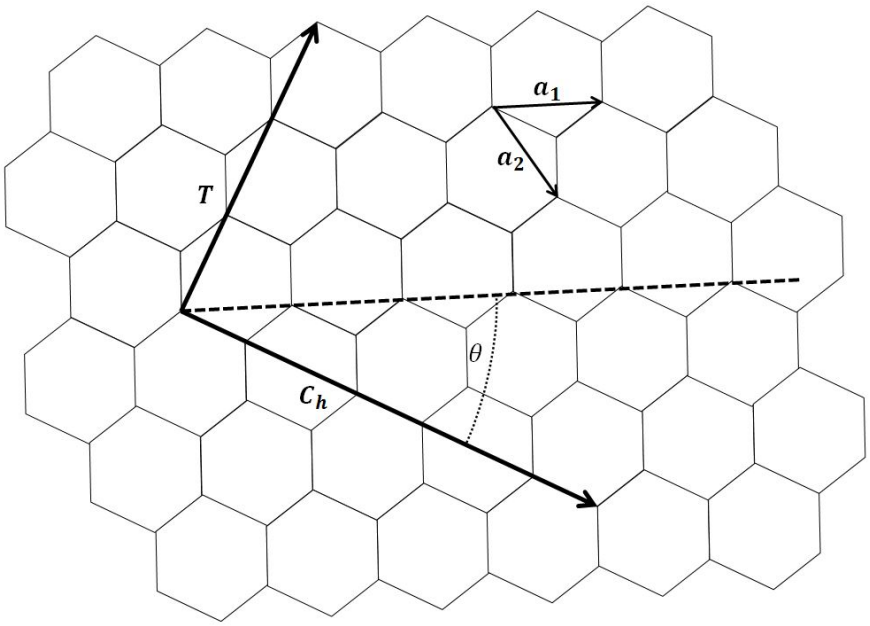

Figure 2.2: $\mathbf{C}_h$ and $\mathbf{T}$ describe a rectangle in the SWNT lattice where $\mathbf{C}_h$ is the chiral vector and $\mathbf{T}$ is a vector perpendicular to $\mathbf{C}_h$. The chiral vector is made up of the unit vectors $\mathbf{a}_1$ $\mathbf{a}_2$ and the angle θ determines the tube type of either zig zag, chiral or armchair. Recreated from [4, 39].

the angle between the chiral vector and the unit vector $\mathbf{a}_1$ expressed as:

$$\theta = \tan^{-1}\left(\sqrt{3}\left(\frac{n}{2m+n}\right)\right), \tag{2.3}$$

where m and n are integers used to describe the chiral vector [39]. Using this angle and the chiral vector, the type of CNT is determined. A chiral nanotube is defined as a nanotube of a chiral angle between 0° and 30° and a chiral vector of $\mathbf{C}_h = (n, m)$, where $m \neq n$ in Eq. (2.2). Table 2.1 explains the properties of 'zigzag' and 'armchair' CNTs. [32]

2.2.1 Electrical, Mechanical and Chemical Properties.

The electrical properties of CNTs depend on their structure. A CNT is metallic if $(2n + m)$ is a multiple of 3. If this value is not a multiple of 3 the CNT is considered a semiconductor. Theoretical predictions imply CNTs are low loss conductors of electricity because of their ballistic transport properties. This prediction is based on CNTs similarity

Table 2.1: Summary of CNT types [32]

Type	Angle	Vector
Zigzag	0°	(n,0)
Armchair	30°	(n,n)
Chiral	$0° < x < 30°$	(n,m)

to graphene. The band structure of a graphene sheet is shown in Fig. 2.3 (top) with the first Brillouin zone depicted shown in Fig. 2.3 (bottom). The valence and conduction states meet at six points at the Fermi level. This makes graphene a zero-gap semiconductor. [8]

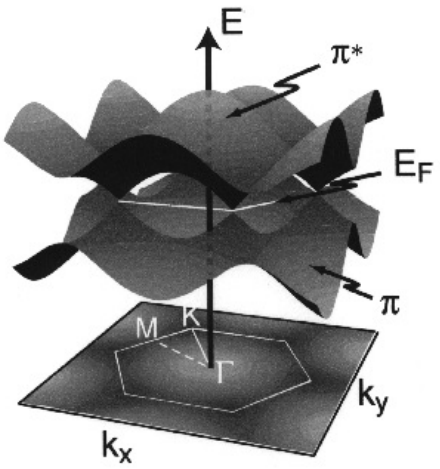

Figure 2.3: Band structure of graphene(top) overlaid on the first Brillouin zone(bottom). The conduction and valence states meet at the Fermi level at six different points making graphene a zero-gap semiconductor. [8] ©2003 IEEE

Considering CNTs as 'rolled graphene' means each band of graphene divides into a number of one dimensional subbands. The allowed energy states of the CNT are slices of the graphene band structure. If these slices only go through a Fermi point, the

tube is metallic. Figure 2.4a shows the band structure for a metallic armchair tube and Fig. 2.4b shows the band structure for a semiconducting tube. [8]

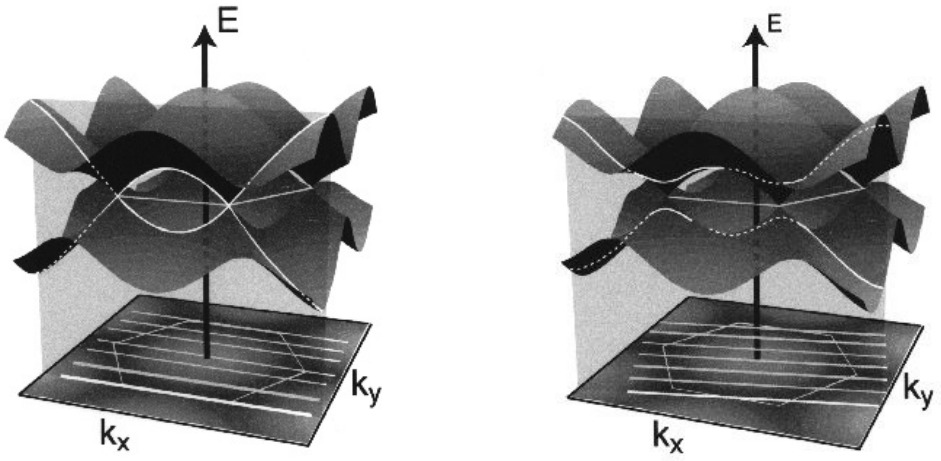

(a) (b)

Figure 2.4: (a) Band structure of an armchair CNT (top) overlaid on the first Brillouin zone (bottom). The lines crossing through the Brillouin zone only cross at Fermi points as shown by the gray plane, making the armchair CNT metallic. (b) The lines crossing the Brillouin zone do not only cross at the Fermi points, as shown by the gray plane, making the chiral CNT a semiconductor. [8] ©2003 IEEE

A single CNT has a current carrying capacity up to 25 μA that corresponds to a current density of $10^9 A/cm^2$, 1000 times greater than copper. The bandgap energy of semiconducting CNTs is related to the diameter of the tube as:

$$E_g = \frac{|t|a_{cc}}{D} = \frac{.84eV}{D}, \tag{2.4}$$

where $|t|$ is the carbon to carbon tight binding overlap energy, a_{cc} is the carbon to carbon bond length (1.42 Å), and D is the tube diameter. [39]

The tube diameter is calculated as:

$$D = \frac{a_{cc}\sqrt{3\left(n^2 + m^2 + nm\right)}}{\pi}, \tag{2.5}$$

where n and m are integers describing the chiral vector [39].

Figure 2.5 is a Kataura plot showing how gap energy relates to tube diameter for metallic and semiconducting SWNTs. The two horizontal lines in each catalyst area represent the metallic window where only metallic tubes are observed. [18] Kataura plots referenced later also include another x-axis for the Radial Breathing Mode (RBM) frequency of the tube. The RBM is inversely related to the tube diameter and analyzed using Raman spectroscopy [39].

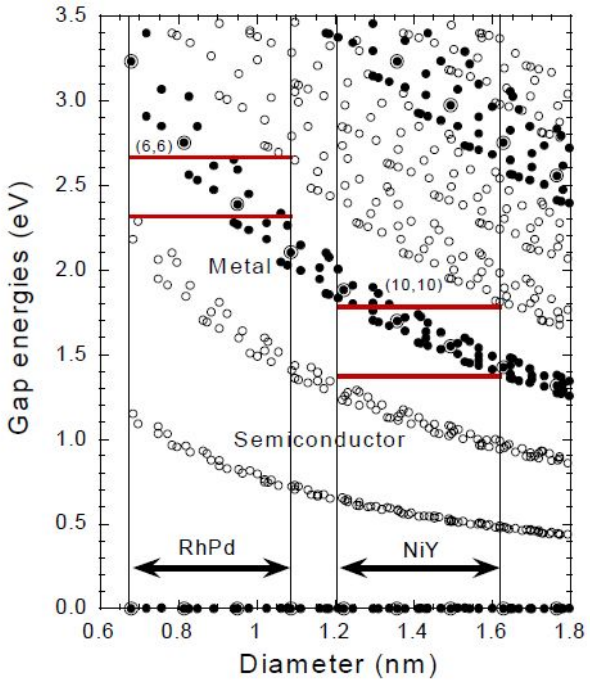

Figure 2.5: Kataura plot showing the gap energies using a laser excitation of 2.75eV. Two different catalysts, RhPd and NiY, were used for finding the metallic windows depicted by the horizontal lines. The diameter and gap energy within this horizontal lines are predicted to produce only metallic tubes. The solid circles are metallic SWNTs and open circles are semiconducting SWNTs. Double circles are armchair type. Reprinted with permission from [18]. ©1999 Elsevier

The high current density and ability to control band gap energies make CNTs useful for applications in nanoelectronics. The Metal-Oxide Semiconductor Field Effect Transistor (MOSFET) is used in almost all computer chips and CNTs are being utilized as the semiconducting channel in these devices instead of silicon. [39]

The mechanical strength of CNTs is due to the strength of the carbon to carbon bond. In 2000, stress-strain measurements were performed on individual MWNTs inside an electron microscope. The modulus values for this experiment varied between 0.27-0.95 TPa. Also shown in this experiment was a fracture strength between 11-63 GPa. The accepted values now for the Young's Modulus is 1 TPa and the tensile strength is 45 GPa. The strength/weight ratio of CNTs is 500 times greater than that of steel or aluminum making it an ideal material for applications such as protective equipment and high strength polymers. [25]

All carbon to carbon bonds are filled in a CNT so they are chemically inert and stable in acids, bases and solvents. The stability of CNTs in different types of chemicals have led to the use of CNTs in a variety of chemical sensors. Sensors made of SWNTs were able to detect certain gases, specifically cyclohexane, due to changes in electrical conductivity with gas adsorption. Different gases produce different electrical resistances across the tube, as shown in Fig. 2.6 where the parts per million (ppm) of cyclohexane is increased and the CNT resistance increases directly. [53]

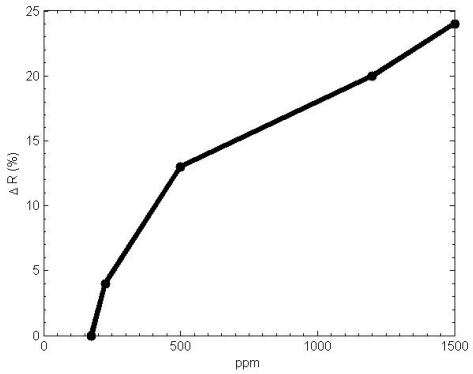

Figure 2.6: CNT resistance versus cyclohexane vapor pressure showing the ability of SWNTs to detect certain gases. Reproduced from [53].

2.2.2 Growth Mechanisms.

An active catalyst nanoparticle (Fe, Ni, Co, etc.) is required for growth to occur and the nanoparticle must have access to a carbon feedstock. It is assumed that once CNTs begin to grow, the diameter is fixed and will not change. The nanotube diameter is related to the nanoparticle size and it is also assumed only one CNT precipitates from each nanoparticle. [39]

CNT growth happens through surface carbon diffusion or bulk carbon diffusion [39]. Surface carbon diffusion is the common growth mechanism in low temperature growth and occurs when the carbon gas diffuses near the surface. The catalyst particle remains a solid in this process. The continual diffusion of the carbon gas into the solid catalyst particles on the surface causes the CNT to begin to precipitate out of the catalyst [39].

Bulk carbon diffusion uses a carbon feedstock gas similar to surface carbon diffusion. The catalyst particles dissolve the carbon gas until saturation is achieved which begins the growth of a CNT [39]. However, the metal catalyst may become a liquid nanodroplet making this process a vapor-liquid-solid transition where the feedstock gas is dissolved by the catalyst forming a metal-carbon liquid which then transitions to a solid nanotube [39]. The specific mechanism that will cause CNT growth depends on the temperature, catalyst particle and the carbon feedstock gas used in the experiment.

In both of the growth methods discussed above growth can occur at the base or tip of the CNT. Base growth generally produces SWNTs, while tip growth leads to MWNTs [39].

When the catalyst-substrate interaction is weak, hydrocarbon decomposes on the surface of the catalyst causing carbon to diffuse down into the metal. This diffusion into the metal catalyst causes the CNT to grow from the bottom of the metal catalyst pushing the whole particle off the substrate resulting in tip growth. The CNT will continue to grow

as long as the metal catalyst particle remains open to hydrocarbon decomposition. Growth stops once the metal catalyst is covered with excess carbon. [32] Figure 2.7 depicts a tip growth process.

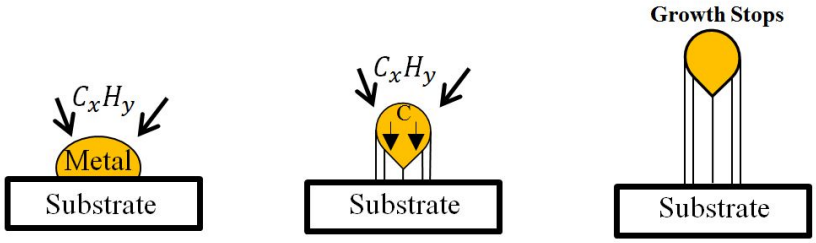

Figure 2.7: Tip Growth Model where the catalyst-substrate interaction is weak allowing the catalyst particle to lift off and precipitate a CNT from below the catalyst. Recreated from [32].

When the catalyst-substrate interaction is strong, hydrocarbon decomposition and initial CNT growth occurs similar to tip growth except the CNT is unable to pull the catalyst particle off the surface. In this situation (base growth) the CNT grows with the catalyst particle at is root and continues to grow as long as a hydrocarbon decomposition continues to occur on the catalyst as shown in Fig. 2.8. [32]

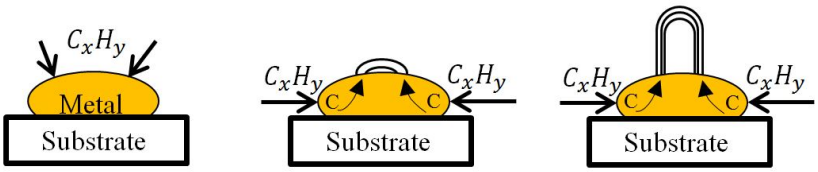

Figure 2.8: Base Growth Model depicting the strong catalyst-substrate interaction allowing a CNT to precipitate out of the top of the catalyst particle. Recreated from [32].

Another growth mechanism model used to describe the nucleation, growth and termination of CNTs is known as the Puretzky model and is shown in Fig. 2.9 [5]. In Puretzky's model, the feedstock molecules collide with the surface of the catalyst creating

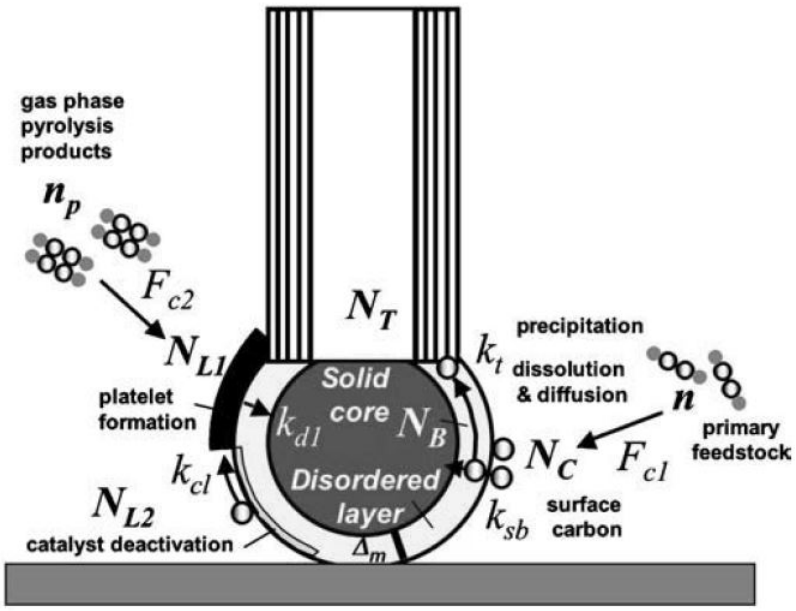

Figure 2.9: The Puretzky Growth Model depicting the arrival of carbon feedstock gas on the surface of the catalyst nanoparticle. The flux of carbon into the catalyst determines the number of walls produced and the growth rate. As the flux of carbon into the catalyst increases beyond what the catalyst can accept, a carbonaceous layer is formed reducing the ability of the catalyst to accept more carbon atoms. Growth terminates when the catalyst can no longer accept additional carbon atoms. Reprinted with permission from [5]. ©2005 American Institute of Physics.

a stable flux of carbon, F_{c1}. A small portion of these molecules bond to the nanoparticle creating the initial source of carbon atoms, N_C, for growth. A highly disordered molten layer is formed on the surface of the nanoparticle from the dissolution of carbon atoms to the nanoparticle at a rate of k_{sb}. This molten layer has a thickness, Δ_m, that depends on the growth temperature and the number of molecules, N_C, decomposing on the nanoparticle surface. [5] The molten layer focuses the diffusion of the carbon atoms, N_B, at a constant rate, k_t, into a CNT because of the higher diffusivity of the molten layer. Growth continues in this way as long as the right amount of carbon atoms are diffusing into the molten layer of the catalyst nanoparticle. Termination of growth occurs because a small amount of the incoming carbon atoms create a carbonaceous layer, N_{L1}, at a rate of k_s on the nanoparticle

surface. This layer reduces the surface area available for carbon atoms to enter the molten layer. When the entire surface of the nanoparticle is covered in a carbonaceous layer, growth terminates. [5]

For growth occurring in the temperature range of 700°C-900°C an additional growth process is required. A second carbon flux, F_{C2}, leads to the formation of the carbonaceous layer because of gas-phase pyrolosis products, n_p, of the carbon feedstock gas. An inactive catalyst layer, N_{L2}, forms, however, this layer is able to be reactivated using water or other carbon feedstock gases. [5] At higher temperatures diffusion of silicon atoms from a silicon substrate into the nanoparticle may lead to the creation of the deactivated layer. The deactivated layer and carbonaceous layer appear as islands on the catalyst nanoparticle. As these islands spread, growth terminates unless the deactivated layer is reactivated. This additional growth process explains how growth experiments are able to stop and start growth. [5]

2.3 Review of Previous Work in Optimizing Carbon Nanotube Growth Parameters

This section will outline some of the work accomplished to control CNT growth for specific applications. To fully understand the commercial applications of CNTs, it is important to be able to control each growth accurately. Optimized growth can mean precise location, orientation, chirality, length, yield or diameter [39]. The conclusion of this section will summarize the adjustable variables to optimize CNT growth.

2.3.1 Location and Orientation Control.

Controlled growth of CNTs in specific locations on a device has tremendous possibilities in fields such as nanoelectronics for use in MOSFETs and interconnects [39]. There are several methods to pattern the catalysts on the substrate for CNT growth. These include using a photoresist to only allow the catalyst on predetermined locations of the substrate, using a stamp method to remove the catalyst from all unwanted areas of the substrate, and removing CNTs from the substrate after growth [49]. Fig. 2.10(a) shows

pre-growth patterning of the substrate and Fig. 2.10(b) shows the schematic for post growth patterning.

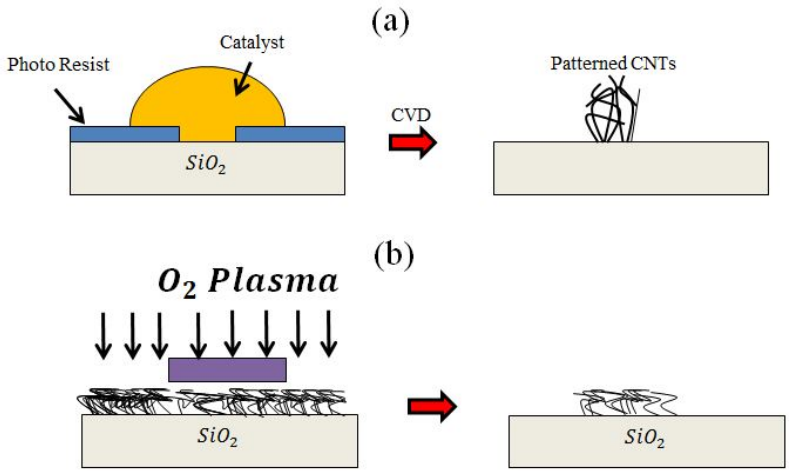

Figure 2.10: (a) Growth Patterning with a Photoresist using pre-growth patterning. (b) Post-growth patterning using a photoresist. (c) The boundary between the SiO_2 and the patterned CNTs. Recreated from [49].

Stamp methods are also used to remove the catalyst during pre-growth or to remove the CNTs post growth [49]. Using the post growth method, with gold stamps, allows the stamps to be reused providing very precise CNT patterns. Figure 2.11 shows the schematic of the gold stamp method and the resulting patterned CNTs.

In many devices it is critical to have the CNT oriented in a predetermined direction. Aligned growth is achieved using electric fields, substrate etching and fast heating methods among others [39]. The substrate is important for alignment because it determines which methods can be applied. For example electric field alignment works for many substrates, however, fast heating may cause damage to the substrate material resulting in poor yields of aligned CNTs [39]. Recent work with quartz and sapphire substrates have led to greater than 99.9% alignment and the gas flow has little affect on the growth direction in this configuration [19].

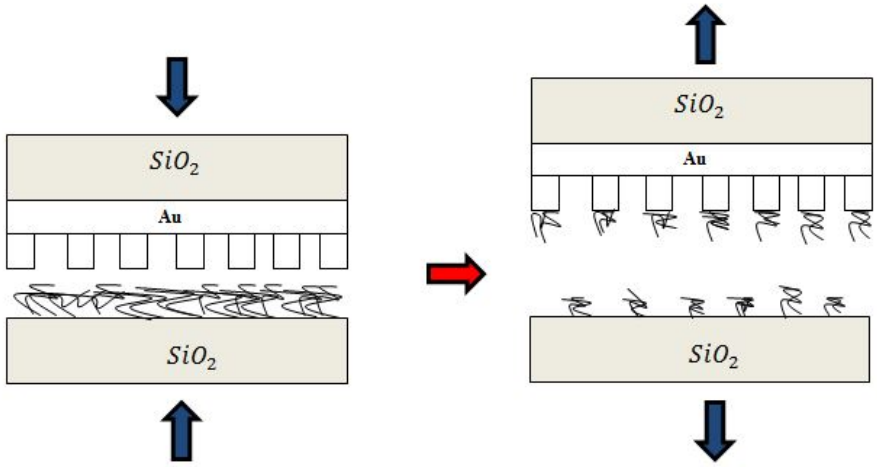

Figure 2.11: Post Growth Patterning with a gold stamp to remove rows of CNTs. Recreated from [49].

2.3.2 Chirality and Diameter Control.

The CVD growth method struggles to control the diameter distribution of tubes. Other methods are able to grow CNTs with much smaller diameter variances, however, CVD produces a higher yield and therefore is investigated more often for diameter control. [39] The diameters of SWNTs has been controlled to some degree in the CVD process by tuning the size of the catalyst nanoparticles [19].

The choice of the catalyst also influences the growth rate and tube diameter in SWNTs and MWNTs [10]. Iron group elements such as Cobalt, Nickel and Iron are preferred for SWNT growth by CVD although the size of the Iron particles directly relates to SWNT or MWNT growth [20]. Pure Nickel or Cobalt catalysts result in a much higher percentage of MWNTs than SWNTs [37]. A correlation between the size of the catalyst and the diameters of synthesized nanotubes was accomplished for SWNT growth using iron oxide particles however other research has shown this correlation does not exist [20, 34]. The catalyst particle size may change during the growth process because of the high temperatures and melting particles, known as Ostwald ripening [7, 20].

For typical diameters, there are approximately 100 different possible chiralities [47]. This amount of variety makes controlling the chirality of a nanotube challenging, specifically for controlling the growth of strictly metallic or semiconducting nanotubes.

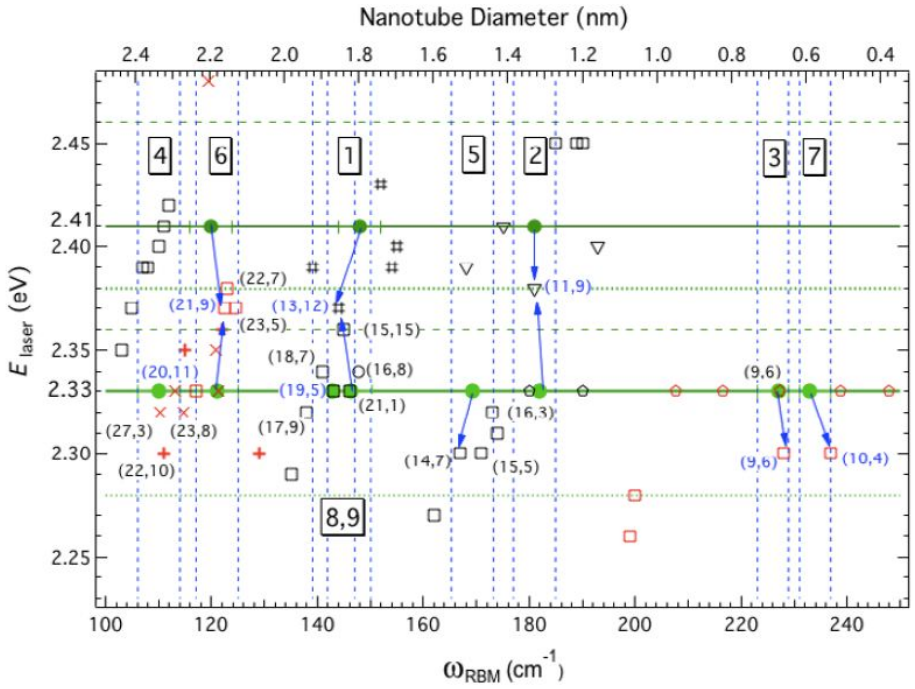

Figure 2.12: Kataura Plot for Raman laser excitation lasers at 2.33eV and 2.41eV. The horizontal dashed lines are the bounds for the excitation laser resonance windows. The vertical dashed lines show a variability in the RBM measurements. This plot assigns tube chirality by mapping the RBM frequencies to a data point within the variability and resonance windows. The RBM is inversely related to the tube diameter. Reprinted from [45] with permission from the Nature Publishing Group.

Bulk growth methods such as CVD generally produce one third metallic CNTs and two thirds semiconducting CNTs [19]. The relationship between chiral angle and growth rate was shown to be linear through the comparison of RBM frequencies to the Kataura plot shown in Fig. 2.12 [45].

The Kataura plot shown in Fig. 2.12, maps transition energies in the electronic density of states of SWNTs to the diameters of the tube. The horizontal dashed lines are

the upper and lower bounds for the resonance windows of the excitation lasers used in Fig. 2.12. The vertical dashed lines, in Fig. 2.12, represent a variability in the measurement of the RBM frequencies. [45] The chirality for each tube is assigned by mapping RBM frequencies to a data point on the Kataura plot that lies within the resonance window and the variability window of the RBM frequency measurement. When multiple chiralities lie in this window the line shape of the G band is examined to determine what type of tube was grown. The G band is referred to the graphitic peak in the Raman spectrum and measures the tangential vibrations of the CNT [33]. An armchair tube and zigzag tube will only have one peak in the G band. Also, the G band line shape is sensitive to metallic and semiconducting tubes, therefore, chirality values are chosen within a single window based on whether the tube exhibited metallic or semiconducting growth characteristics. [45] The plot of growth rate versus chiral angle, is plotted with both experimental and theoretical values in Fig. 2.13. The linear relationship is explained by the amount of dangling bounds available at the growing edge of the nanotube.

If the nanotube is an armchair type, there will be more dangling bonds or steps for additional carbon atoms which results in an equivalent amount of available bonds. Adding a carbon dimer, two carbon atoms bonded together, to an armchair nanotube results in a linear growth rate by shifting its location by one lattice parameter with no change in the kind of bond afterward [45]. However, if the nanotube is zigzag, additional carbon atoms create a configuration which requires more energy to add additional carbon atoms. Examples of armchair, zig zag and chiral SWNTs are shown in Fig. 2.14 to illustrate how the carbon dimers and trimers attach to the leading edge of the CNT.

Another proposed method of controlling the chirality of a SWNT is by controlling the initial nanotube cap formed in the root growth method [47]. A CNT cap consists of six pentagons and some hexagons similar to half a fullerene for small nanotubes such as those with n,m values of (5,5) and (9,0) respectively [47]. The initial

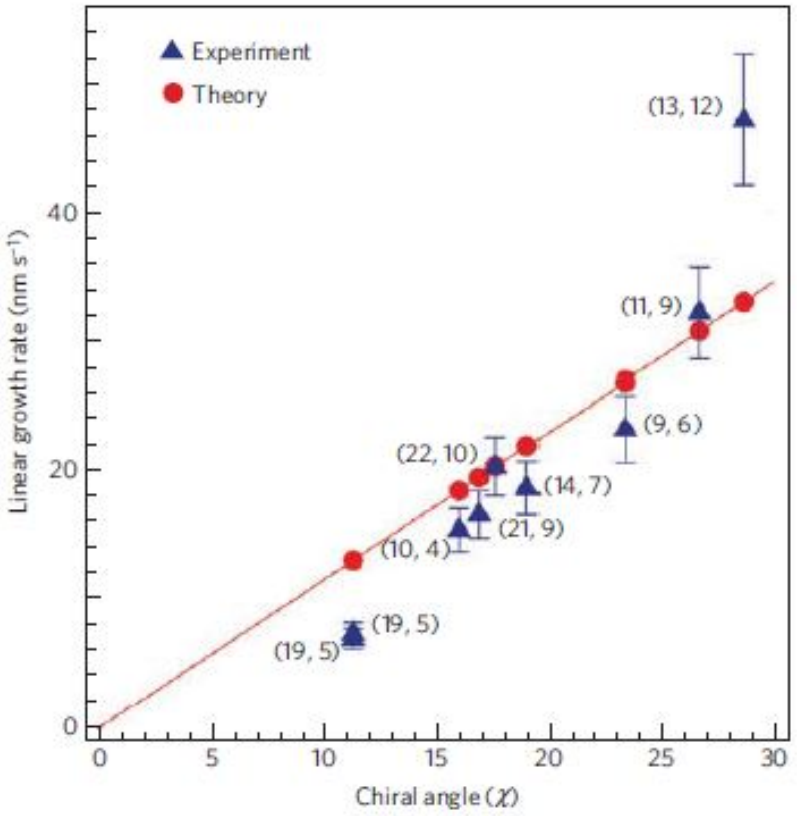

Figure 2.13: The growth rates for individually grown SWNTs were calculated and mapped to chiral angles using the Kataura plot shown in Fig. 2.12. A linear relationship between growth rate and chiral angle was observed. Reprinted from [45] with permission from the Nature Publishing Group.

cap forms from the catalyst as the tube begins to grow. Carbon atoms can easily rearrange while still in contact with the catalyst surface with a migration energy of 0.2eV [47]. After a cap is formed the rest of the CNT continues to grow, pushing the cap off the catalyst. The cap may determine how exactly the rest of the CNT is formed because the tube must bond with the cap, thus determining the tube orientation [47].

2.3.3 Length and Yield Control.

Ultra long CNTs have been grown to lengths greater than 4 cm using the CVD growth method. Most work done in ultra long CNT growth cites tip growth as the growth mechanism [39]. Also, adding a small amount of water to the CVD growth reaction results

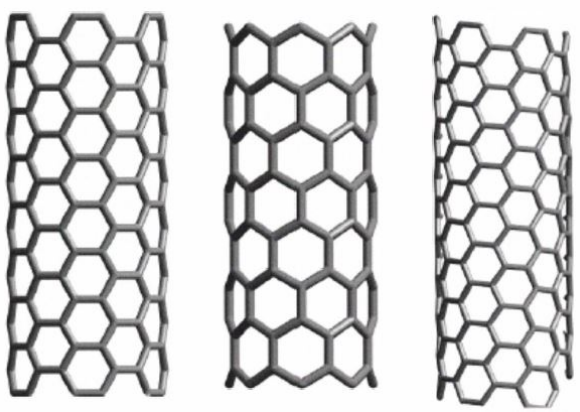

Figure 2.14: Armchair, zig zag and chiral SWNTs are shown left to right respectively. [16] ©2012 IEEE

in long CNTs because water reduces the amount of amorphous carbon that can build up on the catalyst and can inhibit mass loss due to Ostwald ripening [7]. The result is catalysts that are never inactivated and growth yields of up to 99.98% pure SWNTs [39].

Optimizing the reaction feed composition is another area of research in maximizing CNT length. SWNTs of 18.5 cm in length were obtained by using an ethanol precursor and an iron molybdenum catalyst [10]. Also, by controlling the reaction temperature, flow rate and catalyst composition, semiconducting, triple-walled CNTs were grown with 90% selectivity [54].

2.3.4 Overview of Growth Parameters.

This section discusses the controllable growth parameters affecting CNT growth and structure properties. Before optimizing chamber conditions for location specific growth, the parameters affecting the tube structure must be fully understood. Earlier it was shown that chirality is directly related to growth rate. Controlling the growth rate requires precise control of reaction temperature, catalyst composition, and feedstock flow rate [5].

Previous work investigating growth temperature and feedstock gas pressure showed optimal temperature windows for growth and increased CNT length with decreased C_2H_2 pressure [5]. The optimal temperature window shown in Fig. 2.15 is

around 700 °C with an optimal growth rate of $0.2\mu m/s$. The solid line in Fig. 2.15 represents the temperature dependence assuming poisoning of the catalyst at high temperatures and the dashed line represents reduction of the active catalyst state [5].

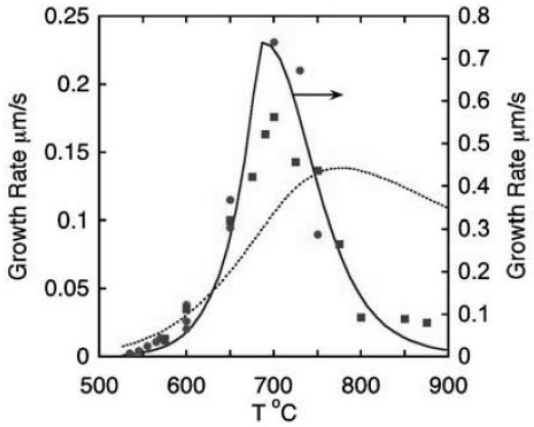

Figure 2.15: Growth Rate dependence on temperature for two sets of metal catalyst films (circles and squares). An optimal temperature is observed for maximizing growth rate in both catalyst materials and temperature is found to reduce growth rate as it is increased beyond the optimal point. Reprinted with permission from [5] ©2005 American Institute of Physics.

The C_2H_2 flow rate also has an affect on growth rate and terminal length. The maximum lengths achieved required lower temperatures as the C_2H_2 flow rate was reduced [5]. The maximum growth rate was achieved by increasing both the temperature and the flow rate as shown in Fig. 2.16. This group also studied CNT length vs time, growth termination at both high and low temperatures and the change from MWNT to SWNT at higher temperatures [5].

The metal catalyst film used for growing the CNTs in this study was a layered almumina, iron molybdenum catalyst [5]. This is an additional parameter to consider when finding relationships between the inputs of the growth system. Only one type of carbon feedstock gas was used in this study but many other studies include a mixture of several gases to determine how to optimize growth rate. Individual studies such as those

shown in Fig. 2.15 and Fig. 2.16 provide valuable information on the basic growth mechanisms and input relationships for CNT growth, however, incorporating techniques from other fields, such as machine learning, will help in optimizing the large number of input ranges and understanding the underlying relationships between growth parameters.

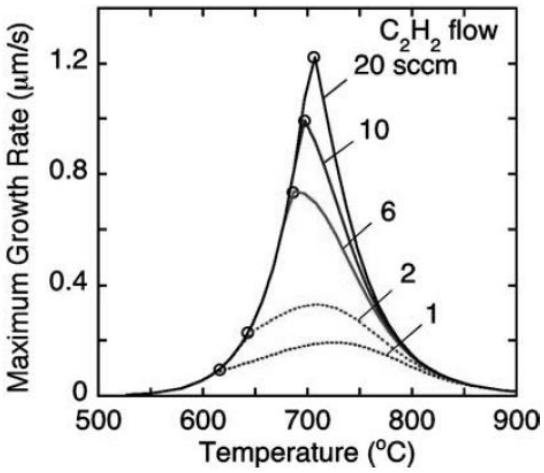

Figure 2.16: The maximum growth rate increases as both temperature and C_2H_2. The carbon activity around the catalyst increases as temperature increases to a limited point where a carbonaceous begins to form on the catalyst. Reprinted with permission from [5] ©2005 American Institute of Physics.

2.4 Introduction to Machine Learning

Machine learning is a subset of artificial intelligence, focused on studying systems with the ability to learn from previous experiences in their environment [48]. According to Arthur Samuel, machine learning is a ”Field of study that gives computers the ability to learn without being explicitly programmed” [48].

This section discusses ways to preprocess data for various machine learning algorithms. SVM classification is introduced for the two class problem and Support Vector Machine Regression (SVR) is outlined to show another use of the SVM algorithm.

Neural networks, the backpropagation algorithm, and the resilient propagation algorithm are also reviewed as regression methods.

2.4.1 Data Preprocessing Techniques.

Data preprocessing is a necessary step in constructing an accurate model using machine learning algorithms. Each feature of the collected data will have varying ranges between samples that can bias the output. Furthermore, collected data might include varying noise from instrumentation or the environment. [14] To enhance the model's ability to accurately classify each class, preprocessing of the data must be performed [21].

Random ordering, mean removal, decorrelation, and covariance equalization are four approaches for transforming data to a usable input dataset [21]. Whether performing none or all of the previously mentioned transformations, the data is typically normalized. The normalization technique can vary, however, a common method is to scale the data either between 0 and 1 or -1 and 1. A common method for normalizing between 0 and 1 is shown in Eq. (2.6) where the value to be normalized is x, $\mathbf{x}$ is the feature vector and $x^{'}$ is the normalized result [21].

$$x^{'} = \frac{x - min(\mathbf{x})}{max(\mathbf{x}) - min(\mathbf{x})} \tag{2.6}$$

In the event that features vary widely across several samples it is important to ensure all features have a variance of 1 [14]. Therefore, all features will have the same influence on the model, regardless of their initial bias. One approach to scale the variance is Pareto scaling, where the standard deviation of each feature is determined and used to replace each feature variance, instead of using the unit variance [14]. Allowing features to be represented by the unit variance amplifies the noise, thus Pareto scaling is a tradeoff between no scaling and unit variance scaling.

Other forms of data preprocessing include: data correction and compression, data transformations, and data validation with known model parameters. Data correction and

compression accounts for the undesirable effects in the data collection process to include signal drift and filtering. Data transformation provides for easy identification of outliers in the dataset. [14] This is difficult because the outliers may be very important data points for creating a well generalized model. Prior knowledge of relationships between features is one way to validate the collected measurements and measure noise in instrumentation and the environment.

2.4.2 Support Vector Machine Classification.

SVMs generate an optimal hyperplane within a multidimensional dataset to distinguish linearly separable classes [11]. The optimal hyperplane is determined by maximizing the margin between each class [21]. In Fig. 2.17 the squares and circles represent two different classes separated by one possible hyperplane. The points on the margin depicted in Fig. 2.17 are the support vectors for the hyperplane [21].

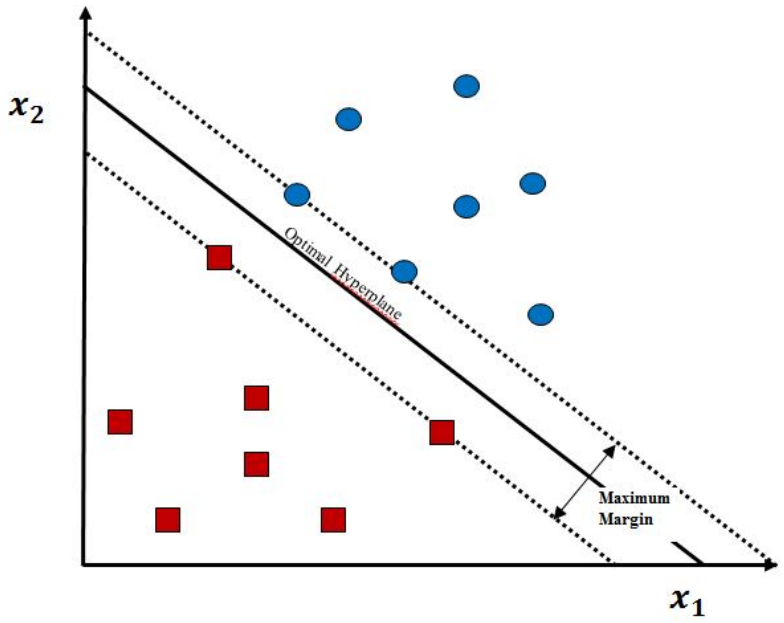

Figure 2.17: SVM classifier of two linearly separable classes (circles and squares). The optimal separating boundary between the two classes is located at the maximum margin between the classes. Recreated from [2].

If the data is not linearly separable then a kernel function is used to transform the data into a higher dimensional space to linearly separate the data as shown in Fig. 2.18.

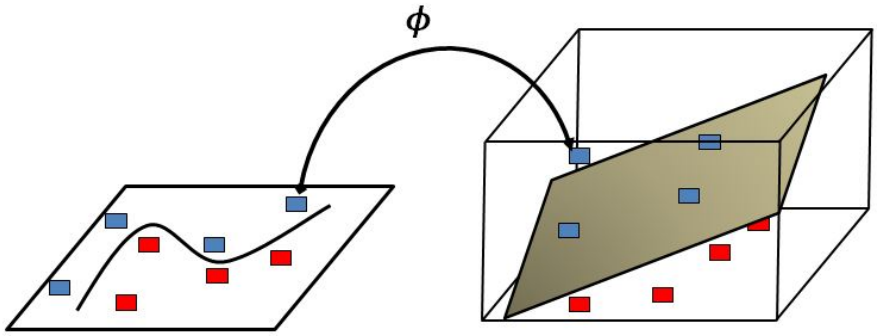

Figure 2.18: Two dimension to three dimension projection using a kernel function, ϕ. The two dimensional data set is not linearly separable and requires a transformation to the three dimensional feature space to become linearly separable. Recreated from [3].

Consider the training data $(x_1, y_1), ..., (x_l, y_l)$ where x_i is the input and y_i is the observed output, where $(y_i \in \{-1, 1\})$. The optimal hyperplane is described by,

$$f(x) = w \cdot x + b, \tag{2.7}$$

where w is the weight vector, b is a bias and x is the input [11]. The optimal hyperplane maximizes the margin, therefore it is the hyperplane described by the convex optimization problem [21]:

$$\begin{aligned} \|w\| &= \sqrt{w_1^2 + w_2^2 + ... + w_N^2}, \\ \text{minimize } & \frac{1}{2}\|w\|^2, \\ \text{subject to } & \begin{cases} (w \cdot x_i) - b & \geq 0 \text{ for } y_i = 1 \\ (w \cdot x_i) - b & \leq 0 \text{ for } y_i = -1, \end{cases} \end{aligned} \tag{2.8}$$

where the goal is to minimize $\|w\|$ while finding a w that satisfies $[y_i(x_i \cdot w) - b] = 0$. The $x_i \cdot w$ represents the dot product between the input and weight vectors and $\|w\|$ is the L2 norm of the weight vector. The convex optimization problem is

solved using the Lagrangian multiplier method that finds a minimum (or maximum), subject to a set of equality constraints [11]. The Lagrange Function, (J), using the constraint and cost function shown in Eq. (2.8) results in Eq. (2.9),

$$J(w, b, \alpha) = \frac{1}{2} w^T w - \sum_{i=1}^{N} \alpha_i \left[y_i (w^T x_i + b) - 1 \right], \tag{2.9}$$

where α_i is the Lagrange multiplier [11], w^T is the transpose of the weight vector and N is the number of training samples.

Taking the partial derivative with respect to w and b, creates a solution that is constrained by α_i as shown in Eq. (2.10) and Eq. (2.11) [11].

$$w = \sum_{i=1}^{N} \alpha_i y_i x_i \tag{2.10}$$

$$\sum_{i=1}^{N} \alpha_i y_i = 0 \tag{2.11}$$

Expanding terms in 2.9 and substituting in Eq. (2.10) and Eq. (2.11) produces Eq. (2.12) [11],

$$J(\alpha_i) = -\frac{1}{2} \sum_{i=1}^{N} \sum_{j=1}^{N} \alpha_i \alpha_j y_i y_j x_i^T x_j + \sum_{i=1}^{N} \alpha_i, \tag{2.12}$$

where $J(\alpha_i)$ is the Lagrange function.

The goal is to find the α_i for all i that maximizes Eq. (2.12) subject to Eq. (2.11) and $\alpha_i \geq 0$ [21]. Once the optimum α_i terms are found, the optimum weights are determined by [21]:

$$w_0 = \sum_{i=1}^{N_s} \alpha_{0i} y_i x_i, \tag{2.13}$$

where N_s are the selected training samples, known as the support vectors, that define the margin. The weights associated with every data point are zero except for the support vector data points which is typically much less than the number of data points [11].

Non-linearly separable data sets are projected to a higher dimensional space using a kernel function. This method is known as the kernel trick because the original data is mapped to an inner product space without having to compute the mapping directly [11]. Various kernel functions exist to perform this operation including the polynomial and radial basis kernel functions [21]. The radial basis function is described by Eq. (2.14) where σ is the variance of the Gaussian function, $\mathbf{x}$ is the mean, and $\mathbf{x}_i$ is the input sample [21].

$$K(\mathbf{x}, \mathbf{x}_i) = \exp \frac{-\|\mathbf{x} - \mathbf{x}_i\|^2}{2\sigma^2} \tag{2.14}$$

The kernel function is represented by $K(x_i, x_j)$ which replaces the x terms in Eq. (2.12) resulting in Eq. (2.15). [11]

$$J = \sum_{i=1}^{N} \alpha_i - \frac{1}{2} \sum_{i=1}^{N} \sum_{j=1}^{N} \alpha_i \alpha_j y_i y_j K(x_i, x_j) \tag{2.15}$$

2.4.3 Neural Networks.

A neural network is a parallel, distributed information processing structure, motivated by biological networks such as the neuron connections of the brain. A neural network consists of neurons interconnected by weighted links that are adjusted to the model data. This adjustment of the neural network topology is similar to how neurons in the brain can die so new ones can grow. Typically a neural network consists of an input layer, several hidden layers and an output layer. [26] The number of hidden layers is determined by trial and error, fitting training data without over fitting the data. An example of a neural network is shown in Fig. 2.19a and an example neuron in a ANN is shown in Fig. 2.19b. Neural networks are useful for problems that involve manipulating multiple parameters to model complex functional relationships. Uses for neural networks include input-output mapping, adaptivity, pattern classification and many others [21].

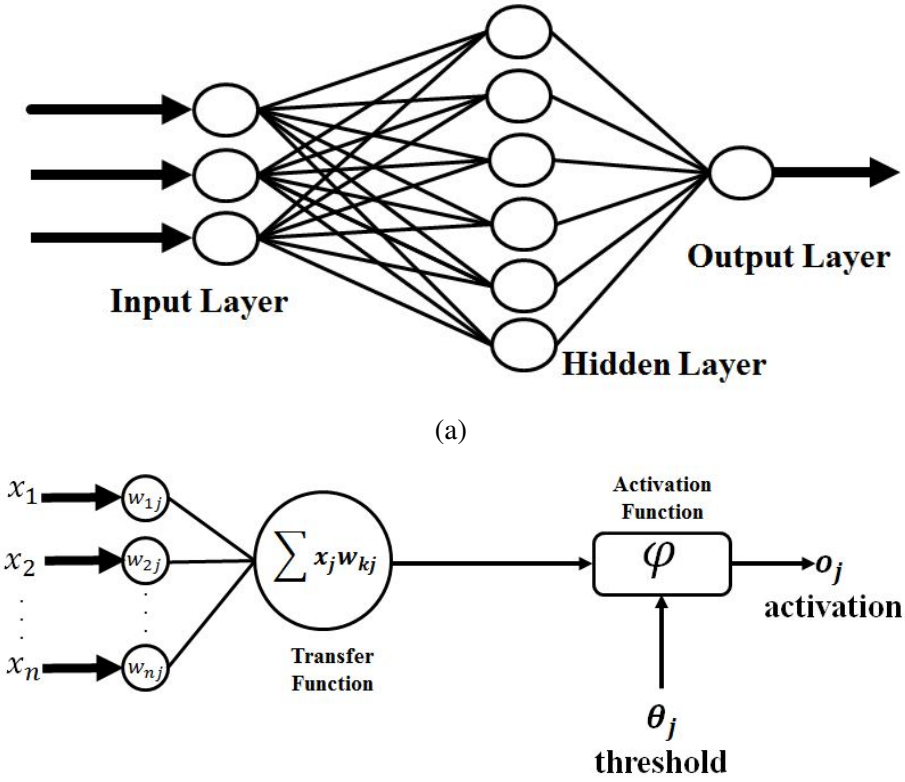

Figure 2.19: (a) An example structure of an ANN with three input neurons, one hidden layer of six neurons and 1 output neuron. (b) A zoomed in view of one individual neuron. The inputs are multiplied by the weights and this product is summed before reaching the activation function where a numerical output between 0 and 1 is produced. Both images recreated from [44].

A neuron k is described by [21]

$$u_k = \sum_{j=1}^{m} w_{kj} x_j, \tag{2.16}$$

$$y_k = \varphi(u_k + b_k), \tag{2.17}$$

where x_j are the inputs, w_{kj} are the weights, m is the number of inputs to the neuron, u_k is the summation of all input-weight multiplications at neuron k as shown in Fig. 2.19b, b_k is the bias, $\varphi()$ is the activation function and y is the output [21]. There are multiple possibilities of activation functions, such as: a threshold function, heaviside function,

piecewise linear function or sigmoid function [26]. The sigmoid function is the most common activation function used in neural networks and is described by Eq. (2.18) [21],

$$\varphi(v) = \frac{1}{1 + exp(-av)} \tag{2.18}$$

where a is the slope parameter of the function allowing the sigmoid function to approximate a threshold function as a approaches infinity and v is the input to the activation function. The activation function ranges from 0 to 1 but it can be adjusted to range from -1 to 1 depending on the application. [21]

The goal of the network is to obtain weights that produce an accurate output for each given input, based on the training set. Once the network is trained, weights learned, a new data set is presented to the network, which predicts outputs based on the previously learned model. This type of configuration is referred to as a feedforward network. [27]

One way of training the network is by the backpropagation algorithm. The current weights of the neural network provide outputs at each layer due to the feedforward process. The error signal at the output layer is calculated as shown: [21]

$$e_j(n) = d_j(n) - y_j(n), \tag{2.19}$$

where the desired signal is $d_j(n)$, the estimated signal is $y_j(n)$, n represents the nth training example and j is jth neuron. Calculating the total error across all output nodes requires the sum of all $e_j(n)$ as shown: [21],

$$E(n) = \frac{1}{2} \sum_{j \in C} e_j^2(n), \tag{2.20}$$

where the set C includes all neurons in the output layer of the neural network. Eq. (2.20) is the error for all output neurons for one sample, to determine the average error for all N samples, known as the cost function, it is computed as shown: [21],

$$E_{av} = \frac{1}{N} \sum_{n=1}^{N} E(n), \tag{2.21}$$

where N represents the number of training samples. The goal of the backpropagation algorithm is to minimize the cost function by adjusting the weights calculated by: [21],

$$\Delta w_{ji}(n) = \eta \delta_j(n) y_i(n), \tag{2.22}$$

where Δw_{ji} represents the change to the weight between neuron j and neuron i, n represents the nth iteration of the training samples and y_i is from Eq. (2.17), the term η is the learning rate parameter of the backpropagation algorithm, and the local gradient $\delta_j(n)$ is described by Eq. (2.23) [21],

$$\begin{aligned} \delta_j(n) &= -\frac{\partial E(n)}{\partial u_j(n)}, \\ &= e_j(n)\varphi_j^{'}(u_j(n)), \end{aligned} \tag{2.23}$$

where u_j is the sum of the weights multiplied by the inputs at each node from Eq. (2.16), $e_j(n)$ is the error for the nth iteration and $\varphi_j^{'}(n)$ is the derivative of the activation function [21]. If neuron j is a hidden node then $\delta_j(n)$ is the product of the derivative of the activation function at that node and the sum of all the previously computed δ in either the next hidden layer or the output layer [21].

Setting the learning rate parameter to a small value will require many steps to reach a solution while a large learing rate parameter will overshoot and oscillate around the optimum point [46]. The resilient propagation algorithm is another training technique with a different weight adjustment method excluding the learning rate parameter. An update value, Δ_{ij}, is introduced for each weight. This value determines the size of the weight update. The resilient propagation algorithm updates according to the cases as shown: [46],

$$\Delta_{ij}^{(t)} = \begin{cases} \eta^{+} * \Delta_{ij}^{(t-1)} & , \text{ if} \frac{\partial E^{(t-1)}}{\partial w_{ij}} * \frac{\partial E^{(t)}}{\partial w_{ij}} \geq 0 \\ \eta^{-} * \Delta_{ij}^{(t-1)} & , \text{ if} \frac{\partial E^{(t-1)}}{\partial w_{ij}} * \frac{\partial E^{(t)}}{\partial w_{ij}} \leq 0 \\ \Delta_{ij}^{(t-1)} & , \text{ else.} \end{cases} \tag{2.24}$$

When the partial derivative of a weight changes its sign, the most recent update was too large and an optimum point was missed. When overshooting of an optimum point occurs, the algorithm decreases the update value Δ_{ij} by a factor of η^-. If the partial derivative keeps the same sign then the algorithm increases the update value by a factor of η^+ to shorten the time until convergence. In Eq. (2.24) η^- is less than 1 and η^+ is greater than 1. [46]

The weight update uses the partial derivative of the weight to determine if a negative or positive update value, Δ_{ij}, should be applied [46]. If the weight partial derivative is positive the error is increased and the weight is decreased by the update value; if the partial derivative is negative the weight is increased by the update value as: [46],

$$\Delta w_{ij}^{(t)} = \begin{cases} -\Delta_{ij}^{(t)} & , \text{ if} \frac{\partial E}{\partial w_{ij}^{(t)}} \geq 0 \\ +\Delta_{ij}^{(t)} & , \text{ if} \frac{\partial E}{\partial w_{ij}^{(t)}} \leq 0 \\ 0 & , \text{ else.} \end{cases} \tag{2.25}$$

For the change of sign of the partial derivative case, the previous update weight is reverted and the stored derivative is set equal to 0. Setting the stored partial derivative equal to 0 avoids an update in the next iteration [46].

2.5 Machine Learning Techniques applied to Carbon Nanotube Synthesis

The synthesis of CNTs involves controlled reactor temperature, carbon feedstock gas flow rate, catalyst composition and a specific substrate material. Useful machine learning techniques applied to a subset of these parameters can create an optimal solution for controlled CNT growth.

Creating a model of the growth reactor is required to predict growth rates, chirality, yield, length, growth orientation and growth location. Research using a genetic algorithm to model a CVD reactor produced a model in good agreement with other growth studies to predict growth rates from a wide range of input parameters. Researchers at the

Clemson University and Army Research Laboratory were able to maximize the amount of CNTs grown while minimizing the amount of deposited amorphous carbon [35]. The search space for this problem is illustrated in Table 2.2 where T_{gas} is the gas temperature, T_{wall} is the reactor wall temperature, P is the reactor pressure, v is the gas velocity at the reactor inlet and X_{CH_4} is the mole factor of methane in the $CH_4 + H_2$ gas mixture [35].

In this group's work, a fitness function was constructed and optimization was performed using the uniform crossover scheme [35]. Table 2.3 shows the optimal values for different weighting factors where I_{CN} is the carbon nanotube deposition rate and I_{AC} is the amorphous carbon deposition rate. The weighting factor is determined by optimizing the genetic algorithm, which is considered a bias variable [35]. A weighting factor of 0.5 gives the best tradeoff between a max CNT deposition rate and a low amorphous carbon deposition rate [35].

Table 2.2: Genetic Algorithm Parameters, recreated from [35].

Parameter	T_{gas} (K)	T_{Wall} (K)	P (atm)	v (mm/min)	X_{CH_4} (mol/mol)
Range	373-973	773-1473	0.25-1.0	50-250	0.02-0.30
Possibilities	32,768	32,768	32,768	32,768	32,768
Binary digits	15	15	15	15	15
Increment	1.831×10^{-2}	2.136×10^{-2}	2.289×10^{-5}	9.156×10^{-3}	8.545×10^{-6}

Another machine learning technique applied to CNT synthesis is a Self-Organizing Map (SOM) to determine CNT diameter. Research performed at Tokyo Metropolitan University was able to use 14 different lasers in the 457-676 nm range to collect data on SWNTs with varying diameters [31]. After collecting data from each unique diameter tube, with each of the 14 lasers, feature reduction was performed using a

Table 2.3: Optimal CVD Parameters recreated from [35].

Weighting Factor	T_{gas} (K)	T_{Wall} (K)	P (atm)	v (cm/min)	X_{CH_4} (mol/mol)	I_{CN} (μ/min)	I_{AC} (μ/min)
0.00	1389.7	773.0	0.25	159.4	0.160	2.9×10^{-3}	5.2×10^{-2}
0.25	1385.5	773.0	0.25	104.5	0.182	2.8×10^{-3}	7.6×10^{-4}
0.50	1380.2	773.0	0.25	114.7	0.178	2.8×10^{-3}	4.7×10^{-4}
0.75	1367.7	773.0	0.25	125.0	0.163	2.7×10^{-3}	3.05×10^{-4}
1.00	782.0	776.4	0.99	186.1	0.028	1.0×10^{-6}	3.0×10^{-16}

discrete cosine transform [31]. This reduced the number of features from 200 to 35. No diameter information was supplied to the SOM and only the discrete cosine transform features and laser excitation level were input to the network. The SOM was able to extract diameter information from the G band structure and the results agree previously performed work [31].

After realizing the benefits of a neural network type approach for classifying tube diameters the research group at Tokyo Metropolitan University also applied a resilient propagation ANN with one hidden layer to predict the diameter distribution [30]. From Table 2.4 the ANN results are very close to the actual RBM results for each tube diameter. The center, (d), and σ are shown here because the Raman RBM analysis fits a Gaussian distribution to each tube diameter [30].

Table 2.4: SWNT diameter comparison of RBM approach and G-Band ANN approach recreated from [30].

Sample	d_{RBM}(nm)	d_{G-Band} (nm)	σ_{RBM} (nm)	σ_{G-Band} (nm)
A	1.050	1.075	0.150	0.156
B	1.174	1.246	0.141	0.140
C	1.297	1.262	0.142	0.143
C	1.297	1.241	0.142	0.143
D	1.393	1.445	0.148	0.150
D	1.393	1.369	0.148	0.148
E	1.467	1.412	0.146	0.144
F	1.561	1.571	0.154	0.154

III. Methodology

The input parameters affecting Carbon Nanotube (CNT) growth, have many complex relationships governing the length, yield, structure and location of growth [39]. Repeated growth experiments may produce different results due to noise from the inputs, defects in the catalyst or defects in the substrate [49, 55]. This thesis presents an approach to control the CNT structure while modeling these complex relationships and providing probabilistic outputs of growth for any experimental input set.

This chapter outlines the CNT growth system hardware and software used for growth and post growth analysis. The data output from the growth system is discussed and preprocessing techniques required for various machine learning algorithms are summarized. Support Vector Machine (SVM) classification and Artificial Neural Network (ANN) regression applied to the growth data are reviewed with their supporting algorithms such as K-Fold cross validation and hyperparameter selection.

3.1 CNT Growth System

Many different approaches exist for growing CNTs, each with their own set of pros and cons. The Chemical Vapor Deposition (CVD) tube furnace method is the most commonly used setup for growing CNTs because of the volume of tubes grown [39]. The growth system used in this thesis is a laser induced CVD system. The heat for CNT growth is provided by a 532 nm CW Verdi V6 excitation laser. This method results in a much smaller volume of CNTs grown and in some cases the growth of a single CNT has been observed.

The growth substrate consists of: 10 μm diameter silicon pillars with a height of 10 μm arranged in a grid on a silicon dioxide substrate. The grid of pillars is divided into 5x5 sub-grids called patches. The pillars are created using deep reactive ion etching of the

top 10 µm of a Si/SiO_2 substrate. The small thermal mass of the pillars allows rapid heating while the oxide barrier between the pillar and the larger substrate prevents heat transfer to the underlying substrate. Figure 3.1a displays the pillars arranged in a 5 x 5 grid. Figure 3.1b shows the view from the microscope where the cross is the current laser position, not centered on a pillar, and the pillars are indicated by the red circles Fig. 3.1b.

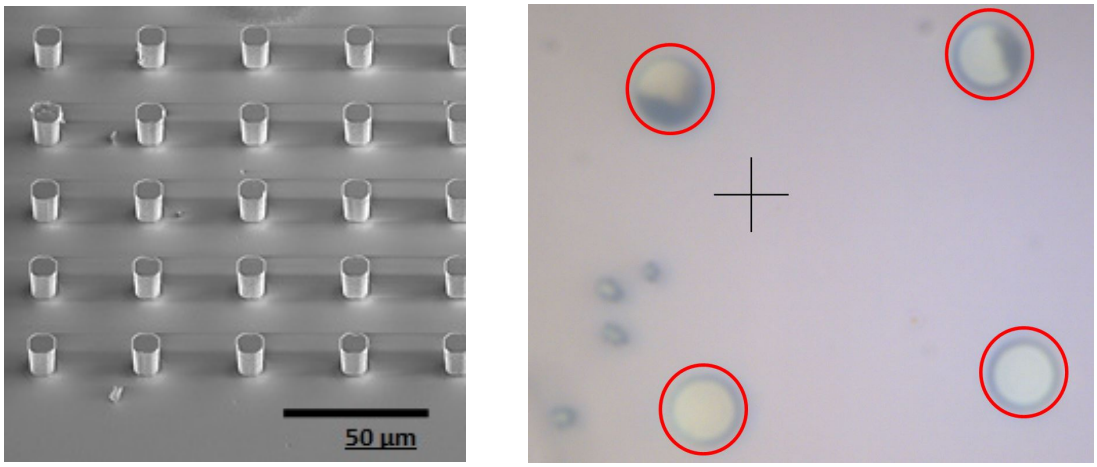

(a) (b)

Figure 3.1: (a) Silicon pillars used for CNT growth referred to as a patch of pillars. Each patch contains a number stamped on the substrate for identification. (b) View from the microscope of four pillars annotated with red circles, within a patch. The laser position is marked by a cross hair that is shown not centered on a pillar. Reprinted with permission from [38].

The catalyst studied in this thesis is 10 nm of alumina ion beam sputtered onto the silicon pillars followed by 1 nm of nickel ion beam sputtered on top of the alumina. The catalyst particle size during growth is unknown because the initial catalyst is deposited as a film. Once the film is heated, the film breaks up into particles, however, measuring the particle size is not possible during growth.

The substrate is placed inside a small vacuum chamber containing a gas input port, vacuum port, and a glass window allowing the laser signal to reach the silicon pillars.

The chamber size is one cubic inch and is mounted on a three-axis stage to allow for proper laser positioning.

The stage can travel two inches in each dimension and the motors have a maximum precision of 0.4 μm. The system software allows positioning the laser at a specific pillar by building a pillar map from three pillar positions. The software controls the stage motors to automatically move the laser from pillar to pillar.

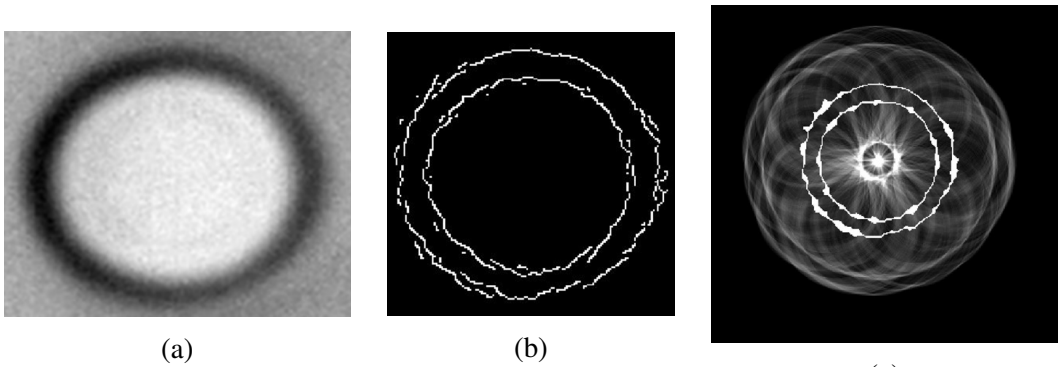

(a) (b) (c)

Figure 3.2: (a) A silicon pillar which must be centered under the laser prior to growth. (b) Canny edge detection on the silicon pillar. (c) Circular hough transform on the Canny edge detected pillar. [38]

Motor slippage induces positioning errors requiring additional laser position adjustments. These additional adjustments require image processing methods to determine the exact center of the pillar. A Canny edge detector is used to find the pillar edges, where a circular hough transform is performed on the edge detected image to determine the center of the pillar. The circular hough transform calculates a circle with the same radius as the pillar at each edge detected pixel. All of these circles intersect in the center of the pillar and an accumulator array is used to track these intersections. The center of the pillar is located at the largest accumulated value. An example is shown in

Fig. 3.2 where Fig. 3.2a is the original pillar, Fig. 3.2b is the result of Canny edge detection and Fig. 3.2c is the result of the circular hough transform.

A Nikon Ti-E microscope focuses the laser signal through a 50X long working distance objective lens creating a 7 µm spot size on the silicon pillar. This microscope includes two optical filter cassettes stacked underneath the microscope output. The laser lightpath passes through the left input port of the microscope and upward through the objective lens to the sample. The reflected laser light from the sample then passes downward through the microscope and out the right port to the Raman spectrometer. A Jobin Yvon Triax 550 spectrometer using an Andor Newton CCD spectroscopy camera is used to collect Raman spectra. Raman spectra between 2000 cm^{-1} and 3000 cm^{-1} are saved at 5 second intervals during growth for a maximum growing time of 300 seconds. Figure 3.3 displays the setup of the entire growth system and Fig. 3.4 shows an example of collected Raman spectra.

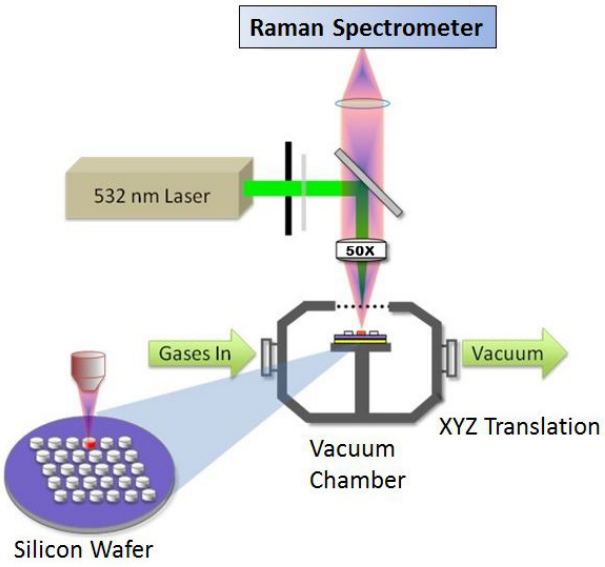

Figure 3.3: CNT Growth System Configuration where a laser is used both for heating a silicon pillar and for in-situ Raman spectroscopy of the grown CNTs. The silicon pillars are under pressure in a vacuum chamber containing a combination of gases to promote growth. Samples consist of 5 by 5 grids of silicon pillars attached to a moveable stage for laser positioning. Reprinted with permission from [38].

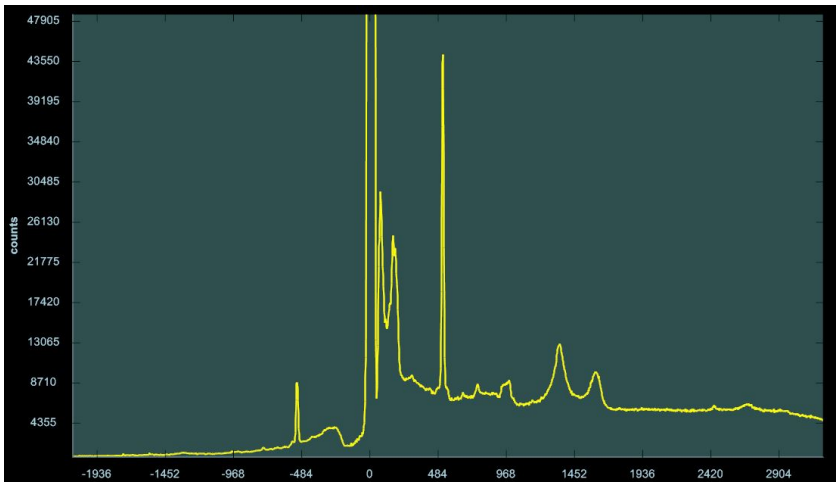

Figure 3.4: Collected Raman Spectra from Multi Walled Carbon Nanotube (MWNT)s. The G and D peaks are shown at $1580cm^{-1}$ and $1340cm^{-1}$ respectively and the Stokes, anti-Stokes peaks are shown at $500cm^{-1}$ and $-500cm^{-1}$ respectively. Reprinted with permission from [38].

Figure 3.3 shows the laser light going down to the sample and reflected back up to the spectrometer however the actual system places the sample upside down with laser light reaching the sample from below. The actual microscope, growth chamber, and gas inputs and outputs are shown in Fig. 3.5, which also shows the multiple objective lenses available for on the microscope. Only the 50X objective lens is used for growth, however, 20X and 5X are available for viewing larger patches of pillars.

The water content in the growth chamber is the only parameter not computer controlled. A test tube of water is fitted with a leak valve to adjust the amount of water vapor entering the growth chamber, as shown in Fig. 3.6. The water content is measured using a Shaw Superdew 3 dew point meter that reports water content to the main experiment software.

To reduce noise and increase the signal received at the Raman spectrometer, the entire system is contained inside a black plexiglass encasing. A floating optics table is also used to reduce vibrations on the sample. The plexiglass encasing around the experiment setup is shown in Fig. 3.7.

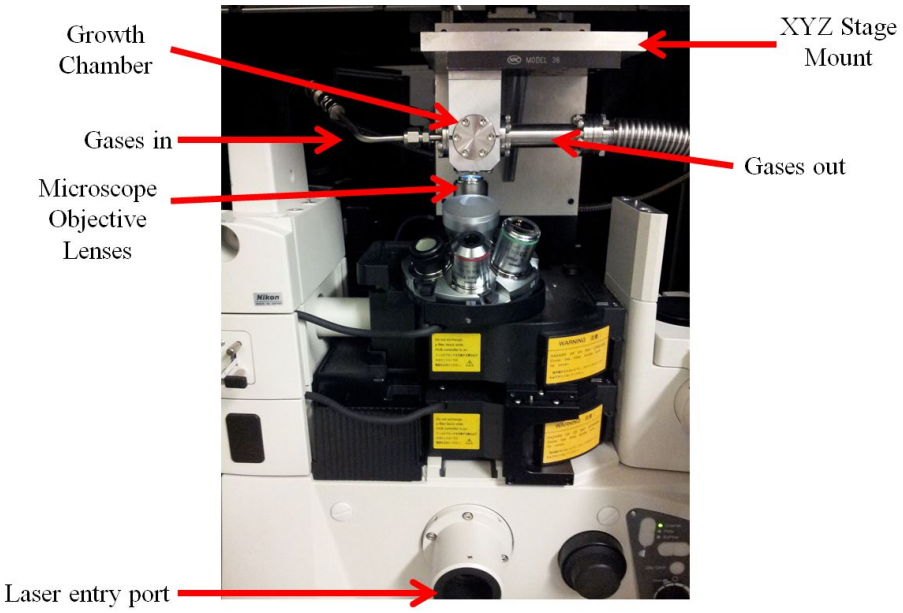

Figure 3.5: The growth chamber has input gases from the left and output gases through the thicker line to the right. The XYZ translation stage is attached to the top of the growth chamber and the microscope with four different objective lenses is shown below the chamber. The laser light enters the microscope through the circular port shown at the bottom of the image and goes up into the growth chamber. [38]

The growth temperature is measured by fitting a Voight lineshape to the Stokes and anti-Stokes peaks found at $\pm 520\,\mathrm{cm}^{-1}$ [9]. The fit is performed using a Levenberg-Marquardt algorithm [41]. The phonon frequency shift is calculated as: [9]

$$\Delta w(T) = \left(\frac{w_s - w_{as}}{2}\right) - w_0, \tag{3.1}$$

where w_s and w_{as} are the Stokes and anti-Stokes frequencies respectively, and w_0 is a constant equal to $528\,\mathrm{cm}^{-1}$. The temperature is found by substituting the phonon frequency shift into Eq. (3.2) and solving for T,

$$\Delta w(T) = C\left[1 + \frac{2}{\frac{\hbar w_0}{e^{2k_BT}-1}}\right] + D\left[1 + \frac{3}{\frac{\hbar w_0}{e^{3k_BT}-1}} + \frac{3}{\left(e^{\frac{\hbar w_0}{3k_BT}} - 1\right)^2}\right], \tag{3.2}$$

where k_B is Boltzmann's constant, $\hbar$ is Planck's constant, C is a constant equal to $-2.96\,\mathrm{cm}^{-1}$ and D is a constant equal to $-0.174\,\mathrm{cm}^{-1}$.

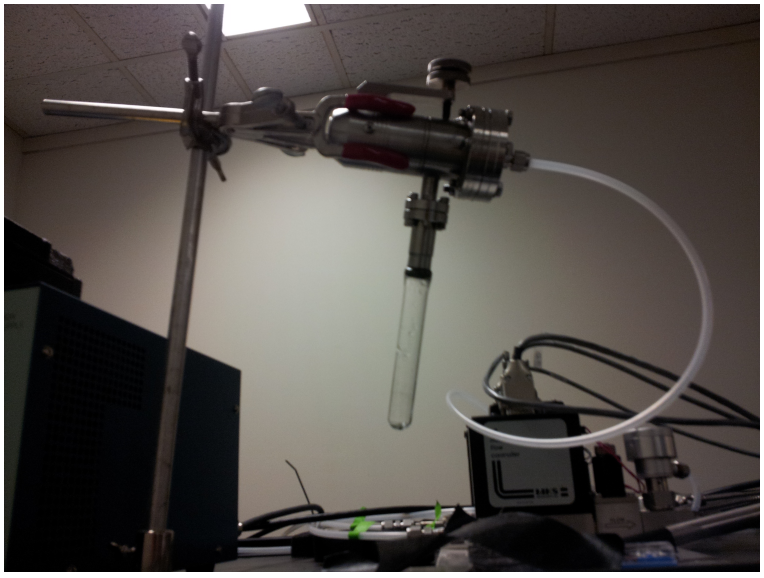

Figure 3.6: The water vapor concentration inside the growth chamber is controlled using a test tube containing water with a leak valve. The leak valve is not computer controlled but the water concentration is measured using a Shaw Superdew 3 dew point meter. [38]

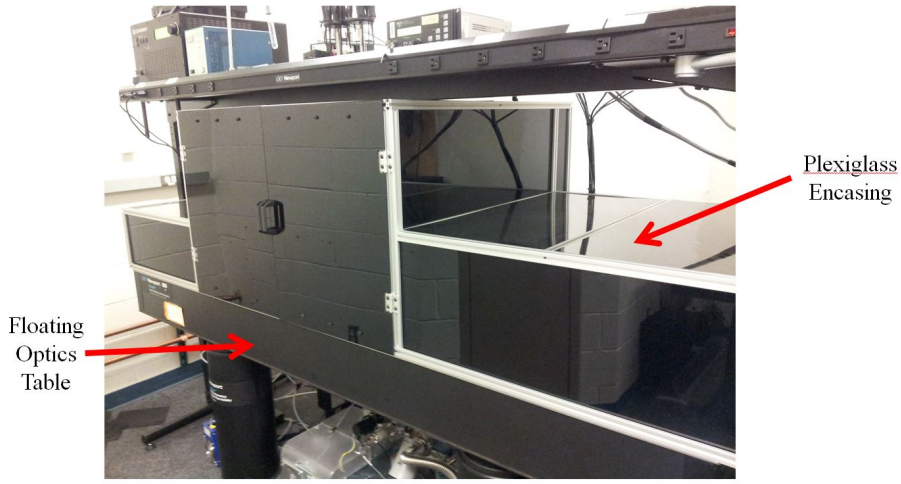

Figure 3.7: To reduce noise the CNT growth system is encased in a black plexiglass box. The entire system is placed on a floating optics table to reduce vibrations on the sample. [38]

After the experiment concludes the growth rate and catalyst lifetime are calculated from the collected Raman spectra. The G peak intensity, located at 1580 cm^{-1},

is integrated to determine the growth rate and catalyst lifetime. An exponential equation is fit to the integrated G peak intensity to determine these parameters as shown: [41],

$$G(t) = \nu\tau\left(1 - e^{\frac{-t}{\tau}}\right), \tag{3.3}$$

where ν is the initial growth rate, τ is the catalyst lifetime and t is the time elapsed since the start of growth. An example fit on growth data is shown in Fig. 3.8.

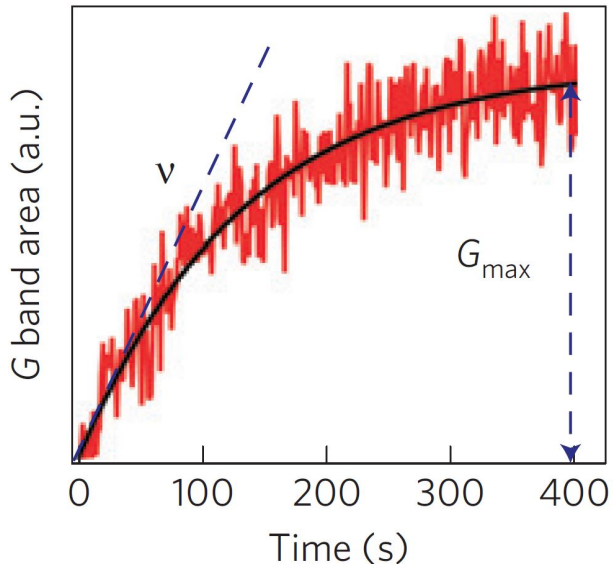

Figure 3.8: The area under the G peak is integrated across time to create the red growth rate curve shown. The red growth rate curve is fitted with Eq. (3.3) to determine the growth rate, ν, and time constant, τ. At time = 400s, the red growth rate curve stops increasing signaling the end of growth and making $\tau = 400$ sec. G_{max} is the maximum theoretical growth height calculated as $\nu \times \tau$. Reprinted from [45] with permission from the Nature Publishing Group.

3.2 Machine Learning Techniques

The data gathered from each CVD growth is used to train an SVM Single Walled Carbon Nanotube (SWNT) vs. MWNT classifier and a regression ANN for predicting the growth rate. The percentage of carbon in a growth reaction is an important feature in growing CNTs, therefore, the partial pressures of each input gas are used instead of flow

rates to better represent the proportions of each gas in the growth chamber. The input gases consist of: Argon, Ethylene, Hydrogen, and a 99:1 ratio of Argon to Carbon Dioxide. The partial pressure of each gas is calculated as:

$$p_i = \left(\frac{f_i}{\sum_{i=0}^{N} f_i} \right) P_T, \tag{3.4}$$

where p_i is the partial pressure of gas i, f_i is the flow rate of gas i in Standard Cubic Centimeter per Minute (SCCM)s, N is the number of gases, and P_T is the total chamber pressure. The sum of the partial pressures will equal P_T.

3.2.1 Support Vector Machine Classifier.

The SVM classifier requires training data labeled with a class designator. The three class designators are SWNT, MWNT, and SWNT/MWNT. The parameters used to train this classifier are: Ethylene, Argon/Carbon Dioxide, Hydrogen, growth temperature, and water concentration. Two models are constructed from the three classes to form two, two class problems. The first model is the SWNT class compared against the MWNT class and the second model is the SWNT/MWNT class compared against the MWNT class. The training data is truthed by visual inspection of the Raman spectra during growth.

The Raman spectra of SWNTs has been extensively studied and many of the tube features are extracted from the spectra. The tube diameter is proportional to the Radial Breathing Mode (RBM) located at $< 200cm^{-1}$. The D peak located at $1340cm^{-1}$ is a measure of the disorder in the tube. The G peak located at $1550 - 1600cm^{-1}$ corresponds to the tangential vibrations of the carbon atoms. The G peak is decomposed into 2 peaks, G+ and G-. The G+ peak is related to the vibrations along the nanotube axis while the G- peak corresponds to vibrations along the circumference. The G peak is used to classify MWNTs and SWNTs because SWNTs will show distinct G+ and G- peaks as shown in Fig. 3.9 while MWNTs will show one broad peak with a lower intensity as shown in Fig. 3.10. MWNTs will also show a similar intensity D peak because of a convolution of

concentric inner wall D peaks. [33] Using this information training samples are labeled as SWNT or MWNT, however, both SWNTs and MWNTs can be observed when a high intensity G peak is seen with a broad range. Samples without the G+ and G- peaks are not labeled as strictly SWNTs.

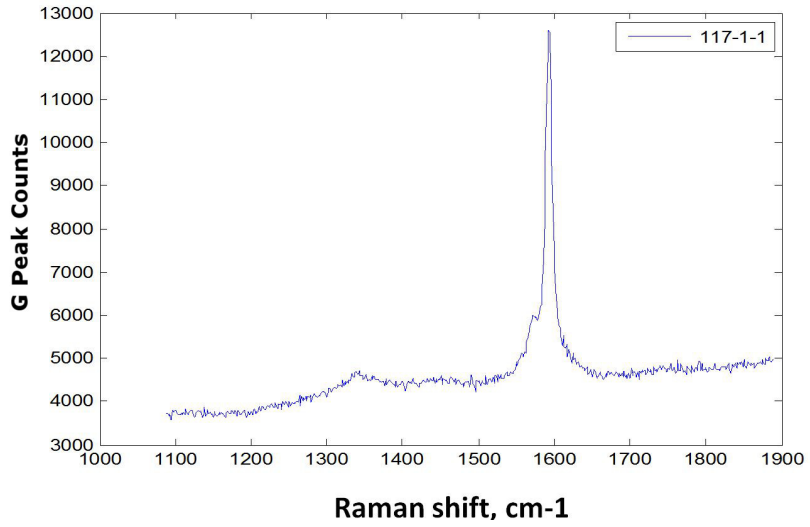

Figure 3.9: SWNT Raman Spectra displaying a sharp G peak and a low intensity D peak. Reprinted with permission from [38].

The SVM classifier is trained using custom written Java code leveraging the Sequential Minimal Optimization (SMO) algorithm within Waikato Environment for Knowledge Analysis (WEKA) [36, 42]. WEKA is freely available software containing a variety of machine learning algorithms including clustering, classification, regression and feature selection. The training data is formatted to an Attribute Relationship File Format (ARFF) allowing a standard file format for all of the machine learning algorithms within WEKA to operate on the data set. [36]

WEKA normalizes the input data between 0 and 1 prior to entering the SVM algorithm. An equal number of experiments from each class are used in the training data. If the two classes contained unequal numbers of training examples the classifier will bias

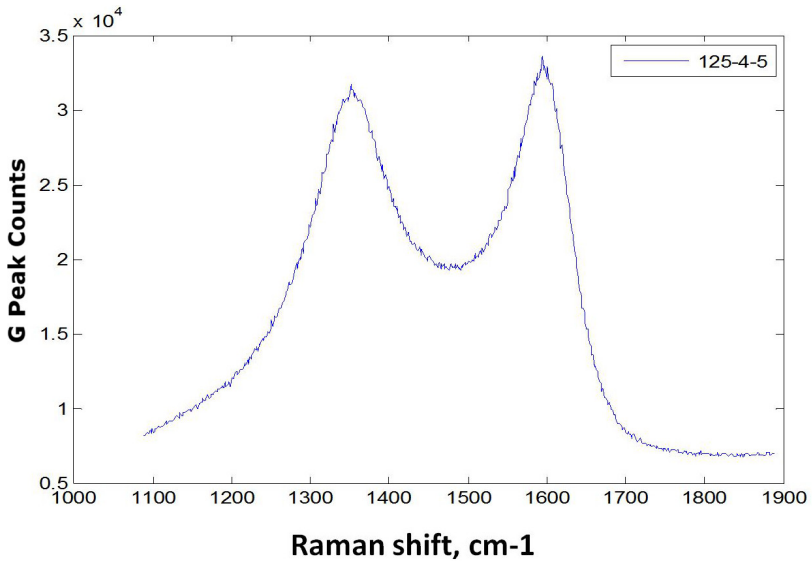

Figure 3.10: MWNT Raman Spectra displaying broad G and D peaks. Reprinted with permission from [38].

towards one class. K-Fold cross validation is implemented within WEKA to create a more generalized model. The algorithm for K-Fold cross validation is shown in Algorithm 1. For K-Fold cross-validation, K models are constructed and each model trains on a different partition of the training set. An example is shown in Fig. 3.11 where K = 3. Each model never trains on the testing data in the associated fold allowing each model to only see a portion of the total training data.

A Radial Basis Function (RBF) kernel is used to project the nonlinearly separable data to a higher dimensional feature space. The RBF kernel requires the user to set two parameters: the gaussian variance, σ, and the cost function term, C. The cost function term is related to the confidence in the training samples. If all of the training samples are labeled correctly then C can be increased making the classifier perfectly classify each instance while increasing the complexity of the model. When the possibility exists for mislabeled training samples then C should remain low to reduce the complexity of the model. The cost function is kept at 1 for the training data used. The training data is

Algorithm 1: K-Fold Cross Validation [21]

Input: $S_o = (x_0, y_0)..., (x_n, y_n)$,Training Data

$M_o, ...M_K$, K Previously Built Models

output: $\bar{E}$, Average Error for K Models

/* Partition S_o into K disjoint sets,B_K, with equal distributions of each class in each set */

B = split(S_o,K);

Build K models: $M_0, ...M_{K-1}$;

for *i from 1 to K* **do**

    // Use B_i for testing and the remaining D_i for training

    $D_i = S_o - B_i$;

    // Train model, M_i with D_i

    train(M_i,D_i);

    // Test trained M_i on B_i

    e_{B_i}=test(M_i, B_i);

$\bar{E} = \frac{1}{K} \sum_{i=1}^{K} e_{B_i}$;

correctly labeled however similar experiments produce different results because of unknown factors affecting growth.

The gaussian variance, σ, is determined by testing models with varying σ terms and finding one which maximizes accuracy while minimizing the number of support vectors. Figure 3.12 shows the resulting support vectors and corresponding accuracy for various σ values. In Fig. 3.12, σ equal to 28 maximizes the accuracy while minimizing the number of support vectors. The cost function parameter, C, is held constant at 1 for all model testing in Fig. 3.12.

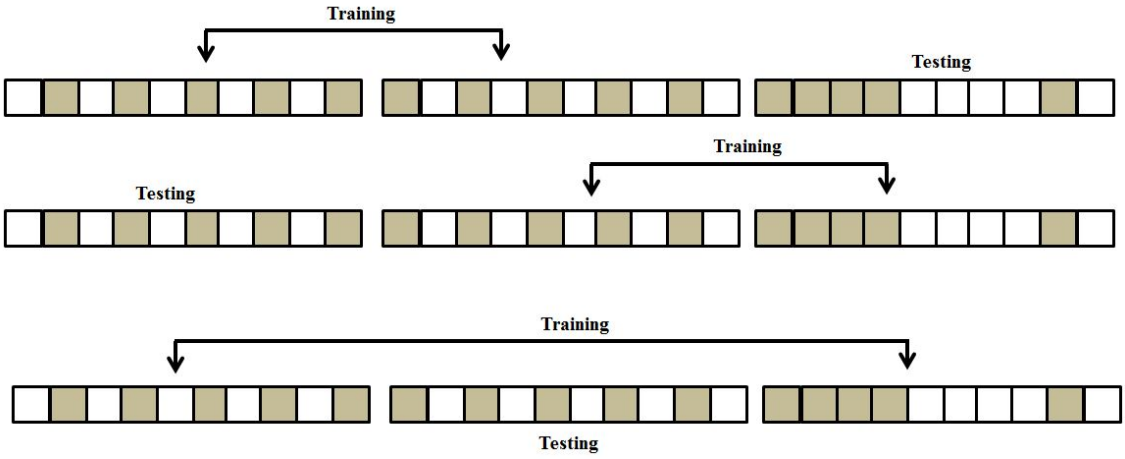

Figure 3.11: K-Fold cross-validation where K = 3 and each fold has different training and testing data. The shaded boxes represent one class and the white boxes represent the other class. Each bin in each fold contains an equal number of training samples from each class. Recreated from [1].

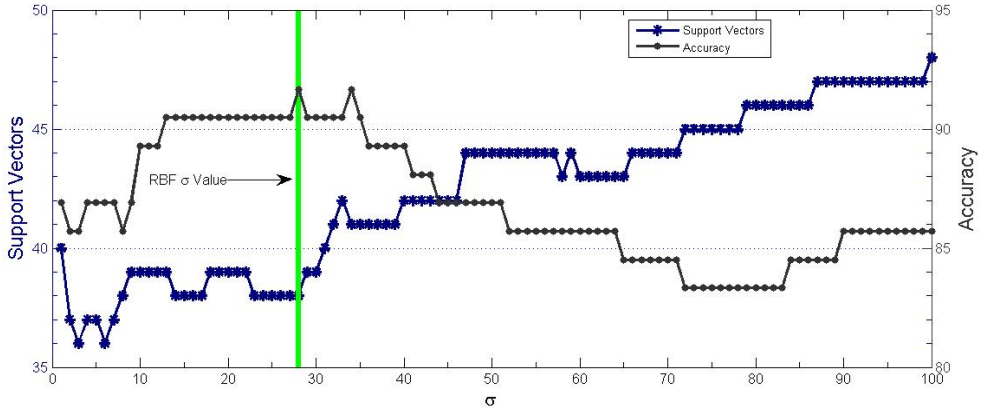

Figure 3.12: The RBF kernel variance, σ is varied between 1 and 100 to produce 100 different classifiers for the training data. The classifier with the fewest support vectors and highest accuracy is chosen, annotated by the vertical green line.

The SVM classifier, whose σ parameter is determined as shown in Fig. 3.12, is tested across the entire input growth parameter space to find regions with higher probabilities of SWNT growth. The experiments, defined as growth parameter input

values, are used to validate the classifier based on a minimum and maximum value and the resolution of each growth parameter, as shown in Table 3.1. The classifier determines which class each experiment corresponds to and produces a probability of the experiment existing in either class. The probability is based on the experiment's euclidean distance from the SVM decision boundary. Experiments lying close to the boundary will have a probability closer to 50% due to the higher probability of misclassification. As experiments move further from the decision boundary the probability increases. [43]

Experiments with a 90% probability of being in either class or greater are kept to determine trends in SWNT growth. This approach also produces a subset of experiments from the large experiment set created using Table 3.1. The subset of experiments are predicted to grow SWNTs with a high probability and bound the growth parameter space. The bounded growth parameter space is explored in further detail to predict SWNT growth rates using an ANN.

Table 3.1: Parameter ranges and resolution for testing the SVM classifier. The combination of all possible experiments using these ranges and resolutions results in 531,201,645 unique experiments.

	Minimum	Maximum	Resolution
Ethylene (Torr)	1	40	1
Hydrogen (Torr)	1	40	1
Argon/Carbon Dioxide (Torr)	1	40	1
Temperature (°C)	300	1200	20
Water Concentration (ppm)	1	200	1

An example output from the SVM classifier is shown in Fig. 3.13 where temperature is varied while all other growth parameters are held constant at the values shown in Table 3.2. Figure 3.13 shows the temperature vs probability plot and indicates a maximum value in probability occuring at 480° C. Displaying the SVM classifier by adjusting only one parameter allows comparisons to other established models of CNT

growth including Puretzky's work described in Chapter 2 and Wood et al.'s work shown in Fig. 3.14. Figure 3.14 shows the number of walls precipitated from a catalyst is based on input carbon flux [5, 56]. Varying the ethylene partial pressure and monitoring the temperature with the highest probability of SWNT growth provides a comparison between Fig. 3.13 and Fig. 3.14. Ethylene partial pressure cannot be directly compared to carbon flux, however, the model illustrates the relationship between higher ethylene partial pressure and higher temperature is in good agreement with Fig. 3.14.

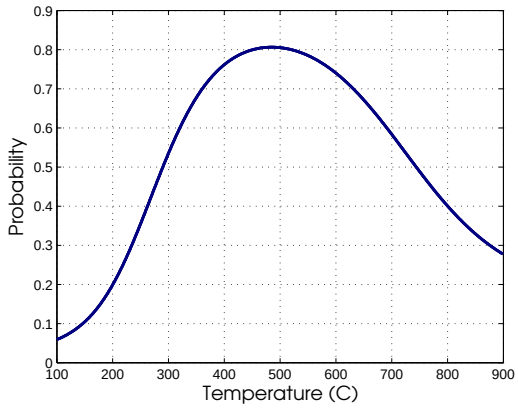

Figure 3.13: Adjusting temperature while keeping all other growth parameters constant to the values shown in Table 3.2 and recording the probability of SWNT growth results in the temperature probability curve. Adjustment of each growth parameter changes the shape of the probability curve and this curve can be plotted for each growth parameter while keeping all other parameters constant.

Growth Parameter	Value
Ethylene	5 Torr
Hydrogen	5 Torr
Argon/Carbon Dioxide	5 Torr
Water	10 ppm

Table 3.2: The growth parameters used to generate Fig. 3.13 are shown. Only temperature is adjusted in this analysis.

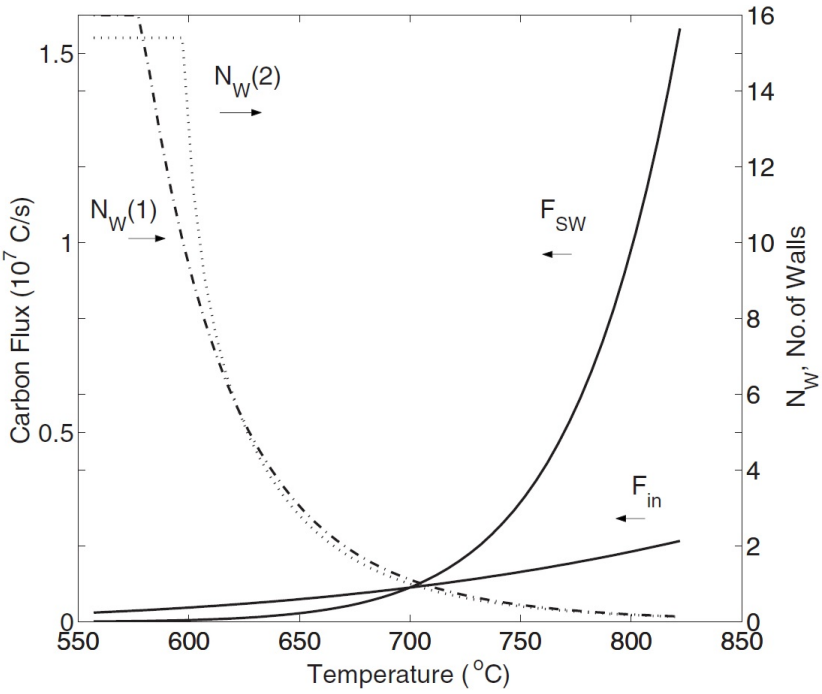

Figure 3.14: The number of walls from a single catalyst is determined by the amount of carbon flux, F_{in} (slowly increasing solid dark line), into the catalyst versus the optimal amount of carbon flux, F_{SW} (exponentially increasing solid dark line), needed for SWNT growth. If more carbon is input to the catalyst than is needed more than 1 wall is grown. Where F_{SW} and F_{in} intersect is exactly where SWNT growth will occur. The dash line, $N_W(1)$ illustrates the number of walls precipitated from a catalyst and $N_W(2)$ (dotted line) shows a previous model of the number of walls predicted to precipitate from a catalyst. Reprinted with permission from [56]. ©2007 The American Physical Society

3.2.2 Artificial Neural Network Regression.

The growth rate prediction training data contains two additional features: growth rate and catalyst lifetime. Before any training is performed the relationship between growth rate and catalyst lifetime must be verified. These two parameters are inversely related and the training data must show this relationship to validate the data points. Figure 3.15 shows growth rate, ν, plotted against catalyst lifetime, τ, and the inverse relationship is described by the equation fitting the data.

The data is preprocessed by removing the mean and standard deviation, randomly reordering the data, and normalizing between 0.1 and 0.9. Shuffling the data helps to

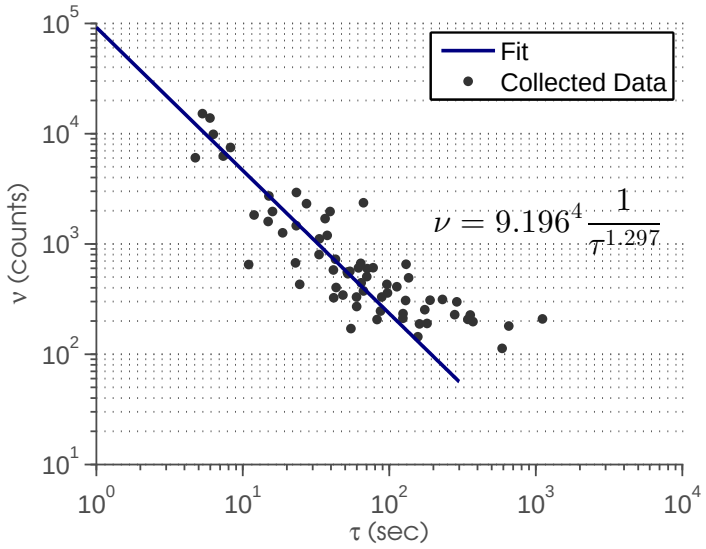

Figure 3.15: ANN training data showing the inverse relationship between growth rate,(ν) and catalyst lifetime, (τ). Training data that does not fit this relationship contains an error in the growth rate or catalyst lifetime measurement. The equation governing the growth rate/catalyst lifetime relationship is shown in the figure.

reduce any biases that may exist in any partition of the data. Scaling between 0.1 and 0.9 ensures the activation functions are not receiving inputs at their minimum or maximum values allowing each input to have an effect on the overall weighting of the ANN. Training the ANN utilizes a K-Fold cross-validation to generalize the model while reducing the training error [51]. The shuffled and normalized data is sorted into a training and testing set. The training set is 80% of the original data, where the testing set is the remaining 20%. The K-Fold cross validation algorithm shown in Algorithm 1 for SVM training is similar to the K-Fold cross validation for neural network regression, however the samples are not labeled for the regression case.

In addition to the testing and training sets, a validation data set is used to test all K networks. The validation data set is the same for all networks and isn't included in the training or testing sets. The goal of the validation data set is to determine which of the K networks performs best without overfitting the data. Choosing data points for the

validation set is difficult because uneven sampling across the parameter space will result in a bias towards one network over others. An easy way to select these points is to randomly select points before partitioning data into training and testing sets however this may also induce a bias based on the shape of the training data. Another approach is to determine which features have the most impact on results and use these features to dictate how validation data is selected. Previous work on CNT synthesis has shown a strong relationship in growth characteristics based on temperature, ethylene and water concentration [5, 52]. The data points containing the minimum, maximum and median of temperature, ethylene and water concentration are used for the validation data.

Figure 3.16 shows an example of K-Fold cross validation training with K = 3. The training error decreases across all epochs but the testing and validation error increase slightly implying the model may have over fit to the training data beyond this point.

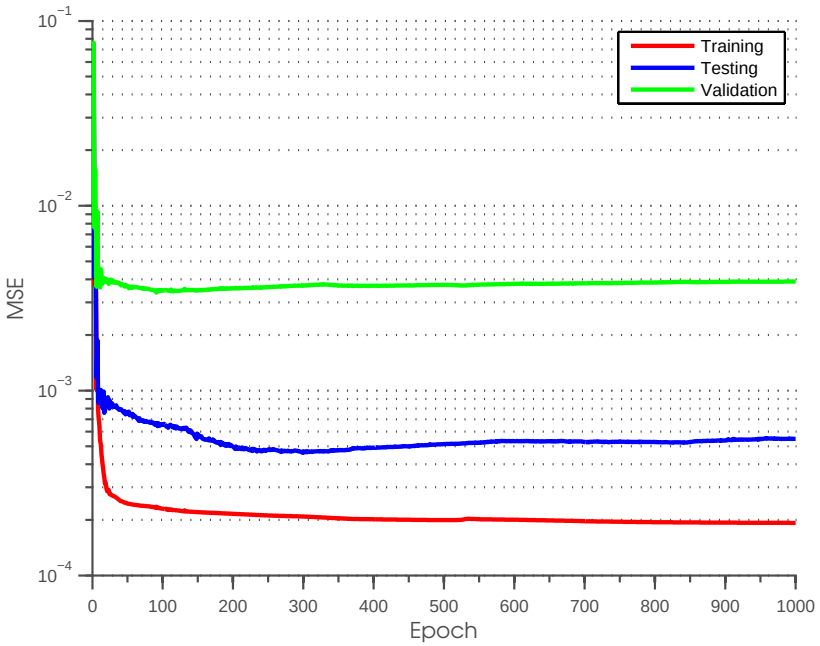

Figure 3.16: MSE curves of K-Fold cross-validation for training, testing and validation. The model begins to train to the data as shown by the increase in testing and validation MSE while the training MSE continues to decrease.

The max theoretical growth height of CNTs is a product of the growth rate and catalyst lifetime, $\nu\tau$ [15]. Work performed by Futaba et al. determined a relationship between water concentration, ethylene and maximum growth height shown in Fig. 3.17 [15]. The model constructed to fit the data shown in Fig. 3.17 determined an optimal water to ethylene ratio to enhance catalyst activity reducing the amorphous carbon formation [15]. The ANN model is able to extract this relationship after training and querying the model across the growth rates considered in the work performed by Futaba et al. [15].

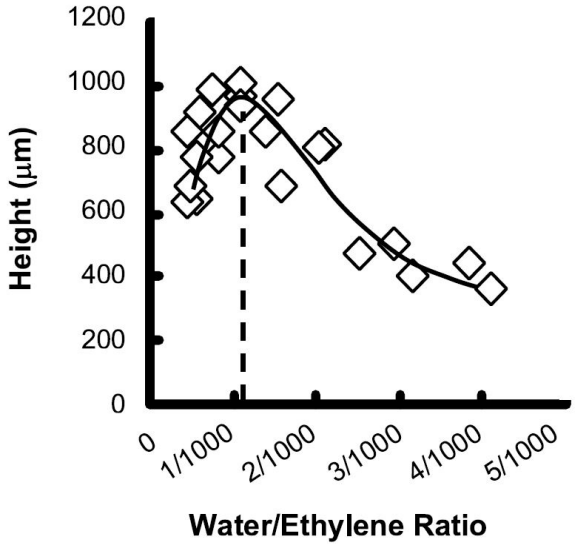

Figure 3.17: Plot of the maximum height as a function of the water/ethylene ratio where the boxes are the collected data points and the curve is a fit to the data. This shows the important relationship between water and ethylene for growing long CNTs. The vertical dashed line is the maximum growth height predicted. Reprinted with permission from [15]. ©2005 The American Physical Society

Encog is a machine learning framework for Java, C++ and .Net applications that supports Bayesian Networks, Hidden Markov Models, SVMs and ANNs [13]. The resilient propagation learning technique is the fastest implemented training algorithm within the Encog framework. The framework supports multithreaded training and can also utilize the Graphics Processing Unit (GPU) to increase the training speed. [13]

A .Net application is utilized to build, train, and test various ANN architectures using the Encog framework. The designed application allows network visualization and saving network weights for querying the network later. The application multi-threads the K-Fold cross validation training to increase training speed.

3.3 Experiment Prediction and Single Walled Carbon Nanotube Probability

The trained SVM classifier and ANN regression model are combined to find experiment parameters for a desired growth rate. Predicting experiment parameters for a specific growth rate results in controlling the CNT chiral angle and therefore the metallic or semiconducting tube type. The ANN regression model is trained using growth parameters as inputs and growth rates as outputs. The result of this network configuration allows multiple growth parameters to map to a single growth rate.

A lookup table is constructed by varying each growth parameter by the range shown in Table 3.3 and querying the trained ANN regression model. Each entry in the lookup table contains a set of growth parameters, a growth rate and the probability of SWNT growth based on one of the two SVM classifier models discussed earlier. The lookup table is searched for all entries containing a specific growth rate. This reduced list of experiments are sorted based on the SWNT growth probability returning experiments with the highest probability of SWNT growth for a specific growth rate. Another use of the lookup table involves sorting by growth rates to determine the largest growth rate experiment configuration within a predetermined SWNT growth probability confidence bound. This approach is useful for maximizing SWNT growth rates and shortening the growth time.

The ANN regression model is also compared to the work of Puretzky et al. and Wood et al. by varying growth temperature and holding all other parameters constant. Growth rate curves are generated for the entire temperature range as shown in Fig. 3.18 where local growth rate maximums are observed similar to the observations by other

Table 3.3: Parameter ranges and resolution for building the ANN lookup table.

	Minimum	Maximum	Resolution
Ethylene (Torr)	1	40	1
Hydrogen (Torr)	1	40	1
Argon/Carbon Dioxide (Torr)	1	40	1
Temperature (°C)	500	900	20
Water Concentration (ppm)	1	200	1

groups [5, 56]. Growth temperatures below $600°C$ have not been observed for the configuration in Fig. 3.18, making all growth rate predictions below this temperature an extrapolation subject to large modeling errors. As more experimentation is performed in these regions the predicted and actual growth rate results will converge.

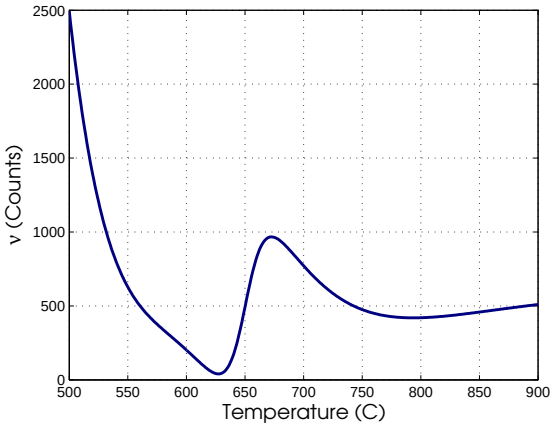

Figure 3.18: Setting ethylene = 8 Torr, hydrogen = 10 Torr, argon/carbon dioxide = 5 Torr and water concentration = 31 ppm and varying temperature results in the growth rate curve shown. Low temperature values are extrapolations in this configuration resulting in large predicted growth rates.

3.4 Summary

This chapter summarizes the processes required to create a predictive growth rate model used in parallel with the laser induced CVD growth system for growing strictly

semiconducting or metallic SWNTs. Growing MWNTs occurs with slight changes in growth parameters, therefore, growth parameters only resulting in SWNT growth are determined first. An SVM classifier trained using SWNT and MWNT growth experiments determines if an experiment will result in SWNT growth. This classifier ensures only SWNT growth experiments are considered for chiral-selective growth.

A predictive ANN trains on SWNT growth experiments to predict growth rates based on growth temperature, water concentration, ethylene, hydrogen and argon/carbon dioxide partial pressures. The ANN training utilizes K-Fold cross validation to prevent the model from overfitting the data. A lookup table is required because the goal of the ANN regression model is to return growth parameters for a desired growth rate. The lookup table returns a list of experiment configurations for a desired growth rate and these configurations are sorted based on the SVM classifier probability of SWNT growth.

The combination of the SVM classifier and ANN regression model allows exploration of growth rate experiments with the highest likelihood of SWNT growth. In the next chapter, the SVM classifier and ANN regression will be applied to collected CNT growth data. The results will show the growth parameter regions predicting SWNT growth generated from the SVM classifier and the ANN regression model will be used to grow SWNTs with metallic or semiconducting properties.

IV. Results and Analysis

An automated growth system developed at Air Force Research Laboratory (AFRL) increases experimentation speed by a factor of 100, however, this still is insufficient in an experimental search of every combination of all growth parameters. An intelligent approach to optimize experimentation parameters to characterize growth parameters for specific growth rates is desired. The growth rates considered are for Single Walled Carbon Nanotubes (SWNTs)s, therefore, a classifier is necessary to determine experimentation parameters for SWNT growth. This reduced set of SWNT experiments is used for growth rate prediction.

This chapter presents the results of the Support Vector Machine (SVM) classifier and Artificial Neural Network (ANN) regression of SWNT growth rates. The SVM classifier results are described and compared against related work on different growth systems. This includes different combinations of the four classes: SWNT, Multi Walled Carbon Nanotube (MWNT), both SWNT and MWNT and no growth, for one vs. all classification. The ANN growth rate regression results present growth rates for highly probable accurate prediction possibilities, as well as defining poor model performance areas, requiring additional training data.

4.1 Support Vector Machine Classifier

The SVM classifier determines Carbon Nanotube (CNT) growth experimentation parameters that result in SWNT growth. The training data consists of four classes: SWNT, MWNT, both SWNT and MWNT, and no observed growth.

4.1.1 SWNT vs MWNT Classifier.

The SWNT and MWNT class data is used to construct a classifier for determining SWNT growth. This classifier ignores experiments generating either no

growth or a combination of SWNTs and MWNTs. The training data statistics are shown in Table 4.1 and Table 4.2 for the SWNT and MWNT classes respectively. The MWNT class consists of 34 MWNT growth experiments and the SWNT class consists of 87 SWNT growth experiments. The cost function utilized in the SVM training algorithm is adjusted to prevent biasing due to the unequal number of samples per class.

Table 4.1: The training data used in the SWNT vs MWNT classifier contains SWNT growth experiments with the statistics shown. This highlights the range of growth parameters used to grow SWNTs and for training the SVM classifier.

	Min	Max	Mean	Std. Deviation
C_2H_4 (Torr)	1.008	8.13	3.577	1.69
H_2 (Torr)	2.37	18.86	8.32	3.93
Ar/CO_2 (Torr)	1.61	13.008	5.72	2.71
Temperature(° C)	420	872.74	689.16	109.47
H_2O (ppm)	2.1	110	28.65	29.43

Table 4.2: The training data statistics for the MWNT class in the SWNT vs MWNT classifier are displayed. The range of growth parameters used to grow MWNTs is similar to the parameter ranges for SWNT growth.

	Min	Max	Mean	Std. Deviation
C_2H_4 (Torr)	3.04	8.69	6.84	2.5
H_2 (Torr)	7.07	18.86	14.41	4.61
Ar/CO_2 (Torr)	4.87	13.91	10.94	4.003
Temperature(° C)	300	753.3	569.41	139.64
H_2O (ppm)	2.09	135	32.89	40.15

The SVM model is determined by adjusting the Radial Basis Function (RBF) kernel variance, σ, to maximize accuracy and reduce model complexity. The iterative process to determine σ is shown in Fig. 4.1a where $\sigma = 3.98$ is the selected value for the RBF kernel variance, resulting in an accuracy of 95.04%. The Area Under Receiver Operating Characteristic Curve (AUC) is used to help determine σ, where a larger AUC indicates better performance.

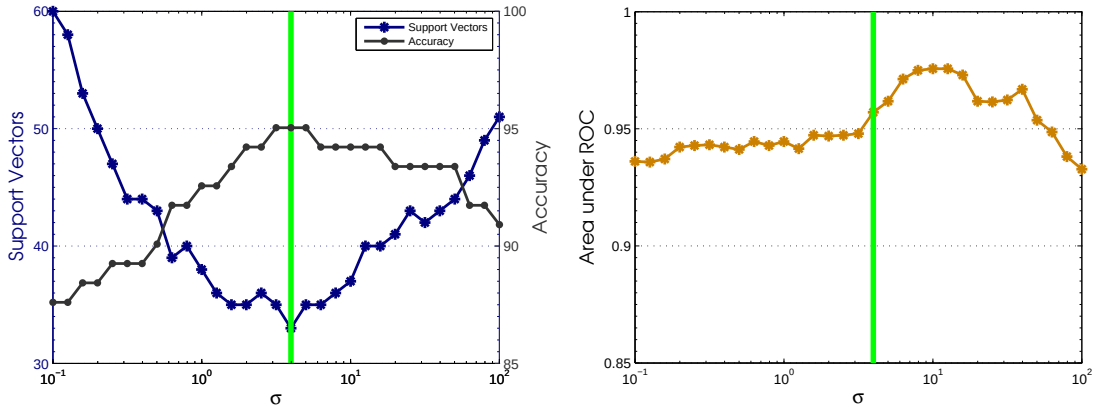

(a) (b)

Figure 4.1: (a) The RBF kernel variance, σ, is varied from 0.1 to 100 and the model accuracy and number of support vectors are plotted. The solid green line indicates the σ value selected for the SVM classifier. (b) The AUC for σ values between 0.1 and 100 is plotted showing the selected σ value, vertical green line, which is not a maximum AUC value but a maximum accuracy and minimum support vector value.

Using the variance determined in Fig. 4.1 the SVM classifier is tested using all combinations of the parameter space consisting of 531,201,645 unique experimental configurations. The distance of the experiment values from the SVM classifier decision boundary determines the probability of SWNT or MWNT growth. Experiments with greater than 90% probability of SWNT growth are saved for further analysis. Histograms of this subset of experiments are plotted to determine trends in each growth parameter. The resulting histograms of each feature plotted against all other features is shown in Appendix A. The histograms shown in Appendix A, depict a larger variance in hydrogen than all other feedstock gases. This can be accounted for due to the greater variation in hydrogen than the other feedstock gases, and most likely not a result of CNT growth dependence on hydrogen.

The temperature value where the highest probability of SWNT growth occurs is determined based on a constant ethylene, hydrogen, argon/carbon dioxide partial pressures and water concentration. The ethylene and hydrogen partial pressures are

increased and the temperature with the highest probability is re-acquired. Repeating this process for all values of hydrogen and ethylene results in the surface plot shown in Fig. 4.2b. The same surface plot is projected onto contours while showing the respective probability contours of SWNT growth for each optimal temperature value in Fig. 4.2a. The temperature is expected to increase as more ethylene is introduced according to the model shown in Fig. 3.14 [56]. This relationship is observed for low ethylene and hydrogen partial pressures where the model confidence is high as shown in Fig. 4.2a. As the model confidence declines, indicated by the lines with blue numbers, this relationship is no longer prevalent because the temperature begins to decrease at higher ethylene partial pressures. A large increase in the optimal growth temperature is predicted for a hydrogen partial pressure of 15 Torr. This is a result of a bias in the training data because several growth experiments were performed at 40 Torr with a higher corresponding hydrogen partial pressure.

An increase in argon/carbon dioxide partial pressure also results in an increase in growth temperature as shown in Fig. 4.3 where hydrogen is held constant at 2 Torr and the water concentration is 10 ppm. An increase in ethylene is expected to result in an increased growth temperature because of additional carbon activity. Carbon dioxide is a weak oxidant that has been shown to improve CNT growth by reducing amorphous carbon deposition and introducing a small amount of water to the growth reaction [22]. Increasing carbon dioxide does not introduce more carbon atoms for nucleating a CNT but it does improve the probability of carbon atoms precipitating into a CNT from the ethylene flow [22].

When ethylene and water concentration are varied, two cases are observed for probability of growth that is greater than 90%, as shown in Fig. 4.4a. One case is where water concentrations are greater than 60 ppm, an increase in ethylene has a direct effect on the optimal growth temperature. Increases in water concentration above 60 ppm have little

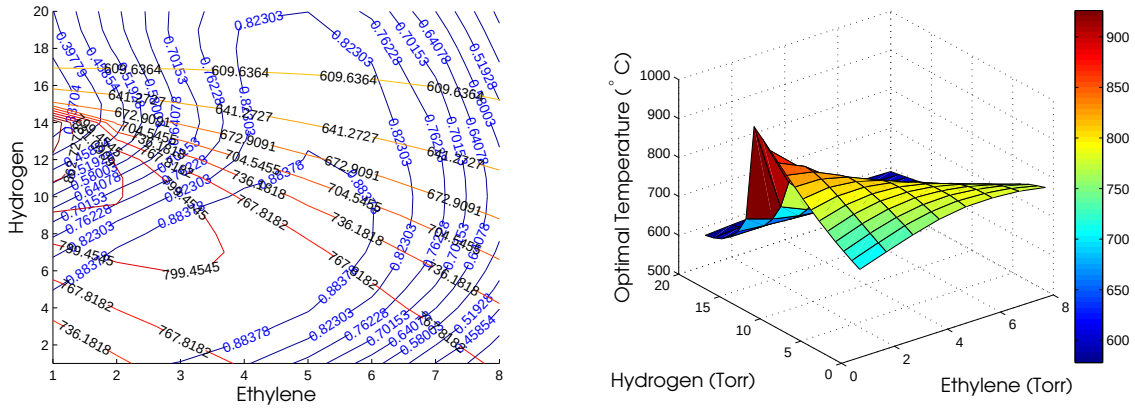

(a) (b)

Figure 4.2: (a) Hydrogen and ethylene are adjusted across their entire range while keeping argon/carbon dioxide = 5 Torr and water concentration = 10 ppm . Each parameter combination is input to the SVM model with growth temperatures ranging from 500° C to 900° C. The growth temperature with the highest probability of SWNT growth is plotted, black numbers, for each hydrogen and ethylene combination. The probability of SWNT growth at each ethylene, hydrogen and temperature point is also shown by the blue numbers. (b) The growth temperatures with the highest probability of SWNT growth for varying ethylene and hydrogen partial pressures are depicted as a surface plot.

effect on the optimal growth temperature, suggesting the growth mechanisms are dominated by ethylene in this regime. The other case is when water concentrations are below 60 ppm. For this case, an increase in either water concentration or ethylene partial pressure results in changes to the optimal growth temperatures indicating more of a dependence on each parameter.

4.1.2 SWNT, SWNT and MWNT vs MWNT Classifier.

The SVM classifier classes can be modeled to determine SWNT growth as an independent event. The two class problem is constructed as any class that includes SWNT growth versus only MWNT growth. Defining the problem in this manner allows more samples to be used for training which reshapes the SWNT class to cover a wider range of growth parameter values. The no growth class is not considered because the no growth

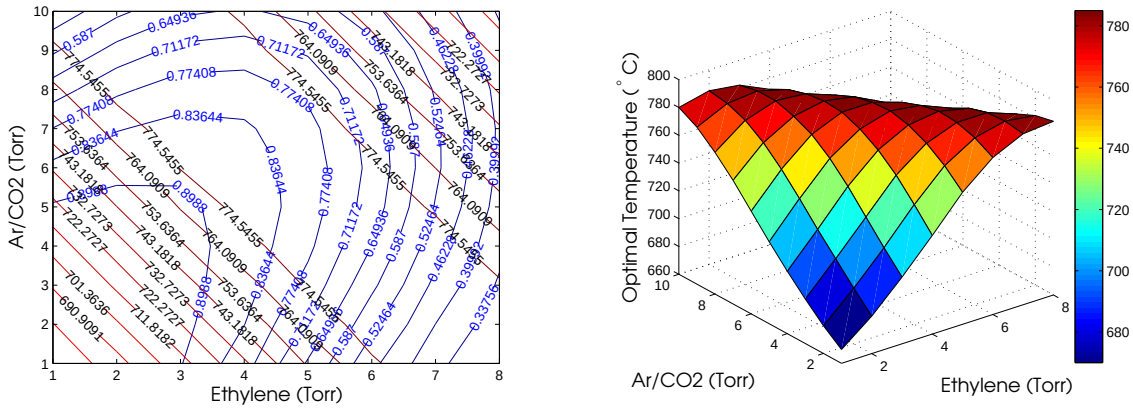

(a) (b)

Figure 4.3: (a) Ethylene and argon/carbon dioxide are varied and the growth temperature with the highest probability of SWNT growth is overlaid on the maximum probabilities of growth for hydrogen = 2 Torr and water concentration = 10 ppm. (b) The optimal growth temperatures are shown as a surface plot to visualize the relationship between ethylene, argon/carbon dioxide and temperature.

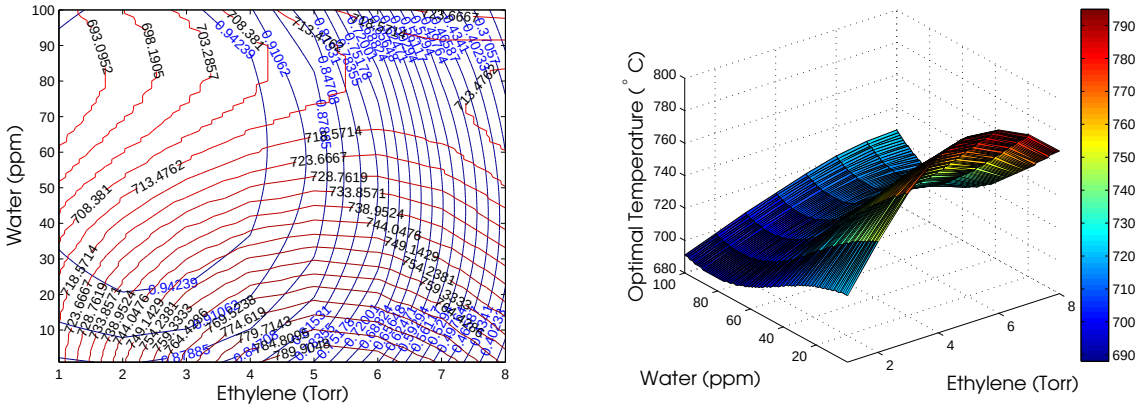

(a) (b)

Figure 4.4: (a) The growth temperature with the highest probability of SWNT growth is overlaid on the corresponding maximum probabilities for argon/carbon dioxide = 5 Torr and hydrogen = 2 Torr. (b) The optimal growth temperatures are also shown as a surface plot.

experiments were experiments that failed for unknown reasons instead of parameter values where CNT growth is not expected to occur. The training data statistics for this new two class problem are shown in Table 4.3 and 4.4 which vary slightly from Table 4.1 and 4.2 due to the additional training data. The training data consists of 34 MWNT growth experiments, 87 SWNT growth experiments and 49 SWNT and MWNT growth experiments.

Table 4.3: The training data statistics for the SWNT, SWNT and MWNT class for the SWNT, SWNT and MWNT vs MWNT classifier. The statistics depicted are from performed growth experiments resulting in either SWNT growth or a combination of SWNT and MWNT growth.

	Min	Max	Mean	Std. Deviation
Ethylene (Torr)	1.008	8.13	4.27	1.81
Hydrogen (Torr)	2.37	18.86	11.05	4.89
Ar/CO2 (Torr)	1.61	13.008	6.84	2.91
Temperature (°C)	400	872.74	656.77	104.97
Water (ppm)	2.09	130	24.96	31.27

Table 4.4: The training data statistics for the MWNT class in SWNT, SWNT and MWNT vs MWNT classifier. The temperature range has shifted to lower temperatures in comparison with the SWNT/MWNT statistics depicted in Table 4.3.

	Min	Max	Mean	Std. Deviation
Ethylene (Torr)	3.04	8.69	6.37	2.59
Hydrogen (Torr)	7.07	18.86	13.80	4.6
Ar/CO2 (Torr)	4.87	13.91	10.19	4.15
Temperature (°C)	300	772.08	573.74	141.01
Water (ppm)	2.09	160	35.27	44.29

The gaussian variance, σ, is varied from 0.1-100 to determine the optimal SVM model parameter. Using σ = 2.512 results in a classifier accuracy of 88.24% for 60 support vectors, as shown in Fig. 4.5a. This accuracy is lower than the SWNT vs MWNT classifier due to the additional MWNT growth samples. A σ value of 6.13 results in a

higher accuracy with more support vectors, however, from the AUC plot shown in Fig. 4.5b, this value would indicate poor performance. The SVM classifier is tested for all parameter combinations to determine regions of SWNT regions with greater than a 90% probability. The result of this parameter space search is shown in Appendix A.

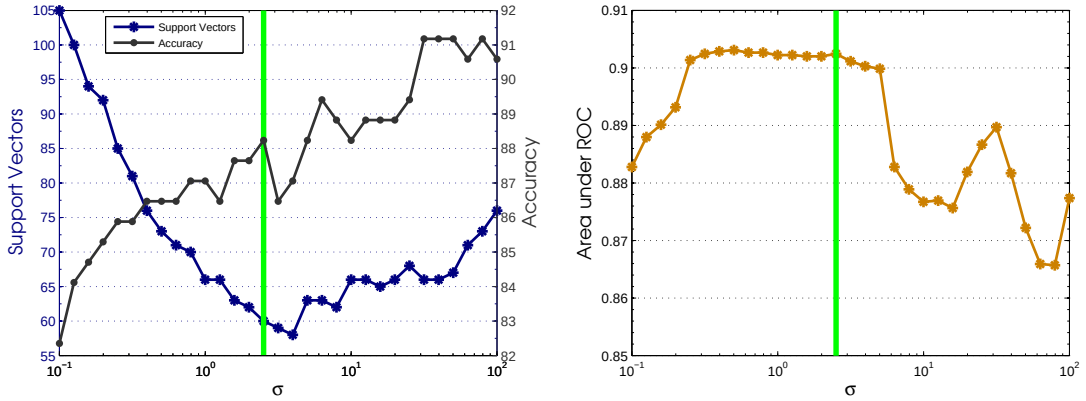

(a) (b)

Figure 4.5: (a) Varying σ from 0.1 to 100 for the SWNT, SWNT and MWNT vs. MWNT classifier. The vertical green line is the σ value selected for creating the SVM classifier. (b) The AUC plot shows the same σ value selected corresponding to a high AUC. Larger σ values have higher classifier accuracies but significant reductions in AUC.

Varying ethylene and hydrogen partial pressures and evaluating the temperature with the maximum probability of SWNT growth, results in the plots shown in Fig. 4.6. A trend toward higher temperatures for higher ethylene partial pressures is determined, peaking at a temperature of 760°C. The increase in temperature from ethylene of 1 to 4 Torr and hydrogen of 1 to 8 Torr is similar to the corresponding region in Fig. 4.2a, suggesting optimal SWNT growth temperatures for these growth parameters to be in the range of 730 - 800°C . The inclusion of MWNT growth in the SWNT class shifts the highest confidence region away from low ethylene and low hydrogen partial pressures. The highest confidence region in Fig. 4.6a shows a decrease in growth temperature as ethylene is increased, contrary to the SWNT vs MWNT classifier. This decrease is greater

along the hydrogen axis implying hydrogen has a large effect on optimal growth temperatures.

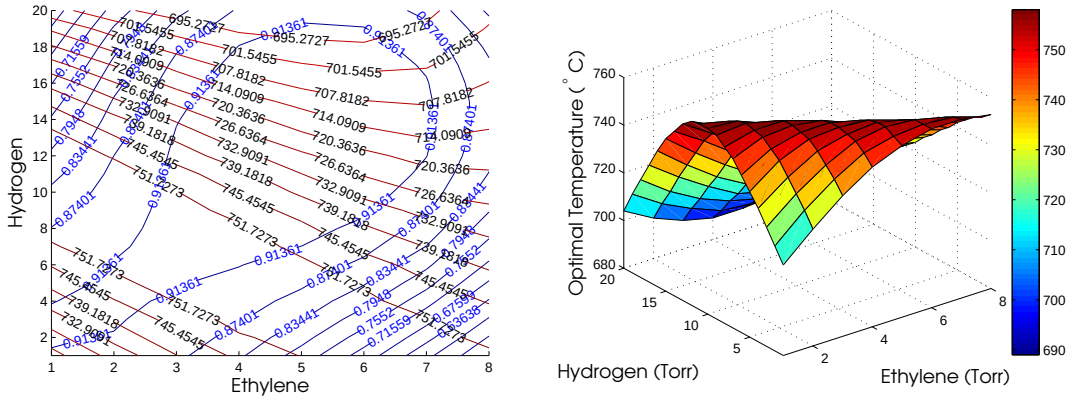

(a) (b)

Figure 4.6: (a) Varying ethylene and hydrogen partial pressures while keeping water concentration = 10 ppm, and argon/carbon dioxide = 5 Torr, the growth temperature is varied to determine the temperature with the highest probability of SWNT growth. The contours labeled with black numbers are the probability contours and the contours labeled with red numbers are the temperature contours. (b) The growth temperatures with the highest probability of SWNT growth are depicted as a surface plot without the probability contour.

Adjustment of ethylene and argon/carbon dioxide partial pressures shows an increased optimal growth temperature for both feedstock gases displayed in Fig. 4.7b. The justification is the same as that of the SWNT vs MWNT classifier, where CO_2 acts as a weak oxidant. The inclusion of MWNT growth in the SWNT class reduces the model confidence as seen by comparing the probability contour in Fig. 4.3a to the probability contour in Fig. 4.7a. The argon/carbon dioxide is 99% argon which is used as a carrier gas for the ethylene molecules. The linear increase in growth temperature is based on additional carbon atoms reaching the catalyst by the additional argon flow into the growth chamber. The effects of CO_2 are not well represented by the model, however the 1% flow of CO_2 is less than 0.1% of all molecules in the growth chamber.

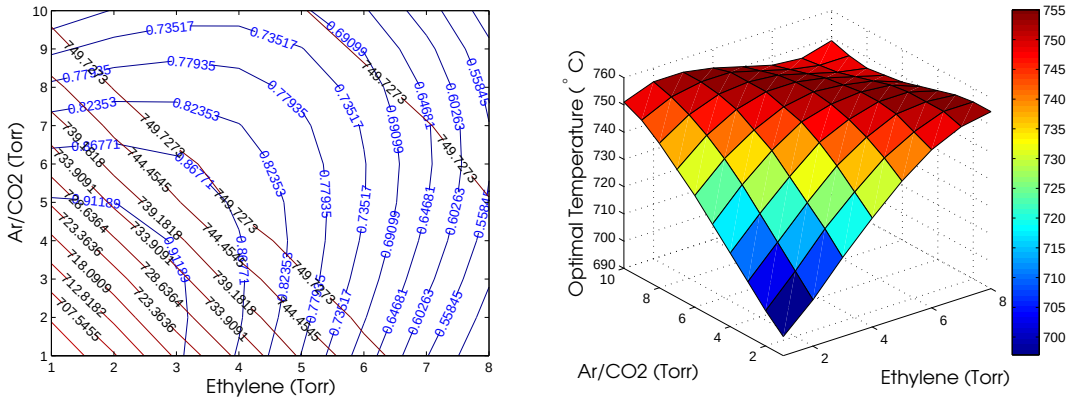

(a) (b)

Figure 4.7: (a) Ethylene and argon/carbon dioxide partial pressures are varied and the growth temperature with the highest probability of SWNT growth is plotted for water concentration = 10 ppm and hydrogen = 2 Torr. (b) The optimal growth temperatures are depicted as a surface plot to visualize the temperature peak predicted by the model as ethylene and argon/carbon dioxide are increased.

Adjustment of water and ethylene for this classifier results in the optimal growth temperature surface plot and probability contour plots shown in Fig. 4.8. Increasing ethylene partial pressure from 1 to 4 Torr results in small temperature increases within the 93.717% confidence region. The temperature surface plot in Fig. 4.8b has a similar shape to the temperature surface plot in Fig. 4.4b for the SWNT vs MWNT classifier, however, the temperatures are slightly higher and two different growth regions are not observed within the highest confidence bound.

4.2 ANN Regression

The training data consists of 219 SWNT growth experiments, however many of these experiments had poor growth kinetic data, creating large uncertainties in the growth rate curves. A total of 66 growth experiments have acceptable growth kinetic data with reliable growth rates. Of these 66 experiments, 56 are used to train the ANN and 10 experiments are selected randomly to validate the regression model.

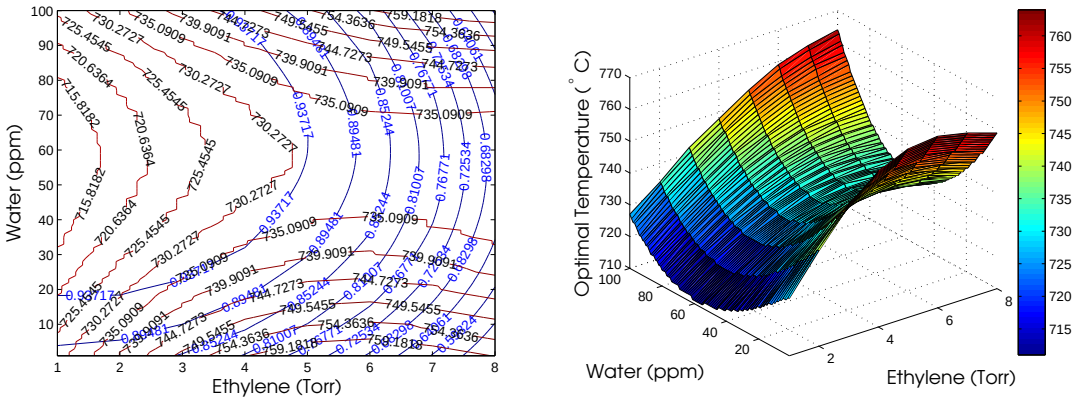

(a) (b)

Figure 4.8: (a) Varying ethylene and water concentration and tracking the temperature with the highest probability of SWNT growth for argon/carbon dioxide = 5 Torr, hydrogen = 2 Torr. The probability of SWNT growth is depicted by the contours with blue labels and the temperature contours are depicted with black labels. (b) A surface plot of the optimal growth temperatures is plotted to visualize the temperature peak determined at low water concentrations.

Two ANN models are constructed using the inputs: ethylene, hydrogen, argon/carbon dioxide, temperature and water concentration. The first model has growth rate as an output and the second model uses the growth length as an output because during experimentation this value was more stable than growth rate for repeated experiments. The growth rate is multiplied by a time constant to create the maximum theoretical CNT length [41]. The maximum theoretical length is not directly related to chiral angle, however, the growth length regression model can be compared to other growth models which are used to determine optimal regions for increasing the catalyst lifetime and/or growth rate.

4.2.1 Growth Rate Regression.

The growth rate regression model allows a growth rate to be specified and returns the experimentation configuration inputs with a high probability of SWNT growth. The training data consists of SWNT growth experiments with measurable growth rates and catalyst lifetimes. Figure 4.9a shows the distribution of growth rates and Fig. 4.9b depicts

catalyst lifetimes within the training data. Very few growth rates are observed above 1000 G peak counts, however, larger growth rates are desired for optimized growth placing an emphasis on large growth rates.

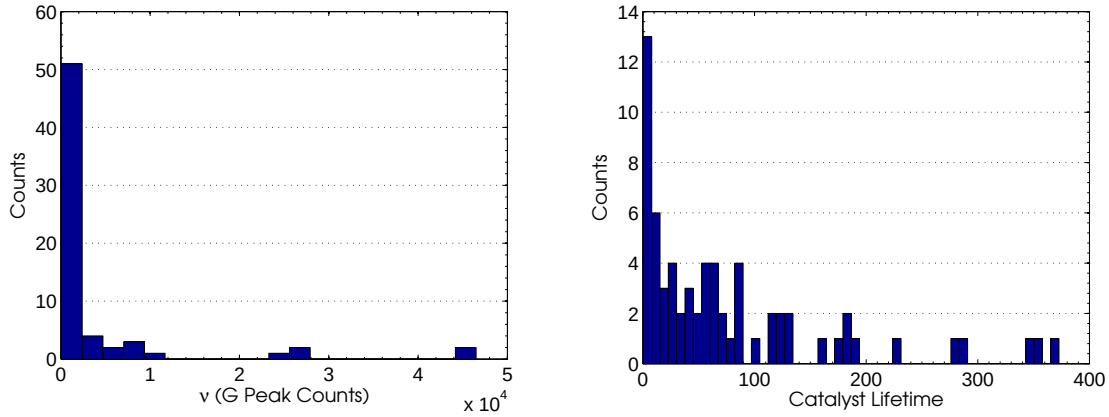

(a) (b)

Figure 4.9: (a) The growth rates used in the ANN training data. Most of the growth rates are below 1000 G peak counts providing few examples of large growth rate experiment conditions. (b) The catalyst lifetimes used in the ANN training data are plotted to show the variance of this parameter in comparison to growth rate.

The training data contains 37 experiments with the same values for ethylene, hydrogen and argon/carbon dioxide partial pressures. This is represented by the large peaks in the histograms in each gas in Fig. 4.10. More growth experiments are needed to fully determine the relationship between each gas partial pressure and SWNT growth rate, however, this biased sampling is valid training for predicting SWNT growth rates. Model predictions using the gas partial pressures in these 37 experiments will be very accurate because of the additional training data for this growth configuration.

The temperature values in the training data are shown in Fig. 4.11a where no large biases are observed in growth temperature values. The growth chamber conditions and pillar defects fluctuate the growth temperature. The water concentration values shown in Fig. 4.11b represent the indication from the dew point sensor, and does not take into

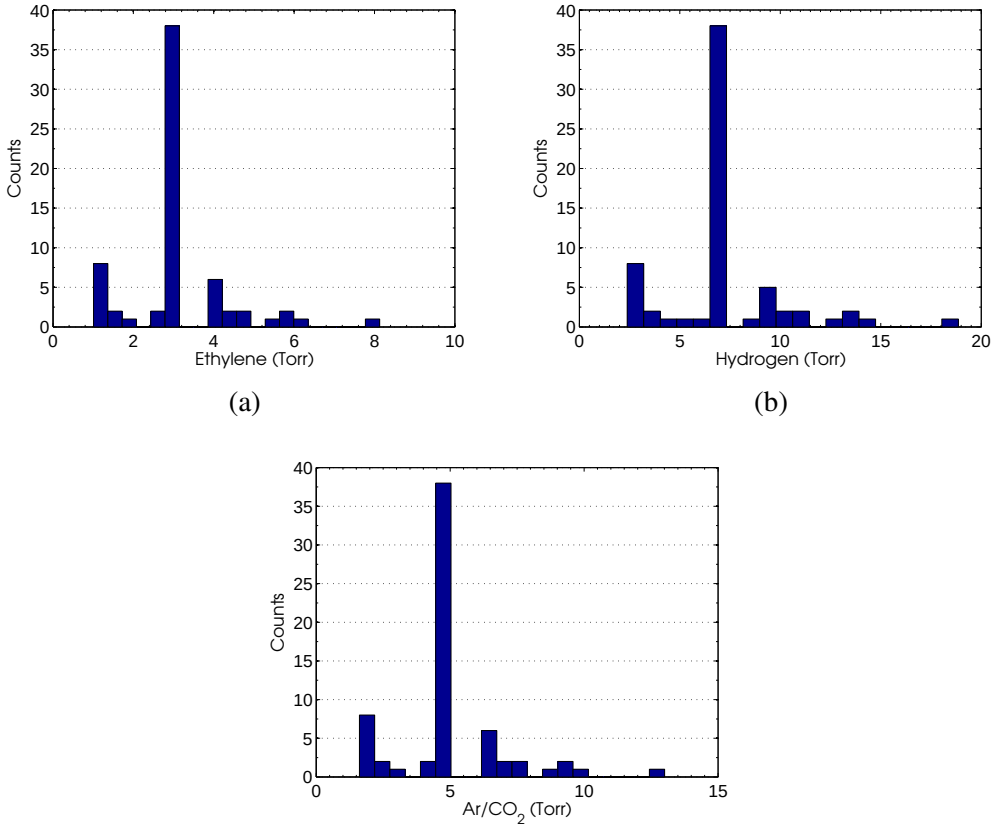

Figure 4.10: (a) Ethylene values in the training data. (b) Hydrogen values in the training data. (c) Argon/carbon dioxide values in the training data. 37 experiments were performed at ethylene = 3.04 Torr, hydrogen = 7.07 Torr, and argon/carbon dioxide = 4.87 Torr making this parameters reliable for testing the regression model after training because of the large number of training examples.

account the additional water vapor that may be present from the chemical reaction of CO_2 and H_2 to form H_2O. Most water concentration values are below 40 ppm, however, growth was observed at water concentrations greater than 100 ppm. The water concentration training data values are missing experiments between 60 ppm and 100 ppm forcing the model to make large interpolations in this range.

As mentioned in Chapter 3, the growth rate and the catalyst lifetime must maintain an inverse relationship. The training data displays this relationship, where the

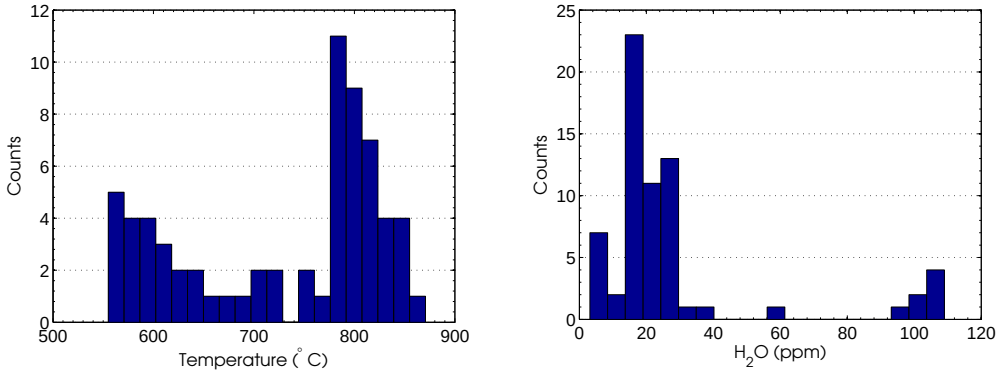

(a) (b)

Figure 4.11: (a) The temperature values used in the ANN training data. A higher temperature is observed for SWNT growth compared to other models because ethylene is used instead of acetylene as a carbon feedstock gas [5]. (b) The water concentration values used in the ANN training data. The water concentration is difficult to precisely control which results in water concentrations > 100 ppm.

Fig. 4.12a is all collected SWNT growth experiments with measurable growth kinetics and Fig. 4.12b contains the data points used for ANN training. The points in Fig. 4.12a with large catalyst lifetimes and are far from the plotted fit line do not display the same inverse relationship represented by rest of the training data. These points are excluded from the training data based on this difference.

An example of the collected SWNT spectra is shown in Fig. 4.13a and the growth rate fit is shown in Fig. 4.13b. A G+ peak is observed at 1580 cm^{-1} and a G- peak, 1550 cm^{-1}, is observed in Fig. 4.13a which is representative of SWNT growth. The D peak is very small, further suggesting SWNT growth, however, the Radial Breathing Mode (RBM) spectra also needs to be analyzed to confirm SWNT growth. The exponential growth equation fits well to the integrated G peak intensities resulting a catalyst lifetime, $\tau = 28$, and the growth rate, $\nu = 1196$.

A neural network, consisting of one hidden layer with 10 neurons, is trained utilizing a 4 fold cross validation, resulting in the Mean Squared Error (MSE) curves

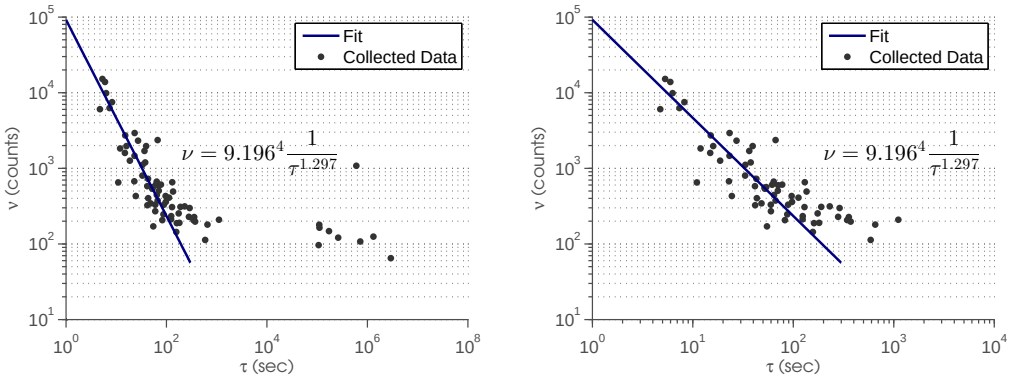

(a) (b)

Figure 4.12: (a) Growth rate and catalyst lifetime plotted showing the inverse relationship between the parameters and validating the collected training data. Nine of the original experiments did not fit the inverse equation and were eliminated from the training data. (b) The training data after eliminating points that did not fit the inverse fit.

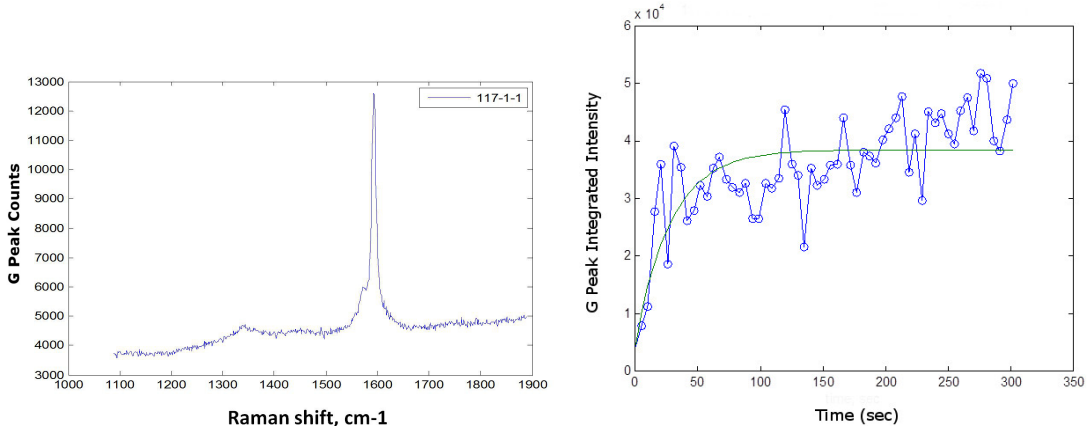

(a) (b)

Figure 4.13: (a) Collected Raman spectra of SWNT. This is SWNT growth because the presence of a sharp G peak at 1580 cm^{-1} and a very small D peak at 1340 cm^{-1}. (b) Integrated G peak intensity with the exponential growth rate equation fit to the data. The calculated growth rate, $\nu = 1196$ and the catalyst lifetime, $\tau = 28$.

shown in Fig. 4.14. Shown in Fig. 4.14, epoch 65 is the last iteration with a decreasing testing and validation error. After epoch 65 the testing and validation error increase

indicating the network at epoch 65 is the most generalized model with minimal regression error. The ANN weights are depicted in Appendix E, where the line thickness depicts the weight magnitude, and where the red lines are negative weights and the black lines are positive weights.

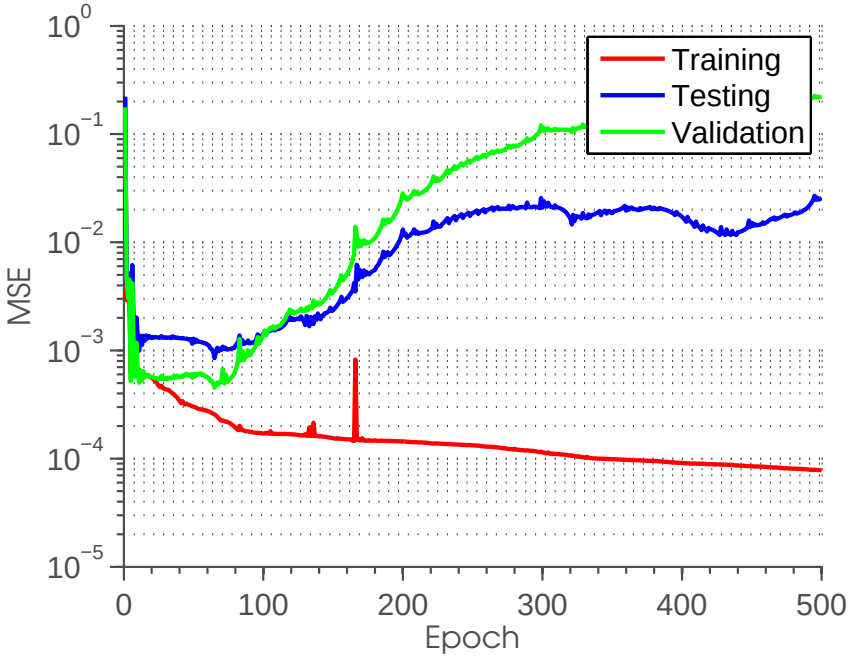

Figure 4.14: Results of training neural network with 1 hidden layer of 10 neurons. Epoch 65 is the last iteration where the training and validation error are decreasing. The neural network at epoch 65 is considered the best model.

The trained ANN regression model is evaluated to determine experimental configurations for desired growth rates, where the inputs are experimental parameters and the output is the expected/modeled growth rates. From this model a lookup table is constructed correlating experimental parameters to growth rates. The lookup table is created by varying ethylene, hydrogen, argon/carbon dioxide, temperature and water concentration across the total parameter space and querying the regression model at each point. This approach creates a large database of mappings from input parameters to growth

rates limiting the ability to predict exact growth rates and instead returns experimental parameters for growth rates within ±1 G peak counts of the requested growth rate.

The lookup table is searched for the maximum growth rate for SWNT probabilities of 99% or greater based on the SWNT vs MWNT classifier and 98.5% or greater based on the SWNT/MWNT vs MWNT classifier. The SWNT growth confidence is lower using the SWNT/MWNT vs MWNT classifier because the SWNT class includes partial MWNT growth. The maximum growth rate experimental values, shown in Table 4.5, are input to the regression model for a range of growth temperatures resulting in the predicted growth rates shown in Fig. 4.15. The growth rate curves have a similar shape because of the similarity between the optimal growth parameters. Performing experiments at higher temperatures, for the parameter values shown in Table 4.5, will validate the ability of the ANN to extrapolate larger growth rates and highlight areas in the regression model with large errors.

Table 4.5: Maximum growth rate experiments with highest probability of SWNT for each SVM classifier model.

Classifier Type	P(SWNT)	C_2H_4 (Torr)	H_2 (Torr)	Ar/CO_2 (Torr)	H_2O (ppm)	Temperature (°C)	Growth Rate (G Peak Counts)
SWNT vs MWNT	99%	2	5	4	76	725	2577
SW/MW vs MWNT	98.5%	2	3	3	76	750	17672

Larger growth rates are desirable for efficient CNT growth, however, growth termination occurs through a variety of methods. These methods include formation of amorphous carbon on the catalyst nanoparticle, coalescence of catalyst nanoparticles, evolution of catalyst morphology during growth, catalyst subsurface diffusion into the catalyst support and porosity of the support among others [6, 28, 29]. The addition of water limits the formation of amorphous carbon and allows for longer catalyst lifetimes and larger growth rates. Also, the addition of water limits Ostwald ripening and increases catalyst activity [7]. The training data contains 37 experiments with ethylene at 3.04 Torr,

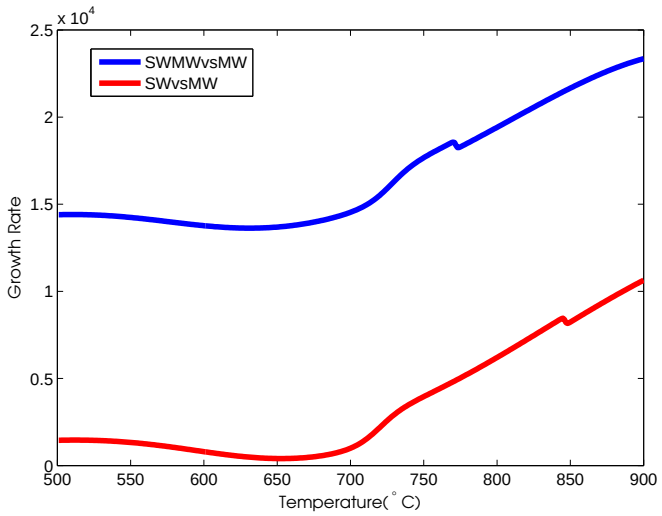

Figure 4.15: ANN predicted growth rates for varying temperatures including the maximum growth rate for: 99% probability of SWNT growth for the SWNT vs MWNT classifier and 98.5% probability of SWNT growth for the SWNT/MWNT vs MWNT classifier.

hydrogen of 7.07 Torr and argon/carbon dioxide equal to 4.87 Torr. Keeping these values constant allows only two degrees of freedom in water concentration and growth temperature. The growth rate model predicts an increase in water concentration for higher growth rates using the constant values discussed for ethylene, hydrogen and argon/carbon dioxide. Excess water will poison the growth process which the model also predicts by a peak in water concentration as shown in Fig. 4.16. The water concentration values shown in Fig. 4.16 are beyond the range of the training data. This is an extrapolation of the model that requires validation through additional experimentation.

The model predictions for the validation data are shown in Table 4.6. The growth rates fluctuate across wide ranges with small changes in growth parameters. Setting ethylene, hydrogen and argon/carbon dioxide to 3.04 Torr, 7.07 Torr and 4.87 Torr, respectively, and making small adjustments in both water concentration and temperature, results in growth rates between 116 to 6049 G peak counts. The model performs well on

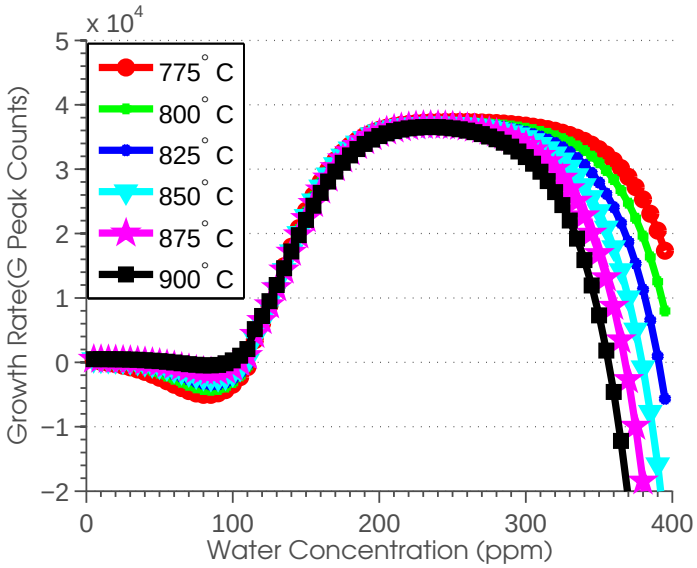

Figure 4.16: Keeping ethylene, hydrogen and argon/carbon dioxide constant and varying water concentration for 5 different growth temperatures results in an increase and decrease in growth rates.

the second sample in Table 4.6 because there are more training data points between 800 to 900°C and 20 to 30 ppm making this sample well represented in the training data.

Table 4.6: The predicted values for performed experiments that were not included in the training data. The growth rate regression model performs well on the second sample because the growth parameters are well represented in the training data. Large errors are observed on other samples because of limited training data for these growth parameters.

C_2H_4 (Torr)	H_2 (Torr)	Ar/CO_2 (Torr)	H_2O (ppm)	Temperature (°C)	Predicted Growth Rate (G Peak Counts)	Observed Growth Rate (G Peak Counts)
5.08	11.78	8.13	20.5	550	22538	4237.9
3.04	7.07	4.87	26.1	872.74	323	140.41
4.03	9.52	6.45	7	741.75	2208	263.9
1.008	2.37	1.61	3.22	642.54	3109	247.64
8.13	18.86	13.008	26.5	658.6	46783	175.28
3.04	7.07	4.87	90	630	-5671	6049.5
3.04	7.07	4.87	2.1	711.19	1829	284.07
2.23	5.18	3.57	110	630	19431	3678.8
3.04	7.07	4.87	25.1	770.67	-583	116.72

In addition to the validation data shown in Table 4.6, the growth rate was linearly increased the experiment parameters with the highest probability of SWNT growth were returned from the ANN model. The results are shown in Table 4.7 highlighting the complex relationships between the input parameters.

Table 4.7: Linearly Increasing Growth Rate Experiments

C_2H_4 (Torr)	H_2 (Torr)	Ar/CO_2 (Torr)	H_2O (ppm)	Temperature (° C)	Growth Rate (G Peak Counts)	SWNT Probability
3	5	4	56	825	100	97.95%
2	7	3	80	675	200	98.49%
2	6	4	83	675	300	98.90%
3	5	4	87	750	400	98.71%
2	5	4	62	750	500	98.80%
3	3	3	67	675	600	98.20%
2	5	5	49	825	700	97.29%
3	7	3	95	725	800	97.98%
3	6	3	78	800	900	97.84%
3	4	4	79	750	1000	98.68%

Additional experimentation was performed after training the ANN regression model. These new experiments no longer include argon/carbon dioxide and increase the water concentration outside the range of the training data. The predicted results are shown in Table 4.8, where most predictions are extrapolations of the model. The training data has a maximum water concentration of 110 ppm, far below many of the growth experimental values. The first two entries in Table 4.8 have similar predicted and observed growth rates displaying the limited ability of the model to extrapolate.

4.2.2 Theoretical Length Regression.

Each growth experiment includes the catalyst lifetime and growth rate, and multiplying these two terms results in a maximum CNT projected length. The theoretical length is more stable than growth rate or catalyst lifetime when the same parameters are used in repeated experiments. The theoretical length cannot be used to control chirality,

Table 4.8: Additional experimentation was performed with parameters outside the range of the training data. The model predicts closely to the observed growth rate for the first sample, however, all experiments are extrapolations.

C_2H_4 (Torr)	H_2 (Torr)	Ar/CO_2 (Torr)	H_2O (ppm)	Temperature (°C)	Predicted Growth Rate (G Peak Counts)	Observed Growth Rate (G Peak Counts)
10.67	5.33	0	184	920	2780	2224.1
10.67	5.33	0	184	887	2738	1109.8
10.67	5.33	0	186	849	3238	726.34
10.67	5.33	0	188	928	4420	1596
10.67	5.33	0	189	784	3239	143
8	8	0	148	878	-1310	112
8	8	0	147	808	-825	649
13.5	13.5	0	170	788	-5225	96.55
13	13	0	80	880	976	1966
11.6	17.4	0	60	771	1881	194

however, a regression model is still useful for extracting relationships between growth parameters and CNT length.

The same samples used for training the growth rate regression model is used for training the theoretical length model. Figure 4.17 displays the training sample distribution with no units included for the theoretical length axis because the growth rate is in G peak counts instead of μm/s. Further analysis is needed to determine the relationship between G peak counts, CNT length and CNT growth rate.

The trained growth length ANN contains 5 input neurons, 1 hidden layer of 10 neurons and 1 output neuron. The training results are shown in Fig. 4.18 where the model weights at epoch 56 are used for the final regression model because of the increasing testing and validation errors after this iteration. The ANN weights are shown in Appendix E for this model.

The length regression model predictions for the validation data is shown in Table 4.9. The model is very accurate for nearly all of the validation data points which is also represented by the drop in the validation error in Fig. 4.18. This improved prediction ability using the growth length instead of growth rate confirms the increased stability of growth length.

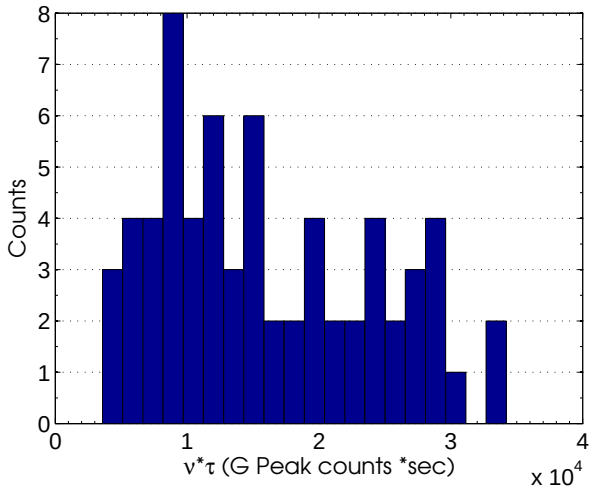

Figure 4.17: The training data used for the theoretical length regression model. The theoretical length axis does not contain units because the growth rate is in G peak counts instead of μm/s.

Table 4.9: The predicted values for experiments withheld from the training data. The growth length model performs well across a wider range of growth parameters than the growth rate model. This is due to the increased stability of growth length for repeated experiments, therefore requiring less training data to determine input/output relationships.

C_2H_4 (Torr)	H_2 (Torr)	Ar/CO_2 (Torr)	H_2O (ppm)	Temperature (°C)	Predicted Length (G Peak Counts*sec)	Observed Length (G Peak Counts*sec)
5.08	11.78	8.13	20.5	550	28829	26632
3.04	7.07	4.87	26.1	872.74	17094	13510
4.03	9.52	6.45	7	741.75	7844	6037
1.008	2.37	1.61	3.22	642.54	9151	10285
8.13	18.86	13.008	26.5	658.6	14697	23777
3.04	7.07	4.87	90	630	18292	32066
3.04	7.07	4.87	2.1	711.19	7409	10148
2.23	5.18	3.57	110	630	20325	20515
3.04	7.07	4.87	25.1	770.67	8793	10365

The training data set has 37 experiments with the same ethylene, hydrogen and argon/carbon dioxide partial pressures. The trained regression model is queried using ethylene of 3.04 Torr, hydrogen at 7.07 Torr, argon/carbon dioxide equal to 4.87 Torr, temperature 800 - 900°C and water varied from 1 to 50 ppm to visualize the model predictions and compare against Fig. 3.17. These growth values are used because the

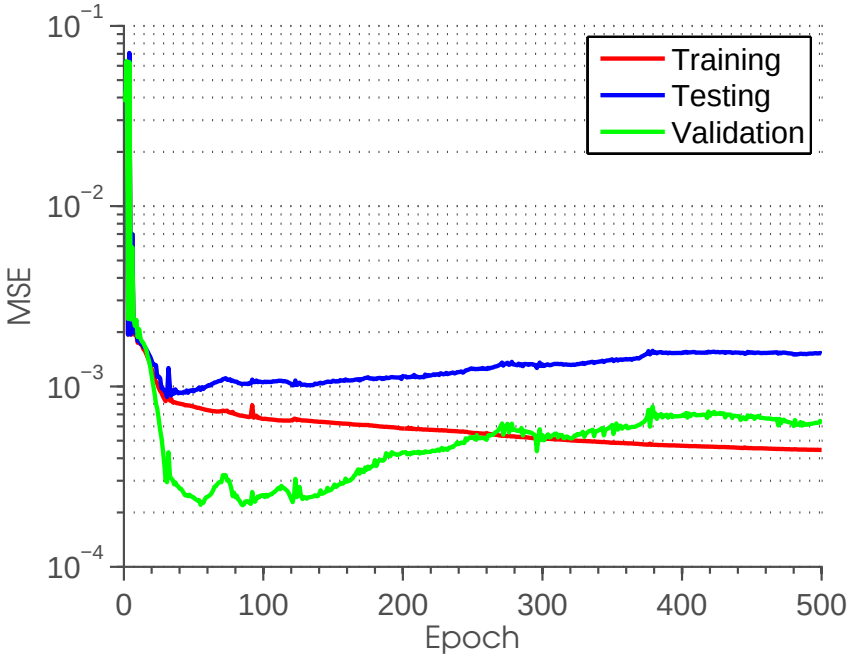

Figure 4.18: Training, testing, and validation curves using 4 fold cross validation. Epoch 56 is the model selected because of the increase in testing and validation errors after this epoch.

training data contains 37 experiments in these parameter ranges making the network predictions more accurate.

The model predictions are shown in Fig. 4.19b where a peak in the growth length is determined at an optimal water/ethylene ratio. The catalyst lifetime is increased with an increase in water because water reduces the amount of amorphous carbon forming on the catalyst nanoparticle and limits the impact of Ostwald ripening on the catalyst particles. Increasing the water concentration beyond the optimal point results in large reductions in growth yields because the growth process is poisoned by excess water. The work of Futaba et al. is also shown in Fig. 4.19a for comparison, however the scales cannot be directly correlated because of different experiment configurations and CNT length measurement techniques. Figure 4.19a is based on ethylene varying between 10 to 300 Standard Cubic Centimeter per Minute (SCCM), water varying from 50 to 290 ppm, a

constant growth temperature of 750°C and an iron catalyst on a 2cm by 2cm growth substrate [15]. The model predictions disagree for low water/ethylene ratio values at high temperatures. As the temperature is reduced the two models begin to agree but this may be a result of using different growth systems and growth length measurement techniques.

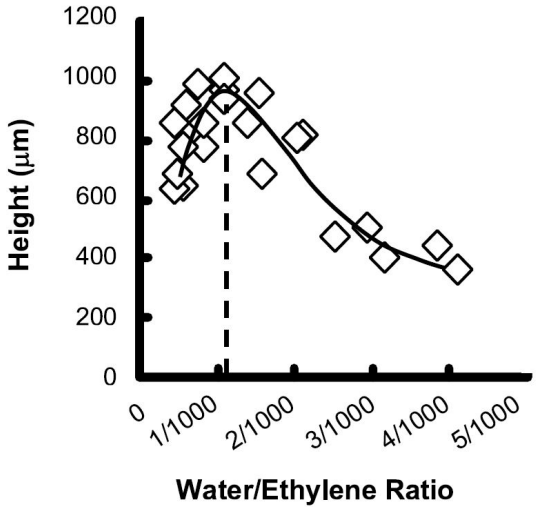

(a)

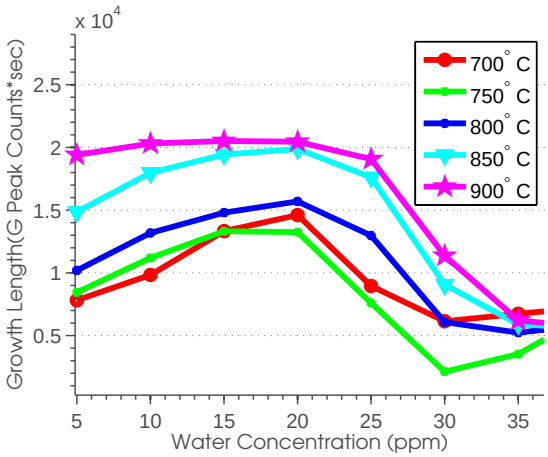

(b)

Figure 4.19: (a) Results of Futaba et al. in modeling CNT carpet height against water concentration/ethylene ratio [15]. ©2005 The American Physical Society (b) ANN results for: Ethylene = 3.04 Torr, hydrogen = 7.07 Torr, argon/carbon dioxide = 4.87 Torr with temperature and water varying results in a similar relationship between water and CNT growth length.

The additional experiments shown in Table 4.8 are also applied to the length regression model for additional extrapolation testing. The length regression model does not extrapolate well based on the large errors between predicted and observed length values in Table 4.10. Figure 4.19b shows that water concentration is an important parameter in controlling the CNT length. Nearly all of the experiments in Table 4.10 are extrapolations of water concentration creating large errors in the model.

This chapter has discussed the results of the SWNT vs MWNT classifier, SWNT/MWNT vs MWNT classifier, ANN growth rate regression and theoretical length

Table 4.10: The predicted growth length values for experiments with growth parameters outside the range of the training data. All experiments are model extrapolations and results in poor performance.

C_2H_4 (Torr)	H_2 (Torr)	Ar/CO_2 (Torr)	H_2O (ppm)	Temperature (°C)	Predicted Length (G Peak Counts*sec)	Observed Length (G Peak Counts*sec)
10.67	5.33	0	184	920	13884	59176
10.67	5.33	0	184	887	13915	36965
10.67	5.33	0	186	849	14117	31217
10.67	5.33	0	188	928	13883	23790
10.67	5.33	0	189	784	16640	22563
8	8	0	148	878	13884	66533
8	8	0	147	808	14077	7128
13.5	13.5	0	170	788	12461	1.03×10^7
13	13	0	80	880	-602	77500
11.6	17.4	0	60	771	4727	13301

regression. The two SVM classifier models produced similar results in optimal growth temperatures and are able to output experiment parameters most likely to grow SWNTs. The growth rate regression model identified experimental parameters maximizing SWNT growth rates. An additional regression model for maximum theoretical length was able to determine a relationship between SWNT length and water/ethylene ratio. Additional experimentation will continue to strengthen these models through iteration of the training process as the validation error increases with new data.

V. Conclusions and Future Work

This chapter summarizes the results of this thesis and presents ideas for future work on this area of research. The two machine learning algorithms applied to this CNT research are discussed in Section 5.1. Ideas for future work and areas of this research requiring additional research are outlined in Section 5.2. Finally, the contributions of this thesis to predictive CNT growth rates and selective SWNT growth are discussed in Section 5.3.

5.1 Summary of Conclusions

The problem statement of this thesis is to predict SWNT growth properties based on the growth parameters prior to experimentation. The result of this thesis is the ability to predict growth properties of CNTs using only the growth parameters prior to experimentation. The growth properties include the number of walls precipitated from the catalyst nanoparticles and the growth rate of SWNTs. The growth parameters considered are: ethylene, hydrogen, argon/carbon dioxide, growth temperature, and water concentration for a constant catalyst composition. The growth process consists of an in-situ laser induced Chemical Vapor Deposition (CVD) growth system. The substrates consist 10 μm diameter pillars of silicon with nickel and alumina ion beam sputtered on top of each pillar.

The ability to predict if a growth experiment will result in SWNT or MWNT growth allows detailed research and analysis of CNT properties and applications. This was accomplished with an SVM classifier utilizing an RBF kernel function for creating a hyperplane that linearly separates the two classes. Two different classifier models are constructed: strictly SWNT growth vs MWNT growth and a combination of SWNT and MWNT growth vs only MWNT growth. The SWNT vs MWNT accuracy is 95.04% while

the second classifer, SWNT/MWNT vs MWNT growth, has a lower accuracy at 88.24%. The probability of SWNT growth is investigated for varying growth parameter values and relationships between argon/carbon dioxide, ethylene, hydrogen and temperature are determined. Increased catalyst activity is shown to increase the required growth temperature predicted by both classifier models.

A regression model for predicting SWNT growth rates is also implemented for chiral selective growth. An ANN is trained using 4 fold cross validation to create a generalized regression model. The ANN regression model creates a lookup table mapping experiment input values to SWNT growth rates. The lookup table provides the maximum growth rate, meeting a 99% probability of SWNT growth based on the SWNT vs MWNT classifier and 98.5% probability of growth, based on the SWNT/MWNT vs MWNT classifier. Growth experiments implementing the model predicted maximum growth rate experiments result in higher SWNT growth rates demonstrating the extrapolation abilities of the model.

A second regression model is also implemented for maximum theoretical length. This model relies on the same experiments for training data as the growth rate regression model. Repeated experiments result is small changes in growth rates and catalyst lifetimes but the maximum theoretical length showed more stability over many experiments. The goal of this regression model is to determine a relationship between growth length and water/ethylene ratio. The predicted growth length as a function of water/ethylene ratio agreed well with the work of Futuba et. al in the shape of these curves.

5.2 Future Work

This section discusses future research related to chiral selective growth of SWNTs.

5.2.1 Experiment Correlation.

It is assumed that experiments performed on adjacent pillars have no effect on the current experiment. The collected data changed growth parameters on each pillar making it difficult to find any correlation between adjacent experiments. Performing the same experiment many times over several patches of pillars will allow a detailed analysis of how growth kinetics change as more experiments are performed. Using the collected training data, no strong correlations were observed across patches, however, this still requires further analysis.

5.2.2 Time Series Growth Rate Prediction.

If a correlation does exists between adjacent pillars or across patches of pillars a different type of growth rate regression is required. The ANN regression model will require information about previous experiments to predict the current experiment output. This approach is referred to as time series regression where events are dependent on past events.

5.2.3 Optimized Catalyst Prediction.

The SVM classifier and growth rate prediction performed in this work is limited to nickel catalysts because the training data only included this material. The inclusion of additional catalyst materials will show differences in optimal SWNT growth parameters and growth rates. The analysis of many catalyst materials will show trends toward catalysts with more desirable growth properties such as lower temperature, feedstock material and minimal amorphous carbon deposition.

5.2.4 Uniform Input Parameter Sampling.

The training data for the SVM classifier and ANN regression model contained large biases in the growth gases. Many experiments were performed with very similar gas partial pressures limiting the ability of the models to find the relationship between each input gas and the corresponding output. A design of experiments to sample the growth

gases will create a more uniform sample and provide better training data. The current models performed poorly on the experiments lacking an argon/carbon dioxide input and high water concentrations. If this configuration is better for controlling growth then the current models will need to be retrained on this additional data.

5.2.5 Analytical Model Comparison.

Work performed by Puretzky et al. shows an analytical model of SWNT growth rates for varying temperatures with acetylene as the feedstock material and iron as the catalyst [5]. The model determines an exact temperature at a specific acetylene partial pressure for SWNT growth. The SVM classifier results can be compared to these analytical predictions if the model is adjusted for ethylene partial pressure and a nickel catalyst. Differences in growth systems may have a large effect on the results and growth dynamics because carpets are grown typically by large scale CVD and only a few CNTs are produced on the laser induced heating system considered in this work.

5.2.6 Neural Network Pruning.

The trained ANN regression models were not modified after training and their weights were not further analyzed. Algorithms such as optimal brain damage pruning allow modifications to be made to the trained network to reduce overfitting and increase generalizability. Although K-fold cross validation was used to reduce overfitting, the structure of the network was predetermined and not adjusted based on any pruning algorithm. Pruning algorithms are difficult to implement because the wrong weights can be removed causing the network results to worsen.

5.3 Contributions

This thesis has shown a way to predict CNT growth experiment outcomes based on the controllable input parameter values. This machine learning approach is a new way to approach complex materials problems and quickly extrapolate limited results. The SVM classification method outputs ranges of input parameter values with the highest

likelihood of SWNT growth allowing further analysis of these regions utilizing the ANN regression model. Prediction of SWNT growth rates was accomplished on growth parameters similar to the training data. A second set of experiments with large variations in growth parameter values from the training data resulted in large prediction errors. The impact of applying machine learning algorithms to CNT growth analysis is a reduction in the number of required experiments to validate observations and increased experiment efficiency. This approach coupled with the highly automated growth system used in this work provides a way to direct autonomous experimentation for creating materials with desired properties.

Appendix A: SWNT vs MWNT Classifier

A.1 SWNT Growth Histograms

Varying the growth parameters across the entire parameter space and recording experiment configurations predicted to grow SWNTs with greater than 90% probability results in the histograms shown below.

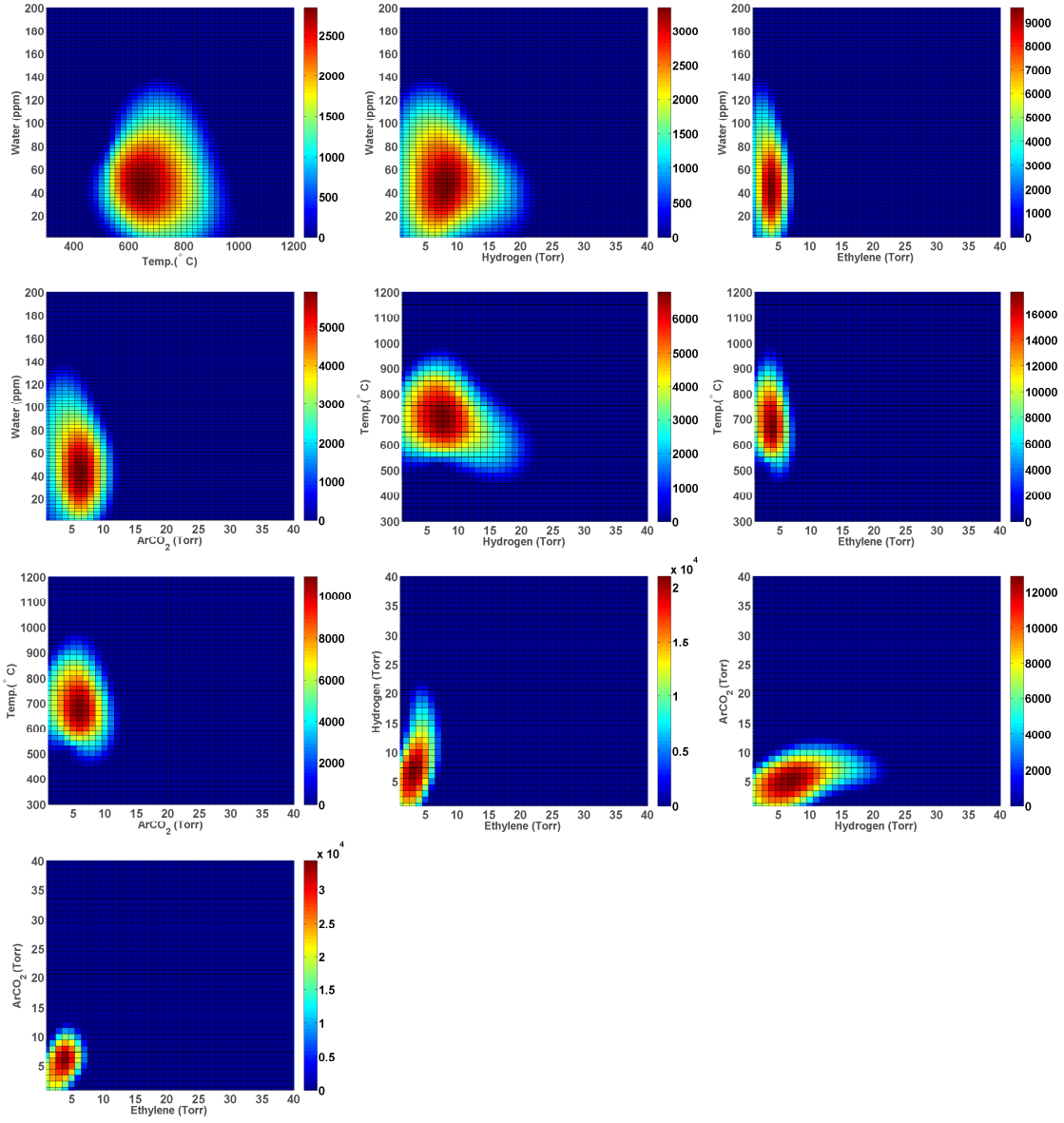

Appendix B: SWNT, SWNT and MWNT vs MWNT Classifier

B.1 SWNT and SWNT/MWNT Growth Histograms

Experiments predicted to grow either strictly SWNTs or a combination of SWNTs and MWNTs with a probability greater than 90% are shown in the histograms below. These cover a wider range than the plots depicted in Appendix A.

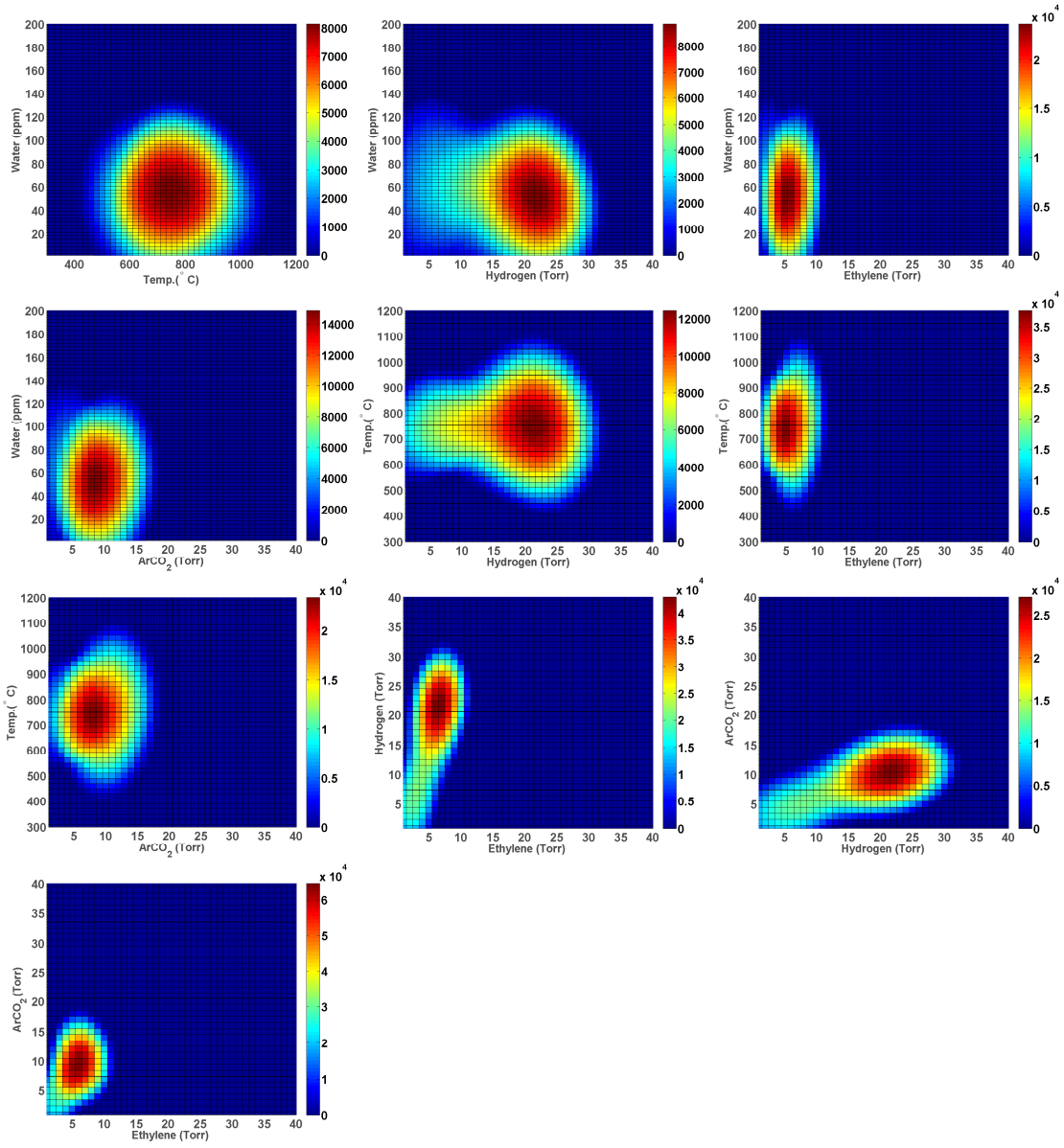

Appendix C: Code Snippets

The SVM classifiers are trained using Weka libraries and leveraging custom written Java code. The data set is created as an Attribute Relationship File Format (ARFF) file for the Weka training methods.

```
        sigma = 3.981;
        C = 1;
        //Train the SVM classifier
        RBFSVM model = new RBFSVM(filename,sigma,C);

        Instances train = new Instances(
                            new BufferedReader(
                                new FileReader(filename)));
        train.setClassIndex(train.numAttributes()-1);

        Classifier SVM = new weka.classifiers.meta.CostSensitiveClassifier();

        StringBuilder builder = new StringBuilder();
        String baseString = "-cost-matrix \"[0.0 1.0; 2.58 0.0]\"-S 1 -W
weka.classifiers.functions.SMO -- -C 1.0 -L 0.001 -P 1.0E-12 -N 0 -M -V
 -1 -W 1 -K \"";
        String optionString = "weka.classifiers.functions.supportVector.RBFKernel
 -C 250007 -G 0.7 ";
        String tempString[] = optionString.split(" ");
        tempString[tempString.length-1]=Double.toString(sigma);

        for (String string:tempString){
            if (builder.length()>0){
                builder.append(" ");
```

```
            }
            builder.append(string);
        }
        optionString=builder.toString();

        optionString = baseString + optionString + "\"";
        String[] options = weka.core.Utils.splitOptions(optionString);
        SVM.setOptions(options);
        //Train Classifier
        SVM.buildClassifier(train);
```

Training the ANN regression models requires implementing the K-Fold cross validation algorithm and multithreading the training process for increased speed. The libraries within Encog are utilized for building, training and testing the ANN. All code is written in C# and SVM calculations are made by calling .jar files to run executable Java code.

```
//Start K threads
    allThreads = new Thread[kFolds];
    threadIDs = new int[kFolds];
    for (int d = 0; d < kFolds; d++)
    {
        int copy = d;
        allThreads[d] = new Thread(() => trainNetwork(trainingSet[copy],
        testingSet[copy], validationSet));
        threadIDs[d] = allThreads[d].ManagedThreadId;
        allThreads[d].Name = copy.ToString();
        allThreads[d].Start();
    }
    parseMatrix = new Thread(parseThreadMatrix);
    parseMatrix.Start();
```

```
public void parseThreadMatrix()
{
int currentEpoch = 1;
int maxEpochCount = 0;
lock (iterationsTxt)//Referencing GUI object, need to lock it
{
maxEpochCount = Convert.ToInt32(iterationsTxt.Text);
}
List<int> epochNum = new List<int>();
List<double> trainMSEList = new List<double>();
List<double> testMSEList = new List<double>();
List<double> valiMSEList = new List<double>();

while (currentEpoch < maxEpochCount+1)
{
//Check if first column is filled, then release memory,
then calculate and plot, increment epoch value
double[] trainEpoch = new double[kFolds];
double[] testEpoch = new double[kFolds];
double[] valiEpoch = new double[kFolds];
double trainMSE = 0;
double testMSE = 0;
double valiMSE = 0;
Boolean trainCollected = false;
Boolean testCollected = false;
Boolean valiCollected = false;

while (trainCollected == false || testCollected == false ||
valiCollected == false)
//Keep waiting for first column to be filled in all three matrices
{
if (trainCollected == false)
```

```
{
    lock (threadTrainingError)
    {
        for (int i = 0; i < kFolds; i++)
        {
            trainEpoch[i] = threadTrainingError[i][currentEpoch-1];
        }
    }
        if (!trainEpoch.Contains(0.0))
        //If all values are filled in training column, checking again
        {
            trainCollected = true;
        }
}
if (testCollected == false && trainCollected == true)
{
    lock (threadTestingError)
    {
        for (int i = 0; i < kFolds; i++)
        {
            testEpoch[i] = threadTestingError[i][currentEpoch-1];
        }
    }
    if (!testEpoch.Contains(0.0))
    {
        testCollected = true;
    }
}
    if (valiCollected == false && testCollected==true &&
    trainCollected ==true)
    {
        lock (threadValidationError)
```

```
        {
            for (int i = 0; i < kFolds; i++)
            {
                valiEpoch[i] = threadValidationError[i][currentEpoch-1];
            }
        }
        if (!valiEpoch.Contains(0))
            valiCollected = true;
    }
   // Thread.Sleep(500);
} //All values should be filled in this column in all matrices

//trainCollected = true;
//Calculate MSE
double sum = 0;
for (int i = 0; i < kFolds; i++)
{
    sum = sum + (trainEpoch[i] * trainEpoch[i]);
}
trainMSE = sum / kFolds;

sum = 0;
for (int i = 0; i < kFolds; i++)
{
    sum = sum + (testEpoch[i] * testEpoch[i]);
}
testMSE = sum / kFolds;

sum = 0;
for (int i = 0; i < kFolds; i++)
{
    sum = sum + (valiEpoch[i] * valiEpoch[i]);
```

```
}
valiMSE = sum / kFolds;
    epochNum.Add(currentEpoch);
    trainMSEList.Add(trainMSE);
    testMSEList.Add(testMSE);
    valiMSEList.Add(valiMSE);
    this.Invoke((MethodInvoker)delegate
    {
        iterationEpochTxt.Text = Convert.ToString(currentEpoch);
        iterationErrorTxt.Text = Convert.ToString(valiMSE);
        if (valiMSE < minError)
        {
            lock (threadNetworks)
            {
                double min = 1000;
                for (int i = 0; i < kFolds; i++)
                //Want to save one of K networks with lowest MSE
                {
                    if (valiEpoch[i] < min)
                    {
                        min = valiEpoch[i];
                        bestNetwork = threadNetworks[i][currentEpoch];
                    }
                }
                minError = valiMSE;
                validationErrorTxt.Text = Convert.ToString(valiMSE);
                epochCount.Text = Convert.ToString(currentEpoch);
            }
        }
    });
currentEpoch++;
}}
```

Calling the executable .jar file is performed by starting a process and giving the executable file command line arguments as shown below.

```
string modelPath = "\"" + svmModel_Txt.Text + "\"";
String inputDataString = "C:\\Users\\SERG_Laptop01\\Documents\\
Visual Studio 2013\\Projects\\ANNSolver\\WekaProjects
\\allTestInstances.txt";

inputDataString = "\"" + inputDataString + "\"";

String fileLocation = "C:/Users/SERG_Laptop01/Documents/
Visual Studio 2013/Projects/ANNSolver/WekaProjects/
BatchJars/getBatchProbabilities.jar";
fileLocation = "\"" + fileLocation + "\"";
Console.WriteLine(" \"C:/Users/SERG_Laptop01/Documents/
Visual Studio 2013/Projects/ANNSolver/QueryNetwork/bin/
Debug/getBatchProbabilities.jar\
" " + modelPath + inputDataString);
Process p = new Process();
ProcessStartInfo ps = new ProcessStartInfo(@"C:\Program Files (x86)
\Java\jre7\bin\java.exe", @"-jar " + " \"C:/Users/SERG_Laptop01/
Documents/Visual Studio 2013/Projects/ANNSolver/QueryNetwork/bin
/Debug/getBatchProbabilities.jar\" " + modelPath + inputDataString);
String execute = @"-jar ";
String[] args = { execute, fileLocation, modelPath, inputDataString };
String fileName = @"C:\Program Files (x86)\Java\jre7\bin\java.exe";
p.StartInfo.FileName = fileName;
p.StartInfo.Arguments = String.Join(" ", args);
p.StartInfo.UseShellExecute = false;
p.StartInfo.RedirectStandardInput = true;
p.StartInfo.RedirectStandardOutput = true;
```

```
p.StartInfo.RedirectStandardError = true;
p.StartInfo.CreateNoWindow = true;
p.Start();
string swProbability = p.StandardOutput.ReadLine();
string error = p.StandardError.ReadLine();
p.WaitForExit();
p.Close();
```

Appendix D: Neural Network Analysis Tool

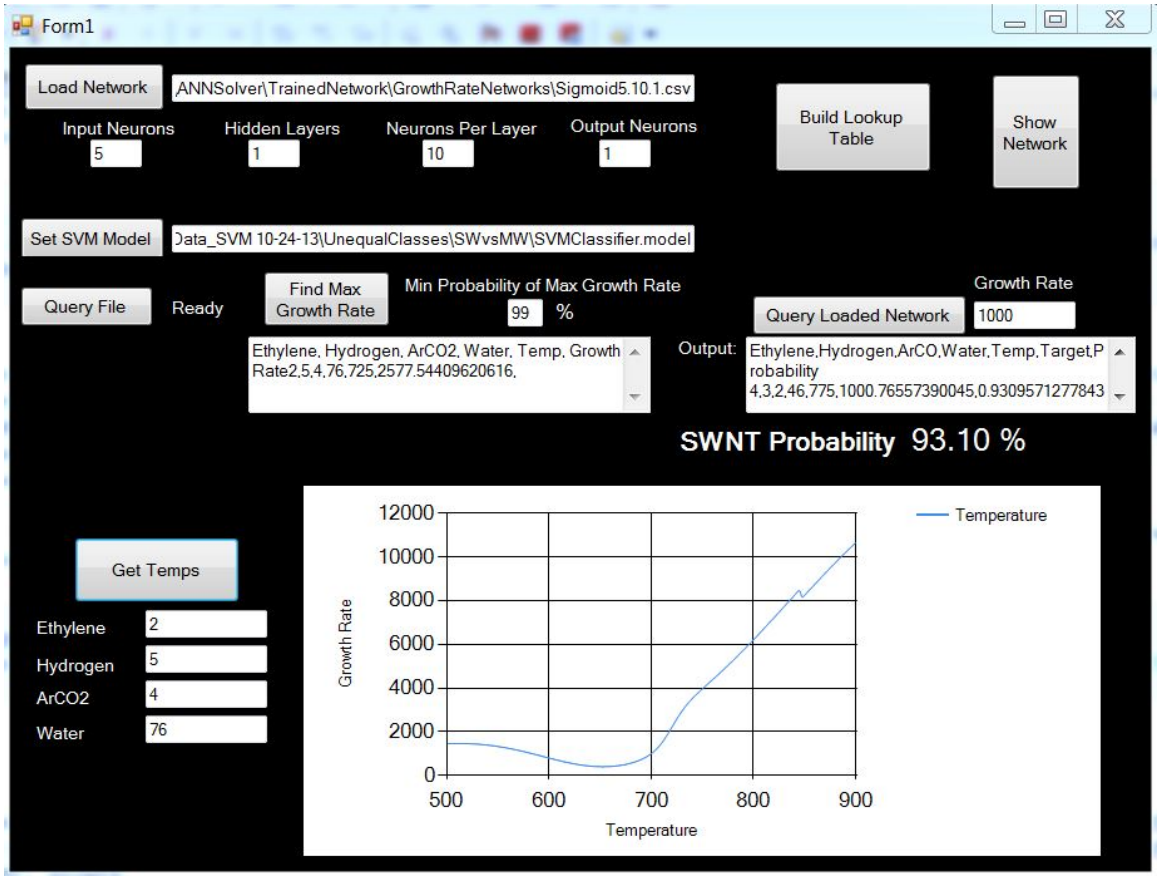

Figure D.1: The trained neural network and SVM classifier were combined to determine maximum growth rates meeting a specified SWNT growth rate probability. The analysis tool also allowed varying temperature and querying specific growth rates for experiment parameters.

Appendix E: Neural Network Weights

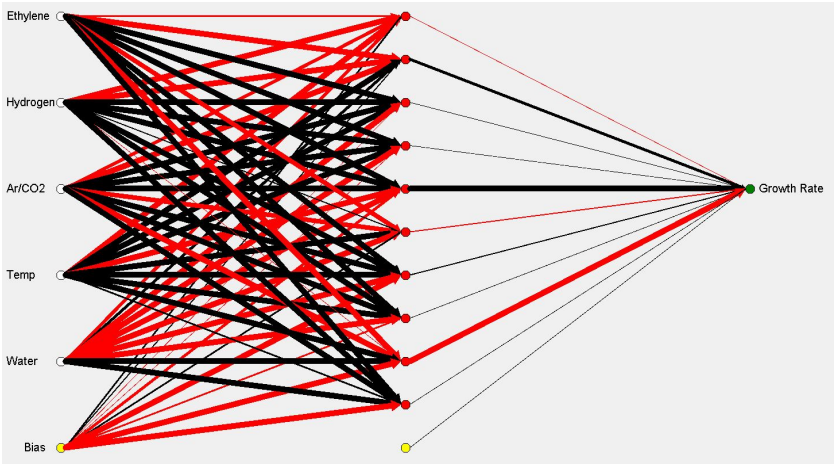

Figure E.1: The trained growth rate regression neural network weights where red lines are negative weights and black lines are positive weights. The line thickness is representative of the weight between connecting neurons.

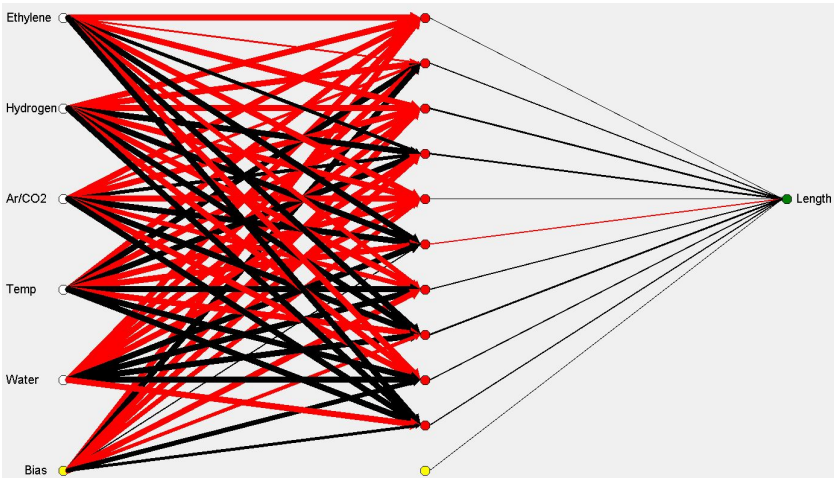

Figure E.2: The trained neural network for length regression. The hidden layer has more negative weights than the growth rate regression network and the output layer contains smaller weights.

Bibliography

[1] "Case studies-K-Fold Cross Validation", November 2013. URL http://homepages.inf.ed.ac.uk/pmartin/tutorial/case_studies.html.

[2] "Introduction to Support Vector Machines", November 2013. URL http://www.docs.opencv.org/doc/tutorials/ml/introduction_to_svm.html.

[3] "Nonlinear Kernel Mapping Functions", August 2013. URL http://www.imtech.res.in/raghava/rbpred/svm.jpg.

[4] "Nanotubes", January 2014. URL http://www.nanosciencenet.org/articles/article_CNT.htm.

[5] A.A. Puretky, S. Jesse I.N. Ivanov G. Eres, D.B. Geohegan. "In situ measurements and modeling of carbon nanotube array growth kinetics during chemical vapor deposition". *Applied Physics*, 81:223–240, 2005.

[6] Amama, P., C. Pint, S. Kim, L. McJilton, K. Eyink, E. Stach, R. Hauge, and B Maruyama. "Influence of Alumina Type on the Evolution and Activity of Alumina-Supported Fe Catalysts in Single-Walled Carbon Nanotube Carpet Growth."

[7] Amama, P., C. Pint, L. McJilton, S. Kim, E. Stach, P. Murray, R. Hauge, and B. Maruyama. "Role of water in super growth of single-walled carbon nanotube carpets". *Nano Letters*, 9:44–49, 2009.

[8] Avouris, P., J. Appenzeller, Richard Martel, and S.J. Wind. "Carbon nanotube electronics". *Proceedings of the IEEE*, 91(11):1772–1784, 2003. ISSN 0018-9219.

[9] Balkanski, M., R. F. Wallis, and E. Haro. "Anharmonic effects in light scattering due to optical phonons in silicon". *Phys. Rev. B*, 28:1928–1934, Aug 1983.

[10] C. Journet, P. Bernier A. Loiseau M.L. deLa Chapelle S. Lefrant P. Deniard R. Lee J.E. Fischer, W.K. Maser. "Large-scale production of single-walled carbon nanotubes by the electric arc technique". *Nature*, 388:756–758, 1997.

[11] Cortes, Corinna and Vladimir Vapnik. "Support-vector networks". *Machine Learning*, 20(3):273–297, 1995. ISSN 0885-6125. URL http://dx.doi.org/10.1007/BF00994018.

[12] De Volder, M., S. Tawfick, R. Baughman, and J Hart. "Carbon Nanotubes: Present and Future Commercial Applications". *Science*, 339:535–539, 2013.

[13] Encog. "Encog Artificial Intelligence Framework for Java and DotNet", August 2013. URL http://heatonresearch.com/encog.

[14] Eriksson, L., J. Jaworska, Worth. A., M. Cronin, and R. McDowell. “Methods for Reliability and Uncertainty Assessment and for Applicability Evaluations of Classification- and Regression-Based QSARS”. *Environmental Health Perspectives*, 111(10):1361–1375, 2003.

[15] Futaba, Don N., Kenji Hata, Takeo Yamada, Kohei Mizuno, Motoo Yumura, and Sumio Iijima. “Kinetics of Water-Assisted Single-Walled Carbon Nanotube Synthesis Revealed by a Time-Evolution Analysis”. *Phys. Rev. Lett.*, 95:056104, Jul 2005.

[16] Gowri Sankar, P.A. and K. Udhaya Kumar. “Investigating the effect of chirality on coaxial Carbon Nanotube Field Effect Transistor”. *Computing, Electronics and Electrical Technologies (ICCEET), 2012 International Conference on*, 663–671. March 2012.

[17] Guo, T., P. Nikolaev, A. Thess, D.T. Colbert, and R.E. Smalley. “Catalytic growth of single-walled nanotubes by laser vaporization”. *Chemical Physics Letters*, 243(1¢2):49 – 54, 1995.

[18] H. Kataura, Y. Maniwa I. Umezu S. Suzuki Y. Ohtsuka Y. Achiba, Y. Kumazawa. “Optical Properties of Single-Wall Carbon Nanotubes”. *Synthetic Metals*, 103:2555–2558, 1999.

[19] H. Zhu, J. Wei K. Wang D. Wu, K. Suenaga. “A strategy to control the chirality of single-walled carbon nanotubes”. *Journal of Crystal Growth*, 310:5473–5476, 2008.

[20] Harutyunyan, Avetik. “The Catalyst for Growing Single-Walled Carbon Nanotubes by Catalytic Chemical Vapor Deposition”. *Journal of Nanoscience and Nanotechnology*, 9:2480–2495, 2009.

[21] Haykin, Simon. *Neural Networks: A Comprehensive Foundation*. Prentice Hall, 1999.

[22] Huang, Jiaqi, Qiang Zhang, Mengqiang Zhao, and Fei Wei. “Process intensification by CO2 for high quality carbon nanotube forest growth: Double-walled carbon nanotube convexity or single-walled carbon nanotube bowls?” *Nano Research*, 2(11):872–881, 2009.

[23] Iijima, S. “Helical microtubules of graphitic carbon”. *Nature*, 354:54–58, 1991.

[24] Iijima, S. “Carbon Nanotubes and their recent developments”. *Proceedings of the IEEE*, 1998.

[25] J. Coleman, W. J. Blau, U. Khan and Y. K. Gun’ko. “Small but strong: A review of the mechanical properties of carbon nanotube polymer composites”. *Carbon*, 44:1624 – 1652, 2006.

[26] Jajarmi, P. and S. Valipour. “Prediction of the grain size of Cd-Mn-S nanocrystalline structures”. *Computational Materials Science*, 47:384 – 387, 2009.

[27] Johan A.K. Suykens, Bart L.R. De Moor, Joos P.L. Vandewalle. *Artificial Neural Networks for Modelling and Control of Non-Linear Systems*. Kluwer Academic Publishers, 1996.

[28] Kim, S., C. Pint, P. Amama, R. Hauge, B. Maruyama, and E. Stach. “Catalyst and catalyst support morphology evolution in single-walled carbon nanotube supergrowth: Growth deceleration and termination.” *Materials Research*, 25:1875–1885, 2010.

[29] Kim, S., C. Pint, P. Amama, D. Zakharov, D. Hauge, B. Maruyama, and E. Stach. “Evolution in Catalyst Morphology Leads to Carbon Nanotube Growth Termination.” *Physical Chemistry Letters*, 1:918–922, 2010.

[30] Kukovecz, A., M. Smolik, S. N. Bokova, E. Obraztsova, H. Kataura, Y. Achiba, and H. Kuzmany. “Artificial neural networks in the analysis of the fine structure of the SWCNT Raman G-band.” *AIP Conference Proceedings*, 685(1):211 – 214, 2003. ISSN 0094243X. URL http://search.ebscohost.com/login.aspx?direct=true&db=a9h&AN=11188294&site=ehost-live.

[31] Kukovecz, A., M. Smolik, S.N. Bokova, H. Kataura, Y. Achiba, and H. Kuzmany. “Diameter dependence of the fine structure of the Raman G-band of single wall carbon nanotubes revealed by a Kohonen self-organizing map”. *Chemical Physics Letters*, 381(34):434 – 440, 2003. ISSN 0009-2614. URL http://www.sciencedirect.com/science/article/pii/S0009261403017627.

[32] Kumar, M. and Y. Ando. “Chemical Vapor Deposition of Carbon Nanotubes: A Review on Growth Mechanism and Mass Production”. *Nanoscience and Nanotechnology*, 10:3739 – 3758, 2010.

[33] Lehman, J., M. Terrones, E. Mansfield, K. Hurst, and V. Meunier. “Evaluating the characteristics of multiwall carbon nanotubes”. *Carbon*, 49:2581–2602, 2011.

[34] Li, Y., W. Kim, Y. Zhang, M. Rolandi, D. Wang, and H. Dai. “Growth of Single-Walled Carbon Nanotubes from Discrete Catalytic Nanoparticles of Various Sizes”. *Journal of Physical Chemistry B*, 105(46):11424–11431, 2001.

[35] M. Grujicic, B. Gersten, G. Cao. “Optimization of the chemical vapor deposition process for carbon nanotubes fabrication”. *Applied Surface Science*, 199:90–106, 2002.

[36] M. Hall, G. Holmes B. Pfahringer P. Reutemann I. Witten, E. Frank. “The WEKA Mining Software: An Update”. *SIGKDD Explorations*, 11, 2009.

[37] Mayne, M., N. Grobert, M. Terrones, R. Kamalakaran, M. Ruhle, and H. W. Kroto. "Pyrolytic production of aligned carbon nanotubes from homogenously dispersed benzene-based aerosols". *Chemical Physics Letters*, 338:101–107, 2001.

[38] Nikolaev, Pavel., Daylond. Hooper, and Benji Maruyama. "Air Force Research Laboratory, Materials and Manufacturing Directorate, RXAS", Jan 2014.

[39] O'Connell, M. *Carbon Nanotubes: Properties and Applications*. CRC Press, 2006.

[40] Ouyang, Y., L.M. Cong, L. Chen, Q.X. Liu, and Y. Fang. "Raman study on single-walled carbon nanotubes and multi-walled carbon nanotubes with different laser excitation energies". *Physica E: Low-dimensional Systems and Nanostructures*, 40(7):2386 – 2389, 2008.

[41] Picher, Matthieu, Eric Anglaret, Raul Arenal, and Vincent Jourdain. "Self-Deactivation of Single-Walled Carbon Nanotube Growth Studied by in Situ Raman Measurements". *Nano Letters*, 9(2):542–547, 2009.

[42] Platt, John C. "Advances in kernel methods". chapter Fast training of support vector machines using sequential minimal optimization, 185–208. MIT Press, Cambridge, MA, USA, 1999. ISBN 0-262-19416-3. URL http://dl.acm.org/citation.cfm?id=299094.299105.

[43] Platt, John C. "Advances in kernel methods". chapter Probabilistic Outputs for Support Vector Machines and Comparisons to Regularized Likelihood Methods, 1–11. MIT Press, Cambridge, MA, USA, 1999.

[44] Priore, P., D. Fuenete, Raul. Pino, and J. Puente. "Dynamic scheduling of flexible manufacturing systems using neural networks and inductive learning". *Integrated Manufacturing Systems*, 1:160–168.

[45] R. Rao, T. Cherukuri B. Yakobson B. Maruyama, D. Liptak. "In situ evidence for chirality-dependent growth rates of individual carbon nanotubes". *Nature Materials*, 11:213–216, 2012.

[46] Riedmiller, M. and H. Braun. "A direct adaptive method for faster backpropagation learning: the RPROP algorithm". *IEEE International Conference on Neural Networks*, 586–591 vol 1. 1993.

[47] S. Reich, J. Robertson, L. Li. "Control the chirality of carbon nanotubes by epitaxial growth". *Chemical Physics Letters*, 421:469–472, 2006.

[48] Samuel, A.L. "Some Studies in Machine Learning Using the Game of Checkers". *IBM Journal of Research and Development*, 3(3):207–226, 1959.

[49] Sangwan, V.K., V.W. Ballarotto, D.R. Hines, M.S. Fuhrer, and E.D. Williams. "Controlled growth, patterning and placement of carbon nanotube thin films". *Solid-State Electronics*, 54(10):1204 – 1210, 2010.

[50] Shulaker, Max, Gage Hills, Nishant Patil, Hai Wei, Hong-Yu Chen, H.-S. Phillip Wong, and Subhasish Mitra. “Carbon Nanotube Computer”. *Nature*, 501:526–530, 2013.

[51] Stone, M. “Cross-Validatory Choice and Assessment of Statistical Predictions”. *Journal of the Royal Statistical Society. Series B, Statistical Methodology*, 36:111–147, 1974.

[52] Tessonnier, J. P. and D. S. Su. “Recent Progress on the Growth Mechanism of Carbon Nanotubes: A Review”. *CHEMSUSCHEM*, 4(7):824–847, July 2011.

[53] W. Chen, A. Roy, L. Dai and T. B. Tolle. “Multifunctional Chemical Vapor Sensors of Aligned Carbon Nanotubes and Polymer Composites”. *Journal of the American Chemical Society*, 128:1412 – 1413, 2006.

[54] Wen, Qian, Rufan Zhang, Weizhong Qian, Yuran Wang, Pingheng Tan, Jingqi Nie, and Fei Wei. “Growing 20 cm Long DWNTs/TWNTs at a Rapid Growth Rate of 8090 m/s”. *Chemistry of Materials*, 22(4):1294–1296, 2010.

[55] Wirth, C.T., S. Hofmann, and J. Robertson. “State of the catalyst during carbon nanotube growth”. *Diamond and Related Materials*, 18(58):940 – 945, 2009.

[56] Wood, R.F., S. Pannala, Wells J. C., A. A. Puretzky, and D.B. Geohegan. “Simple model of the interrelation between single- and multiwall carbon nanotube growth rates for the CVD process”. *Applied Physical Society: Physical Review B*, 75(235446), 2007.

REPORT DOCUMENTATION PAGE

Form Approved
OMB No. 0704–0188

1. REPORT DATE *(DD–MM–YYYY)*	2. REPORT TYPE	3. DATES COVERED *(From — To)*
27–03–2014	Master's Thesis	Sep 2012-Mar 2014

4. TITLE AND SUBTITLE

Carbon Nanotube Growth Rate Regression using Support Vector Machines and Artificial Neural Networks

5a. CONTRACT NUMBER

5b. GRANT NUMBER

5c. PROGRAM ELEMENT NUMBER

6. AUTHOR(S)

Westing, Nicholas M., First Lieutenant, USAF

5d. PROJECT NUMBER

5e. TASK NUMBER

5f. WORK UNIT NUMBER

7. PERFORMING ORGANIZATION NAME(S) AND ADDRESS(ES)

Air Force Institute of Technology
Graduate School of Engineering and Management (AFIT/EN)
2950 Hobson Way
WPAFB, OH 45433-7765

8. PERFORMING ORGANIZATION REPORT NUMBER

AFIT-ENG-14-M-83

9. SPONSORING / MONITORING AGENCY NAME(S) AND ADDRESS(ES)

Air Force Research Laboratory
Materials and Manufacturing Directorate
Senior Materials Research Engineer, Dr. Benji Maruyama
2941 Hobson Way
Wright Patterson AFB, OH, 45433
benji.maruyama@us.af.mil

10. SPONSOR/MONITOR'S ACRONYM(S)

AFRL/RXAS

11. SPONSOR/MONITOR'S REPORT NUMBER(S)

12. DISTRIBUTION / AVAILABILITY STATEMENT

DISTRIBUTION STATEMENT A: APPROVED FOR PUBLIC RELEASE; DISTRIBUTION UNLIMITED

13. SUPPLEMENTARY NOTES

14. ABSTRACT

Control of carbon nanotube growth rates is a challenging problem, thus limiting their use in a wide variety of applications. Carbon nanotubes demonstrating metallic or semiconducting properties allow for high strength materials and high current densities in smaller wires. Due to their simplicity and desirable properties, SWNTs are considered for chiral-selective growth experiments. A machine learning based approach for chiral selective growth of SWNTs using a laser-induced chemical vapor deposition growth system is introduced. Determination of SWNT growth rates is performed through in-situ Raman spectroscopy using a 532 nm excitation laser.

A total of 450 experiments are performed and a subset of 121 experiments are used to train a SWNT vs. MWNT SVM classifier. The SVM classifier determines parameter values for 99% probability or greater of SWNT growth with an accuracy of 95.04%. This subset of synthesis parameters are evaluated using an ANN to predict SWNT growth rates and growth lengths.

Analysis of the ANN growth rate model showed a peak in growth rate as a function of water concentration and growth temperature. The growth length model was trained using the same growth experiments as the growth rate model and showed a 80% reduction in validation errors. The growth length model also identified an optimal water/ethylene ratio for maximizing SWNT length.

15. SUBJECT TERMS

Support Vector Machine, Neural Network, Carbon Nanotubes

16. SECURITY CLASSIFICATION OF:			17. LIMITATION OF ABSTRACT	18. NUMBER OF PAGES	19a. NAME OF RESPONSIBLE PERSON
a. REPORT	b. ABSTRACT	c. THIS PAGE			Lt Col Jeffrey D. Clark, PhD, (ENG)
U	U	U	UU	130	19b. TELEPHONE NUMBER *(include area code)* (937) 255-3636 x4614 jeffrey.clark@afit.edu